Detectability of ocean-circulation-induced magnetic fields in geomagnetic satellite observations

Dissertation

zur Erlangung des akademischen Grades eines
Doktor der Naturwissenschaften
(doctor rerum naturalium)
vorgelegt von

Aaron Hornschild

am Fachbereich Geowissenschaften der Freien Universität Berlin,
angefertigt am Deutschen GeoForschungsZentrum GFZ, Potsdam.

Berlin, 2023

Erstgutachter:	Prof. Dr. Maik Thomas
Zweitgutachter:	Prof. Dr. Claudia Stolle

Datum der Einreichung:	11.08.2023
Datum der Disputation:	07.02.2024

„The important thing is not to stop questioning. Curiosity has its own reason for existing.“

— Albert Einstein

Abstract

The motion of salt water through the Earth's geomagnetic field generates characteristic electromagnetic (EM) signals. These ocean-induced EM signals can be observed from outside the ocean by space-borne satellite magnetometers. They depend on oceanic velocities and conductivity (i.e., temperature and salinity) and, therefore, could contribute to observing the ocean heat content or water mass transport. However, the identification of ocean-induced magnetic fields requires a separation from other geomagnetic field contributions (e.g., the core, lithosphere, and ionosphere). In contrast to tidal-induced EM signals, circulation-induced EM signals have not yet been identified in geomagnetic observations.

This thesis developed a novel Kalman-filter-based rescaling of EM signals (KREMS) to detect ocean-circulation-induced magnetic fields. The essential separation from other magnetic field contributions was achieved by predetermining the temporal behavior of the searched EM signal. KREMS was then used to locally rescale the amplitude of this predetermined EM signal by assimilating geomagnetic observations.

An observing system simulation experiment (OSSE) based on synthetic Swarm-like observations demonstrated that KREMS allowed for a global signal identification of circulation-induced EM signals regardless of their complex temporal behavior and low intensity. In an ideal scenario, the uncertainty of the rescaling could be reduced by 70% on average. The best detectability was found in the Indian Ocean basin and in parts of the Southern Ocean. In a more realistic scenario of the OSSE, KREMS performed comparably well as a least-squares approach. Moreover, it was shown that including spatial constraints in KREMS further improved signal identification.

Based on the these findings, KREMS was applied to seven years of real Swarm geomagnetic satellite observations. Compared to the OSSE, the Swarm assimilation results proved to be more ambiguous and strongly dependent on the presumed estimate of the circulation-induced EM signal. The rescaling remained highly uncertain and did not reveal a consistent spatial pattern. In some areas the signal-to-noise ratio turned out to be too low (e.g., the East Pacific Ocean), on others the rescaling indicates substantial

discrepancies between the presumed and the true circulation-induced EM signal (e.g., the Southern Indian Ocean).

Finally, a purely observation-based detection of circulation-induced EM signals was considered by estimating the temporal behavior of the EM signal from satellite altimetry. This combination also indicated the potential of KREMS to correct water mass transport estimations (e.g., from satellite altimetry) and suggested the applicability of KREMS not only for examining the detectability of EM signals but also in a broader context of ocean observations.

Kurzfassung

Die Bewegung von Salzwasser durch das geomagnetische Feld der Erde erzeugt charakteristische elektromagnetische (EM) Signale. Diese durch den Ozean induzierten EM-Signale können außerhalb des Ozeans mittels Satellitenmagnetometern aus dem Weltraum beobachtet werden. Aufgrund ihrer Abhängigkeit von den Geschwindigkeiten der Ozeanströmungen und der Leitfähigkeit des Ozeans (d. h. Temperatur und Salzgehalt) können sie zur Beobachtung des Wärmeinhalts oder des Wassermassentransports im Ozean beitragen. Die Identifizierung von ozeaninduzierten Magnetfeldern erfordert jedoch eine Trennung von anderen geomagnetischen Feldbeiträgen (z. B. des Kerns, der Lithosphäre und der Ionosphäre). Im Gegensatz zu gezeiteninduzierten EM-Signalen wurden die durch die Ozeanzirkulation induzierten EM-Signale bisher noch nicht in geomagnetischen Beobachtungen identifiziert.

In dieser Arbeit wurde eine neue Kalman-Filter-basierte Reskalierung von EM-Signalen (KREMS) entwickelt, um die durch Ozeanzirkulation induzierten Magnetfelder zu detektieren. Die entscheidende Separation von anderen Magnetfeldbeiträgen wurde erreicht, indem das zeitliche Verhalten des gesuchten EM-Signals vorher festgelegt wurde. KREMS wurde dann verwendet, um die Amplitude dieses vorbestimmten EM-Signals durch die Assimilation geomagnetischer Beobachtungen lokal neu zu skalieren.

Die Simulation eines Beobachtungssystemexperiments (OSSE) auf der Grundlage synthetischer Swarm-ähnlicher Beobachtungen zeigte, dass KREMS eine globale Signalidentifizierung von durch die Ozeanzirkulation induzierten EM-Signalen unabhängig von ihrem komplexen zeitlichen Verhalten und ihrer geringen Intensität ermöglicht. In einem idealen Szenario konnte die Unsicherheit der Reskalierung im Durchschnitt um 70% reduziert werden. Die beste Nachweisbarkeit wurde im Becken des Indischen Ozeans und in Teilen des Südlichen Ozeans festgestellt. In einem realistischeren Szenario des Beobachtungsexperiments zeigt KREMS vergleichbare Resultate wie mittels einem Ansatz der Methode der kleinsten Quadrate. Darüber hinaus wurde gezeigt, dass die Einbeziehung räumlicher Beschränkungen in KREMS die Signalidentifizierung weiter verbessert.

Auf der Grundlage dieser Erkenntnisse wurde KREMS auf sieben Jahre realer geo-

magnetischer Satellitenbeobachtungen von Swarm angewendet. Im Vergleich zu dem simulierten Beobachtungsexperiment stellten sich die Ergebnisse der Swarm-Assimilation als mehrdeutig heraus und waren stark abhängig von der angenommenen Schätzung des durch die Ozeanzirkulation induzierten EM-Signals. Die Reskalierung blieb sehr unsicher und offenbarte kein einheitliches räumliches Muster. In einigen Gebieten erwies sich das Signal-Rausch-Verhältnis als zu niedrig (z. B. im Ostpazifik), in anderen wies die Reskalierung auf erhebliche Diskrepanzen zwischen dem vermuteten und dem tatsächlichen zirkulationsbedingten EM-Signal hin (z. B. im südlichen Indischen Ozean).

Schließlich wurde ein rein beobachtungsbasierter Nachweis von durch die Ozeanzirkulations induzierten EM Signalen in Betracht gezogen, indem das zeitliche Verhalten des Signals aus der Satellitenaltimetrie geschätzt wurde. Diese Kombination zeigte auch das Potenzial von KREMS zur Korrektur von Schätzungen des Wassermassentransports (z. B. aus der Satellitenaltimetrie) und deutete auf die Anwendbarkeit von KREMS nicht nur zur Untersuchung der Nachweisbarkeit von EM-Signalen, sondern auch in einem breiteren Kontext von Ozeanbeobachtungen hin.

Contents

1 Introduction

1.1 Basic motivation

In recent years, observing and understanding our Earth system has gained more importance than ever. The complexity of the system's dynamics, the responsible mechanisms, and the interaction of a variety of different components pose major challenges for science. In addition, the ongoing changes in the climate system with far-reaching consequences demand increasingly detailed knowledge. Over the years, through tremendous effort in various research fields, substantial progress in our understanding has already been achieved. Thereby, monitoring and observing the Earth System plays a decisive role in all developments. Often novel observation techniques and the linkage of different scientific fields represent a great potential to yield more profound insights. One of the most important components of our Earth system, requiring a variety of observations for its exploration and benefiting from a combination of them, is the global ocean (Lin and Yang, 2020). The oceans and their dynamics are still challenging to observe and measure due to their horizontal and vertical size combined with their inaccessibility. In addition, the oceans not only cover 70% of the Earth's surface but also store a large amount of heat and undoubtedly play an essential role in our climate system (Schmitt, 2018). Since 90% of the Earth's thermal energy excess due to ongoing warming is stored in the ocean (Zanna et al., 2019), they are strongly affected by present changes in the Earth's climate (Johnson et al., 2022). Moreover, large-scale water transports through ocean circulation significantly influence our climate system globally. Understanding and

especially predicting ocean dynamics requires as numerous and diverse observations as possible. Given the challenging spatial and temporal scales of ocean dynamics, ocean modeling has played a crucial role in this process. Thereby, correcting numerical model conditions by satellite or in-situ observations and combining ocean models and observations through data assimilation has become very common (Anderson et al., 1996; Moore et al., 2019). When observing the oceans, satellite measurements play a special role as they provide an all-season full view with global coverage. Nowadays, various quantities like sea surface temperature and salinity, sea surface hegiht, surface winds, and wave heights are remotely sensed from space. A major advance in ocean observation was made through high-precision altimetry (e.g., TOPEX/Poseidon mission (Fu et al., 1994) and its successors, the Jason series (Masters et al., 2012)). However, most of these observation techniques only allow direct measurements of the ocean surface and thereby showing that each observing system has its advantages and limitations. In the future, complementing and combining observation techniques from different research fields represents a promising perspective to better understand our Earth system. An outstanding example of connecting research fields and establishing novel observation techniques is presented by satellite gravity measurements. The satellite gravity missions GRACE (Tapley et al., 2004) and GRACE-FO (Landerer et al., 2020) not only complement existing observations but also contribute to understanding climate change (Tapley et al., 2019), especially when combined with other sources of measurement, such as altimetry and in-situ measurements (Barnoud et al., 2023). Thereby, the advantage of satellite gravimetry, compared to other space-borne observations, is providing not only ocean-surface information but on the entire ocean mass redistribution (Chen, 2019). Another example of a connection between different research fields providing such a similarly intriguing source of information is offered by geomagnetic observations and their link to ocean dynamics. Analogous to monitoring changes in the gravitational field, slight changes in the geomagnetic field could indirectly reveal ocean information about the whole water column. Indeed, secondary electromagnetic (EM) fields are generated by the motion of conductive salt water through the Earth's geomagnetic field. These oceanic EM signals depend on water transport and, additionally, on the oceanic conductivity, i.e., temperature and salinity, and are, in principle, remotely observable. Consequently, satellite measurements of ocean-induced EM signals provide both an all-season view with global coverage and an exciting complementary source of information on the whole water column. Motivated by the potential to serve as an indirect source of information and novel observing system, the possible detection and identification of ocean-circulation-induced EM signals in geomagnetic satellite observations is the topic of this thesis.

1.2 Historical development and current state of research

The theoretical foundations of electromagnetic induction were laid by Michael Faraday in 1831 (Ronald Anderson, 1993). Faraday himself already pointed out the generation of electric currents due to the movement of large water masses through the Earth's ambient magnetic field. Twenty years later, Charlton Wollaston was able to observe the first voltage fluctuations in submarine cables (Nature, 1948). The connection between electromagnetism and oceanic water movements was consolidated in the early and mid-20th century by Young et al. (1920); Cherry and Stovold (1946) and Longuet-Higgins et al. (1954). Later on, electromagnetic induction processes in the ocean were the subject of comprehensive theoretical research studies by Larsen (1968) and Sanford (1971) and further developments by Chave and Luther (1990), who introduced the poloidal and toroidal decomposition of the ocean-induced magnetic field (OIMF). First estimations of the EM signals based on an ocean general circulation model (OGCM) were performed by Stephenson and Bryan (1992); Flosadóttir et al. (1997) and Tyler et al. (1997). Since the poloidal part of the OIMF can reach outside the ocean, ocean-generated magnetic fields provide a remote observation possibility. This potential to remotely sense the oceans from distant land or satellite observation was discussed by Tyler et al. (1999). Consequently, new perspectives have emerged with the launch of the satellite mission CHAMP (Reigber et al., 2002) and especially the high-precision magnetometer observation by the ongoing Swarm satellite mission (Friis-Christensen et al., 2006). Typically one distinguishes between two types of OIMF: the one associated with tidal motion and the one caused by ocean circulation. Thus, several further theoretical research activities were already dedicated to both tidal EM signals (e.g. Kuvshinov and Olsen, 2005; Dostal et al., 2012; Velímský et al., 2018) as well as OIMF from circulation (e.g. Vivier et al., 2004; Manoj et al., 2006). Nevertheless, due to the weak signal strength and the superposition with other magnetic field components, the detection of OIMF poses a major challenge Kuvshinov (2008). However, the regularity of the periodic tidal EM signals allowed their identification in various observations. Maus and Kuvshinov (2004) identified tidal-induced EM signals in observatory measurements, Schnepf et al. (2014) and Velímský et al. (2021) analyzed measurements from ocean-bottom electro-magnetometer and seafloor voltage cables, and in particular, Tyler et al. (2003) and Sabaka et al. (2016, 2018, 2020) achieved the detection of tidal-induced EM signals in CHAMP and Swarm satellite observations. In contrast, the OIMF from ocean circulation could not be identified in satellite observations so far. In the case of ocean circulation, the irregular ocean flow complicates the separation from other magnetic field constituents. Moreover, there are also no promising approaches for a possible

identification so far. However, the success of tidal OIMF detection and several research studies clearly demonstrate oceanic EM signals as an exciting source of indirect observation. Hence, many additional research activities addressed the applications and benefits of observing OIMF, covering a broad spectrum of topics. Of particular importance is the dependence of these signals on electric conductivity and transport in the ocean and the Earth's electromagnetic structure. Schnepf et al. (2015); Grayver et al. (2016) used tidal magnetic signals to explore the characteristics of the Earth's structure. Saynisch et al. (2016) used the sensitivity on electric conductivity, and therefore on temperature and salinity, to investigate the climate impact, and Petereit et al. (2019) expanded on this conductivity sensitivity and studied climate trends in shelf regions. Additionally, climate phenomenons like the El Niño Southern Oscillation were analyzed using the EM signals (Petereit et al., 2018). The connection of EM signals to oceanic conductivity was even successfully used to estimate the ocean heat content from satellite observations (Irrgang et al., 2019; Trossman and Tyler, 2019). Finally, EM signals have been associated with extreme events like tsunamis (Toh et al., 2011; Schnepf et al., 2016; Minami et al., 2021). Concerning the ocean circulation-induced EM signals, Irrgang et al. (2017) has already performed a synthetic assimilation experiment to demonstrate that OIMF could provide valuable constraints for an OGCM. All things considered, the overwhelming amount and variety of research studies and results reveal considerable benefits from OIMF observations and indicate that observing oceanic EM signals can also contribute to a deeper understanding of ocean dynamics in the future.

1.3 Research objectives and structure of the thesis

According to the current state of research, the question of the detectability of ocean-circulation-induced magnetic signals arises naturally. The remarkable success based on the already identified tidal EM signals suggest the exploration of the detectability of circulation-induced EM signals. On the one hand, scientific studies agree that the detectability of circulation-induced EM signals would open up new possibilities for observing ocean dynamics, e.g., oceanic transports. On the other hand, these studies also agree that their separation from other magnetic contributions is an enormous challenge. However, since the European Space Agency (ESA) launched the high-precision magnetometer Swarm satellite mission, the weak EM signals from circulation and their spatio-temporal variations are, for the first time, in the range of measurement precision, and, therefore, in principle detectable. Indeed, one of the Swarm mission's secondary research objectives is identifying ocean circulation by its magnetic signature (Friis-Christensen et al., 2006). The present thesis is dedicated to this research objective. Due to missing approaches on how to achieve this, a new method has been developed in context of this thesis:
A **K**alman-filter-based **R**escaling of **E**lectro**M**agnetic **S**ignals (**KREMS**).
This method rescales an initially given EM signal, representing a presumed estimate, by a constant factor through the assimilation of geomagnetic satellite observations. In this thesis, KREMS is used to rescale presumed estimates of the ocean-circulation-induced magnetic field. Subsequently, the rescaling of presumed estimates of the OIMF will be used to evaluate their signal identification in observational data. The goal is to use the resulting scale factor from KREMS to analyze the detectability of ocean-circulation-induced EM signals.

This thesis aims to validate and evaluate the novel KREMS method for the identification of ocean-circulation-induced magnetic fields in geomagnetic satellite observations and presents the application to real Swarm magnetometer measurements. Therefore, the thesis is structured as follows: First of all, the theoretical background and the methodology used are briefly described in Chapter 2. Subsequently, since the proposed KREMS is based on presumed estimates of the OIMF, critical dependencies and relevant approximations are initially outlined in Chapter 3. Finally, the KREMS as a detection method is considered in terms of two general objectives:

1. Validation and evaluation of KREMS

The proof of concept and the validation of the KREMS as a detection method is addressed in Chapter 4. This chapter valuates the detectability of OIMF using KREMS in the context of an observing system simulation experiment (OSSE). Besides the validation, the OSSE is also used to extensively study the KREMS method and answer the following research questions:

- What are the advantages and capabilities of KREMS?
- What are the most relevant influences on the results of KREMS?
- What are the limitations of KREMS?

2. Application of KREMS to Swarm satellite observations

The real-world application of KREMS as a detection method is presented in Chapter 5. In this chapter, KREMS is used to identify both model-based and observation-based presumed OIMF estimates in Swarm satellite observations and to answer the following questions:

- Can KREMS be used to identify ocean-circulation-induced EM signals in Swarm satellite observations?
- Is a purely observation-based detection of ocean-circulation-induced magnetic fields possible?

At the end, a summary is given, and the results and major findings are concluded in Chapter 6.

2

Theoretical background and methodology

2.1 The ocean induced-magnetic field

2.1.1 Electromagnetic induction

The presence of dissolved ions as charge carriers makes seawater a conductive fluid. The motion of conductive seawater through the Earth's main magnetic field generates both electric and magnetic fields. The deflection of differently charged ions by the ambient magnetic field induces electric currents, which in turn cause secondary so-called ocean-induced magnetic fields (OIMF). The phenomenon of motionally induced magnetic fields in the ocean can be fully described by the theory of classical electromagnetism. The force acting on dissolved ions moving in the oceans is given by the fundamental Lorentz force $\mathbf{F}^{\text{lorentz}}$ (Heaviside, 1889; Lorentz, 1895):

$$\mathbf{F}^{\text{lorentz}} = \text{q}\,(\mathbf{E} + \mathbf{v} \times \mathbf{B}^{\text{earth}}), \tag{2.1}$$

where $\mathbf{E}$ describes the electric Field, $\mathbf{v}$ the oceanic velocity, $\mathbf{B}^{\text{earth}}$ the Earth's main magnetic field and q a unit charge. According to Ohm's law, the electric current density $\mathbf{J}$ is then proportional to this force per unit charge:

$$\mathbf{J} = \sigma\,(\mathbf{E} + \mathbf{v} \times \mathbf{B}^{\text{earth}}) \tag{2.2}$$

where the conductivity σ represents the proportionality factor.

The theoretical foundations of electromagnetic induction processes are described by Maxwell's equations (Maxwell, 1865):

$$\nabla \cdot \mathbf{E} = \frac{\varrho}{\epsilon_0} \qquad (2.3a) \qquad \nabla \cdot \mathbf{B} = 0 \qquad (2.3b)$$

$$\nabla \times \mathbf{E} = -\frac{\partial \mathbf{B}}{\partial t} \qquad (2.3c) \qquad \nabla \times \mathbf{B} = \mu_0 \left(\mathbf{J} + \epsilon_0 \frac{\partial \mathbf{E}}{\partial t} \right) \qquad (2.3d)$$

This set of partial differential equations describes the generation and transformation of electric and magnetic fields ($\mathbf{E}$ and $\mathbf{B}$) by charges and currents (ρ and $\mathbf{J}$). The constants μ_0 and ϵ_0 in these equations stand for the vacuum magnetic permeability and the vacuum permittivity. In the case of the OIMF, where electric currents do not change rapidly, one can consider a quasi-static approximation, so that the displacement current $\epsilon_0 \frac{\partial \mathbf{E}}{\partial t}$ in (2.3d) can be neglected. Hence, (2.3d) can be replaced by Ampère's law:

$$\nabla \times \mathbf{B} = \mu_0 \mathbf{J} \qquad (2.4)$$

This directly implies that $\nabla \cdot \mathbf{J} = 0$ (divergence of the curl of a vector field is always zero), which is the condition of magnetostatic dealing with steady currents (i.e., continuous current without change and charge pile up). In fact, this approximation is valid until currents do not change extremely rapidly, and is well justified in the case of oceanic values (Sanford, 1971). On this basis, the induction equation can be derived. By using (2.2) to express the electric field $\mathbf{E}$ and substituting it in Faraday's law (2.3c), one gets:

$$\nabla \times \left(\frac{1}{\sigma} \mathbf{J} - \mathbf{v} \times \mathbf{B}^{\text{earth}} \right) = -\frac{\partial \mathbf{B}}{\partial t} \qquad (2.5)$$

Subsequently, using Ampère's law (2.4) to replace $\mathbf{J}$ yields the electromagnetic induction equation:

$$\nabla \times \left(\frac{1}{\sigma} \nabla \times \mathbf{B} \right) + \mu_0 \frac{\partial \mathbf{B}}{\partial t} = \mu_0 \nabla \times \left(\mathbf{v} \times \mathbf{B}^{\text{earth}} \right). \qquad (2.6)$$

The induction equation can be solved according to the OIMF $\mathbf{B}$ for a given oceanic velocity field $\mathbf{v}$, corresponding conductivity σ, and the main magnetic field $\mathbf{B}^{\text{earth}}$. Various approaches have been carried out to perform this task and to solve the induction equation numerically. Firstly, a so-called thin sheet approximation developed by Tyler et al. (1997) and Vivier et al. (2004) was used to solve a simplified version of the induction equation by neglecting the self-induction term ($\mu_0 \frac{\partial \mathbf{B}}{\partial t}$). Furthermore, approaches to solving the complete induction equation in the time domain, like ElmgTD (Velímský and Martinec, 2005; Velímský, 2013), were implemented. Additionally, electromagnetic induction solvers, like

X3DG (Kuvshinov, 2008), which operate in the frequency domain, were developed. In spectral space, the electric and magnetic field ($\mathbf{E}$, $\mathbf{B}$), as well as the electric charge and current density (ρ, $\mathbf{J}$), are depending on frequency rather than time. The transformation between frequency and time domains can be achieved using Fourier transformation with a time dependency of $\exp(i\omega t)$, where ω is the angular frequency, and i the imaginary unit and t the time. As a result, since Faraday's law (2.3c) is transformed to $\nabla \times \mathbf{E} = -i\omega\mathbf{B}$, the induction equation in the frequency domain is given by:

$$\nabla \times \left(\frac{1}{\sigma}\nabla \times \mathbf{B}\right) + i\mu_0\omega\mathbf{B} = \mu_0 \nabla \times \left(\mathbf{v} \times \mathbf{B}^{\text{earth}}\right). \tag{2.7}$$

Generally, since the magnetic field is divergence-free, it can be decomposed into a poloidal and a toroidal part:

$$\mathbf{B} = \mathbf{B}^{\text{poloidal}} + \mathbf{B}^{\text{toroidal}}, \tag{2.8}$$

and each part can be represented by a scalar potential (Backus, 1986):

$$\mathbf{B}^{\text{poloidal}} = \nabla \times (\nabla \times (\mathbf{r}\Phi)) \qquad \mathbf{B}^{\text{toroidal}} = \nabla \times (\mathbf{r}\Psi), \tag{2.9}$$

where $\mathbf{r}$ denotes the radial vector in spherical coordinates and Φ and Ψ the scalar potentials. Thereby, the toroidal field is tangential to spheres in contrast to the poloidal part,

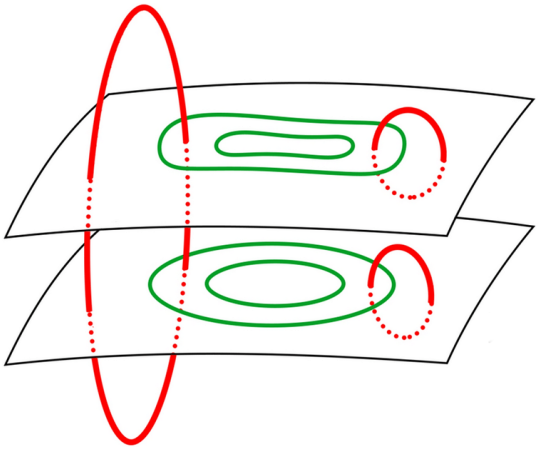

Figure 2.1: Schematic illustration of the poloidal (red) and toroidal (green) part of the magnetic field in relation to a plane. Figure was taken from Yi and Choe (2022).

where the curl of the poloidal field is tangential to spheres (Figure 2.1). Therefore, the poloidal part of the OIMF is of primary interest to the detection of EM signals because it contains a radial component and can reach outside the ocean. On the contrary, the toroidal field is confined to the ocean, meaning that it is not observable from outside the ocean. However, if conductivity is assumed to be not only radially, but also laterally

dependent, the toroidal and poloidal parts are coupled (Velímský et al., 2019). This fact emphasizes that these lateral conductivity variations must be considered when modeling the OIMF.

2.1.2 X3DG induction solver

The forward modeling of the poloidal part of the OIMF in this thesis is mainly based on the electromagnetic induction solver X3DG. X3DG is a thoroughly tested and widely used electromagnetic induction solver (Kelbert et al., 2014; Šachl et al., 2019). This solver calculates numerical solutions of Maxwell's equations in the frequency domain. Instead of taking the ocean velocity directly into account, the X3DG allows for the excitation of any external electric current. Accordingly, Equation (2.4) reads as follows:

$$\nabla \times \frac{1}{\mu}\mathbf{B} = \sigma\mathbf{B} + \mathbf{J}^{\text{ext}} \tag{2.10}$$

In the case of the OIMF, the external excitatory electric current $\mathbf{J}^{\text{ext}}$ is then given by:

$$\mathbf{J}^{\text{ext}} = \sigma(\mathbf{v} \times \mathbf{B}^{\text{earth}}). \tag{2.11}$$

The calculation of the frequency-domain magnetic field is performed using an iterative volume integral approach. The volume integrals are solved using a Greens function technique in a background 1D conductivity. Conductivity anomalies are considered through introduced scattered electric and magnetic fields. More details can be found in Kuvshinov and Semenov (2012).

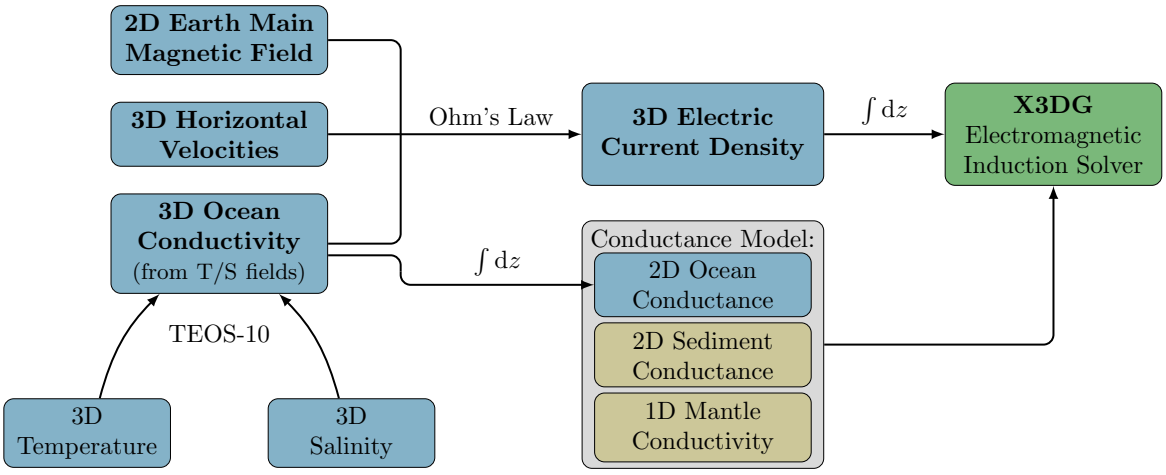

Figure 2.2: Sketch of the processing steps for the input of the electromagnetic induction solver X3DG. (Note: blue boxes highlight time-dependent quantities, brown boxes mark quantities assumed to be constant in time)

Both the electric source and an appropriate description of a surrounding conductance model are needed as input for the X3DG solver. Figure 2.2 illustrates the usual processing steps to obtain both required inputs for the X3DG solver. The external excitatory electric source induced by the ocean flow is prescribed in an infinitesimal thin sheet as a depth-integrated density:

$$\mathbf{j}^{\text{ext}} = \int_{-d}^{0} \sigma \, (\mathbf{v} \times \mathbf{B}^{\text{earth}}) dz, \tag{2.12}$$

where d denotes the depth of the ocean. The vertical ocean velocities are typically assumed to be negligible (resulting in an ocean velocity vector of $\mathbf{v} = (\mathbf{v}_x, \mathbf{v}_y, 0)$) since they are at least one order of magnitude smaller than horizontal ocean velocities. However, Velímský et al. (2019) recently took vertical velocities into account when analyzing the toroidal magnetic field. The conductivity weight in Equation (2.11) and (2.12) is derived from a realistic 3D ocean conductivity description, as Irrgang et al. (2016) showed that its spatial distribution and temporal variation influence the OIMF. Such an ocean conductivity description can be taken directly from datasets like the World Ocean Atlas 2018 (WOA18) by Tyler et al. (2017) or can be additionally calculated from 3D temperature and salinity fields. This can be accomplished using the Gibbs Seawater Oceanographic Toolbox from the Thermodynamic Equation of Seawater 2010 (McDougall and Barker, 2011, TEOS-10). The Earth's main magnetic field is assumed to be constant over depth and the data can be taken from the International geomagnetic reference field IGRF-13 model (Alken et al., 2021).

Finally, the conductance model considered in X3DG consists of two parts. The first part is an anomalous ocean conductance layer that accounts for oceanic and sediment conductivity. The ocean conductance stems from the 3D ocean conductivity used before by simple integration over depth. A time-constant conductance of the sediments is obtained with the heuristic approach from Everett et al. (2003) using the sediment thickness of Laske and Masters (1997). In this approach, the different thicknesses of sediments and igneous rock are weighted with fixed conductivity values. The second part of the conductance model consists of a background 1D conductivity profile characterizing the Earth's mantle conductivity, e.g., as determined by Grayver et al. (2017) or Püthe et al. (2015). It is accompanied by a highly conductive core. Finally, the atmosphere over the ocean layer is assumed to be an insulator. The conductance model used in X3DG is summarized in Figure 2.3.

Output of the X3DG induction solver

X3DG allows the calculation of the OIMF at any point in time and space. Therefore, the OIMF can be evaluated at surface or approximately 460 km satellite height (typical

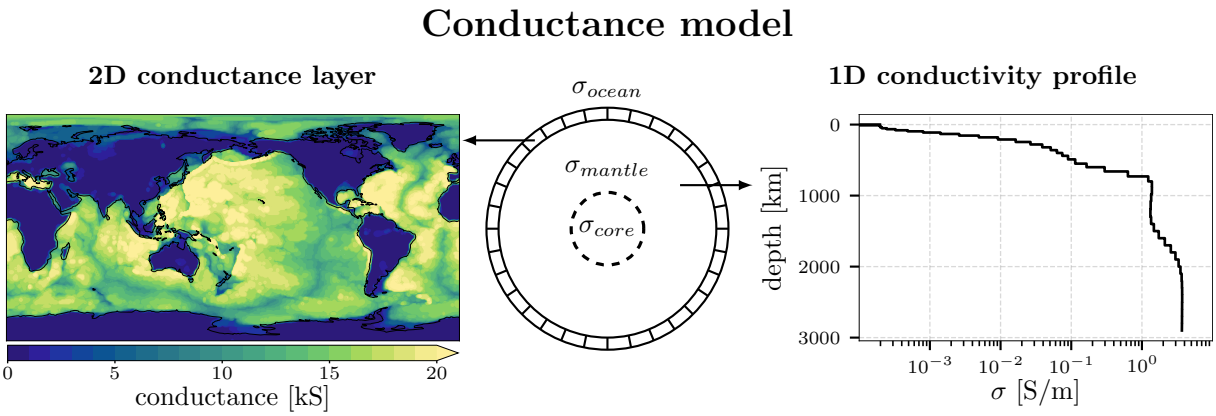

Figure 2.3: The two parts of the conductance model used in the X3DG induction solver. The left side shows the 2D anomalous conductance layer accounting for the ocean and sediment conductance. The right side illustrates the 1D conductivity profile, which is assumed to be located beneath the anomalous conductance layer accounting for the mantle conductivity.

height for the Swarm satellite mission) with a spatial resolution of 1°. The results of a temporal averaged OIMF derived from ocean model velocities are exemplarily presented in Figure 2.4. The underlying X3DG input, the zonal and meridional external electric current density (top panel), are shown, as well as the corresponding X3DG output at surface and satellite height (bottom panel).

Quasi-stationary regime

Since the temporal pattern of oceanic tides corresponds to well-known frequencies, calculating the OIMF in the frequency domain is of particular value when considering tidal-induced EM signals. Contrarily, the temporal behavior of the general ocean circulation does not exhibit specific frequencies. Consequently, when analyzing the magnetic field included by ocean circulation, the time series is of higher interest rather than a specific frequency. Therefore, solving the electromagnetic induction for each time step in a quasi-stationary regime is helpful. In the case of the X3DG solver, this is managed by choosing a sufficiently small excitation frequency of the external electric current (because a zero frequency is not allowed). The imaginary part of the complex frequency-domain magnetic field accounts for its temporal evolution. In order to simulate the quasi-stationary case with X3DG, it is reasonable to choose the excitation frequency as small as possible so that the imaginary part tends to zero. This criterion was used in test calculations to set an excitation frequency of $10^{-12}\,\mathrm{days}^{-1}$ for the quasi-stationary regime. However, the quasi-stationary use of X3DG also introduces some errors since quantities like the penetration depth of EM signals are assumed frequency-independent. A more detailed analysis of this

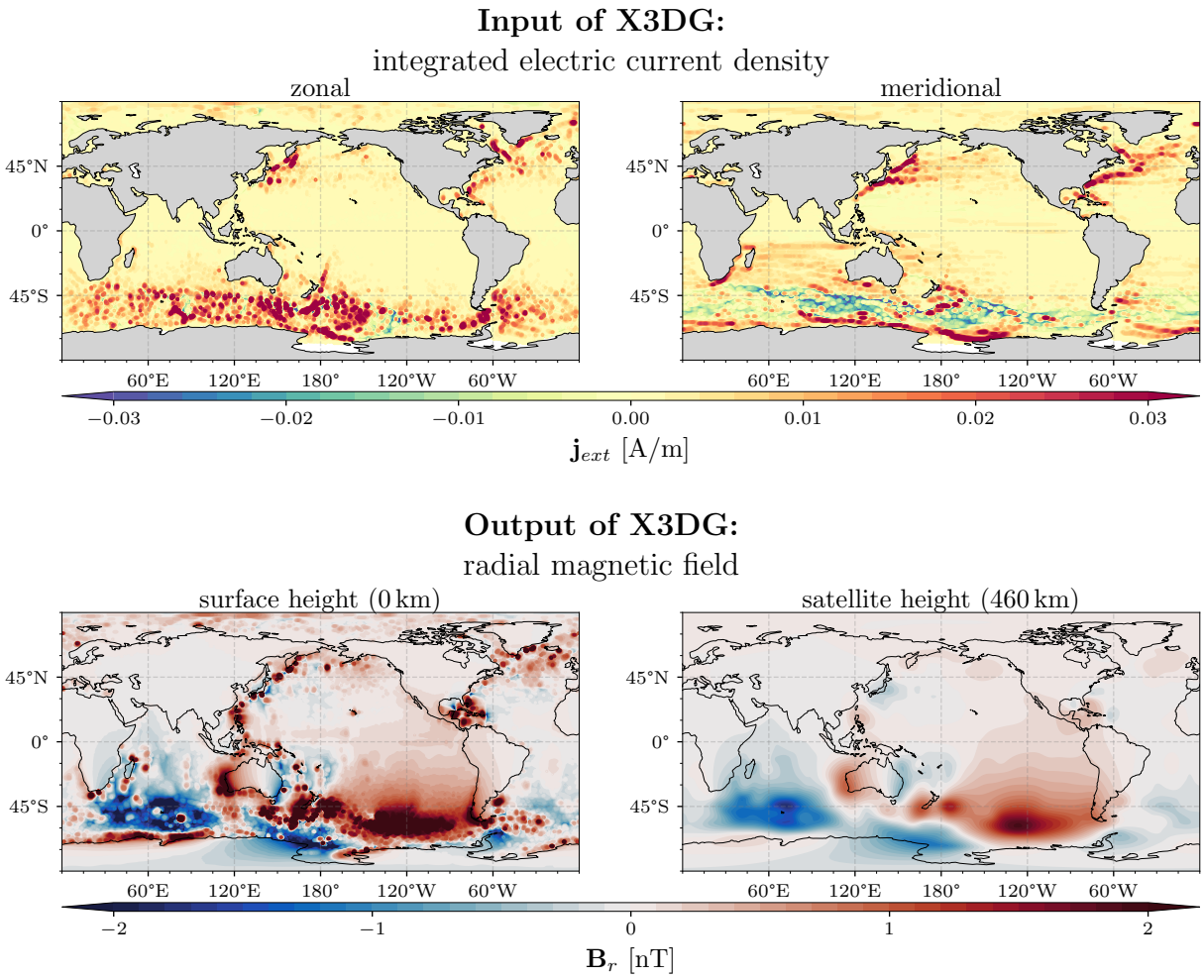

Figure 2.4: Input and Output of the X3DG electromagnetic induction solver. The top row shows the zonal and meridional electric current density used as an external excitation input in X3DG. The input is representatively derived from temporal averaged ocean model velocities. The bottom row shows the resulting radial component of the magnetic field induced by ocean circulation. The left side shows the magnetic field on Earth's surface height; the right side on approximately Swarm satellite height at 460 km over the Earth's surface.

quasi-stationary approach and its errors is given in Section 3.2.3.

From the description of the X3DG induction solver, it is evident that the OIMF depends on various quantities (oceanic conductivity and velocities, Earth's main magnetic field, and mantle and sediment conductivity) and is influenced by several assumptions (e.g., quasi-stationary approximation). The potentially resulting uncertainties on the OIMF must be taken into account in the subsequent analysis and interpretation of the results. Therefore, the impact of these essential quantities and considered approximations on the oceanic EM signals is investigated in more detail in Section 3.2.

2.1.3 Biot-Savart solver

As a conclusion for oceanic EM signal calculations, an additional, more simplified approach to estimate the OIMF will be introduced shortly. In a magnetostatic context, the OIMF can be directly calculated from an electric current distribution using the law of Biot-Savart. The Biot-Savart equation is the fundamental law of magnetostatic and describes the magnetic field generated by a constant electric current. It is given by:

$$\mathbf{B}(\mathbf{r}) = \frac{\mu_0}{4\pi} \int_V \mathbf{J}(\mathbf{r}\,') \times \frac{\mathbf{r} - \mathbf{r}\,'}{|\mathbf{r} - \mathbf{r}\,'|^3}\, dV' \tag{2.13}$$

The magnetic field can be calculated at an arbitrary position in space $\mathbf{r}$ by integrating over the complete electric current density distribution $\mathbf{J}$ in the Volume V'. The Biot-Savart law, combined with the superposition principle, is equivalent to Maxwell's equation in the case of magnetostatic. A derivation of Equation (2.13) from Maxwells's equation can be found in the Appendix A.1. With this simplified Biot-Savart approach, it is impossible to consider the surrounding conductivity model or the coupling of poloidal and toroidal parts through lateral conductance variations. However, the direct link between electric current density and the magnetic field within Biot-Savart is beneficial for understanding and examination purposes. Due to this direct link and the superposition principle, the Biot-Savart magnetic field calculations can be linearized, allowing an inversion in future developments. In some exceptionally simplified cases, the Biot-Savart approach even allows an analytical solution. On the downside, solving the volume integral of the Biot-Savart law can also quickly get cumbersome. Moreover, due to the neglection of the surrounding conductivity and its lateral variations, the solutions resulting from the Biot-Savart law must be considered inaccurate. In the context of this thesis, a simple Biot-Savart solver was implemented and used for investigations on an inaccurate electromagnetic framework and as a simple approximation. Furthermore, the goal was to examine whether presumed OIMF estimates calculated by this simplified Biot-Savart approach are still sufficient to analyze the detectability using the KREMS method. Therefore, a comparison of the resulting OIMF based on the law of Biot-Savart with the advanced X3DG induction solver will be first drawn in Section 3.2.4.

2.2 Geomagnetic field modeling by assimilating satellite observations

2.2.1 Geomagnetic field

The Earth's geomagnetic field comprises several contributions from different origins. Accordingly, various interests arise in determining individual contributions, ranging from understanding the generation processes (e.g., dynamo action in the core, magnetization in the crust, electric currents in the ionosphere and magnetosphere) to studying further dependencies and implications (e.g., probing the conductivity of the mantle and examining ionospheric and magnetospheric phenomena). However, direct measurement of the geomagnetic field only provides the superposition of all magnetic field constituents. In addition, separating the geomagnetic field obtained from direct measurements into its constituents is a complex and challenging task due to the wide range of spatial and temporal scales and the fact that the latter are overlappping. The most dominant magnetic field contribution, the core field, arises from dynamo actions in the Earth's outer core. This field reaches intensities up to 65 000 nT at the Earth's surface and varies on time scales ranging from months to millennia. On smaller spatial scales, a lithospheric part resulting from the magnetization of rocks in the crust has to be taken into account. Its temporal variations are only on geological timescales. Furthermore, electric currents in the ionosphere or magnetosphere caused by thermospheric winds or solar radiation significantly contribute to the geomagnetic field. These parts, in turn, can lead to intense variations on very short up to decadal timescales. Additionally, the fluctuation of the geomagnetic field can induce electric currents in the crust or mantle, resulting in secondary magnetic fields. Finally, as described in Section 2.1, induction processes in the ocean generate further secondary magnetic fields.

2.2.2 Kalman filter-based assimilation

The OIMF is only a tiny contribution to the geomagnetic field. Identifying and potentially utilizing this field in geomagnetic satellite data requires a precise separation from the different constituents. This separation is a demanding task due to the broad spectrum of spatial and temporal scales of the geomagnetic constituents. In geomagnetic field modeling, several approaches were pursued to meet this challenge (Hulot et al., 2015). Of these, numerous models are based on the regularized least squares method, like the geomagnetic field model CHAOS (Finlay et al., 2020) or the comprehensive models by Sabaka et al. (2020). Eventually, some of them followed a Bayesian approach, like the geomagnetic field model Kalmag (Baerenzung et al., 2020). The Bayesian approach is

based on updating a prior probability of a model under the influence of observational data using Bayes' theorem. For a model M and its prior probability $P(M)$ and observed data D, the posterior probability $P(M \mid D)$, which describes the probability of the considered model M after the observation of D, can be determined through Bayes' theorem (Bayes, 1763):

$$P(M \mid D) = \frac{P(D \mid M) \cdot P(M)}{P(D)}. \tag{2.14}$$

Thereby, $P(D \mid M)$ is the so-called likelihood and describes the probability distribution of the data D given the model M. The advantage of the Bayesian approach is the consideration of uncertainties in a natural way. In the case of magnetic field modeling, it not only allows to determine mean-field solution but also its associated uncertainty. Gillet et al. (2013) initiated this Bayesian approach for geomagnetic field models. This approach was further developed and combined with a Kalman filter in the Kalmag model.

Kalman filter

A Kalman filter (Kalman, 1960) is an algorithm that sequentially assimilates observations, whenever available, to update a model. Thereby, inaccuracies and noise in the measurements are taken into account, and a complete probability distribution of the parameters describing the system is estimated. By capturing correlations in the system, the Kalman filter allows a reasonable state estimation while optimally reducing errors. The Kalman filter is notably less computationally demanding than a full Bayesian inversion as it is a recursive algorithm. The algorithm works in two alternating steps: First, a forecast step, where the evolution of the system state is predicted until some observations become available. During this step, the system's dynamic is modeled, and a forecast state $\mathbf{X}_t^{\mathrm{f}} \sim \mathcal{N}(\mathbf{x}_t^{\mathrm{f}}, \mathbf{P}_t^{\mathrm{f}})$ is calculated, predicting both the mean ($\mathbf{x}_t^f$) and covariance ($\mathbf{P}_t^f$) of the model assuming a gaussian distribution. Secondly, an analysis step follows, where a Bayesian inversion updates the system accordingly to the new data. Thereby, whenever a new observation $\mathbf{y}_t$ is available at time t, an analyzed state $(\mathbf{x}_t^{\mathrm{a}}, \mathbf{P}_t^{\mathrm{a}})$ can be computed by:

$$\mathbf{x}_t^{\mathrm{a}} = \mathbf{x}_t^{\mathrm{f}} + \mathbf{K}_t \left(\mathbf{y}_t - \mathbf{H}\mathbf{x}_t^{\mathrm{f}} \right) \qquad \mathbf{P}_t^{\mathrm{a}} = (\mathbf{I} - \mathbf{K}_t\mathbf{H})\, \mathbf{P}_t^{\mathrm{f}}. \tag{2.15}$$

Here, $\mathbf{H}$ denotes the observation operator, which projects the model state $\mathbf{x}_t^{\mathrm{f}}$ to the observation $\mathbf{y}_t$, and $\mathbf{K}_t$ is the Kalman gain at time t. This Kalman gain accounts for error covariances and depends on both the uncertainty of the system ($\mathbf{P}_t$) and observations ($\mathbf{R}_t$). This combined uncertainty information is used to weight the observation residuals ($\mathbf{y}_t - \mathbf{H}\mathbf{x}_t^{\mathrm{f}}$) when updating the system (Equation (2.15)). The Kalman gain is given by:

$$\mathbf{K}_t = \mathbf{P}_t^{\mathrm{f}}\mathbf{H}^T \left(\mathbf{H}\mathbf{P}_t^{\mathrm{f}}\mathbf{H}^T + \mathbf{R}_t \right)^{-1}. \tag{2.16}$$

The steps of the Kalman filter algorithm can then be repeated recursively.

2.2.3 The geomagnetic field model Kalmag

The method introduced later in this thesis is used to detect oceanic EM signals and is based on the Kalman filter algorithm of the geomagnetic field model Kalmag (Baerenzung et al., 2020, 2022). This model is derived from assimilating geomagnetic satellite observations from the low-orbit satellite missions CHAMP and SWARM. The model consists of seven different magnetic sources (listed in Table 2.1) contributing to the observations. Three internal ones accounting for the core field, a lithospheric field, and an induced/residual ionospheric field. And additionally, four external sources are considered, namely a remote, a close, and a fluctuating magnetospheric field, and, finally, a field associated with field-aligned currents. Since the magnetic field is considered in the current free region (which means $\nabla \times \mathbf{B} = 0$), each of them can be expressed by a potential V:

$$\mathbf{B} = -\nabla \mathrm{V}. \tag{2.17}$$

An exception must be made for the source accounting for field-aligned currents, these currents are assumed to be poloidal, and, therefore, the magnetic field can be expressed by: $\mathbf{B} = -\mathbf{r} \times \nabla \mathrm{V}$. Depending on whether it is considered an internal ($\mathrm{V}^{\mathrm{int}}$) or external ($\mathrm{V}^{\mathrm{ext}}$) magnetic source, the corresponding potential is described in spherical harmonics (SH):

$$\mathrm{V}^{\mathrm{int}} = a_0 \sum_{\ell=0}^{\ell_{\max}} \sum_{m=0}^{m_{\max}} \left(\frac{a_0}{r}\right)^{\ell+1} g_{\ell,m} Y_{\ell,m} \qquad \mathrm{V}^{\mathrm{ext}} = a_0 \sum_{\ell=0}^{\ell_{\max}} \sum_{m=0}^{m_{\max}} \left(\frac{r}{a_0}\right)^{\ell} g_{\ell,m} Y_{\ell,m}. \tag{2.18}$$

Here, $Y_{\ell,m}$ represent the spherical harmonics functions of degree ℓ and order m using a Schmidt semi-normalization and excluded Condon-Shortley phase. Accordingly, the $g_{\ell,m}$ are the spherical harmonics coefficients. Lastly, r is the radius at which the potential is evaluated, and a_0 is a corresponding reference radius. Here, magnetic sources are expanded up to a maximum degree and order of $\ell_{\max}$ and $m_{\max}$ (given in Table A.1).

During the Kalman filter's forecast step, the dynamic of the geomagnetic field and its components must be modeled, and proper prior characterization of the individual sources is required. Due to the complexity of the system, direct simulations of the different geomagnetic field components are not feasible. Therefore, the spatio-temporal evolution of the different magnetic sources is prescribed by autoregressive processes (Gillet et al., 2013). An autoregressive process (ARP) is a simple stochastic equation describing certain time-varying processes. Hence, each magnetic source is predicted by its own ARP, which

can be written in the following general form:

$$\mathbf{z}_s(t + \Delta t) = F_s(\Delta t)\mathbf{z}_s(t) + \boldsymbol{\xi}, \tag{2.19}$$

where $\mathbf{z}_s$ characterizes each source by a vector of SH coefficients, F_s describes the ARP parameter, and $\boldsymbol{\xi}$ is a Gaussian white noise. The ARP parameter F_s results from a scale-dependent and source-specific characteristic time. The Gaussian noise $\boldsymbol{\xi}$ is spatially described through stationary covariance matrices corresponding to each source. Thus, the ARP dynamics of each source are fully defined by the characteristic time and the covariance matrix. The covariance matrices, in turn, are derived from prior energy spectra. The shape of an energy spectrum of a corresponding source is assumed to be either flat or C-based, as proposed by Holschneider et al. (2016). The basic characteristic time scales and ARP parameters for the considered sources are listed in the Appendix A.3. For more details about ARP parametrization used in Kalmag, see Baerenzung et al. (2022).

Table 2.1: Magnetic sources considered in the Kalmag model

Magnetic source	$\ell_{\max}$	$m_{\max}$
Core	20	$\ell_{\max}$
Lithospheric	75	$\ell_{\max}$
Residual ionospheric/induced	50	1
Close magnetospheric	1	1
Remote magnetospheric	15	0
Fluctuating magnetospheric	15	0
Field-aligned currents	15	1

2.2.4 Ocean-induced magnetic source

To account for the OIMF, the Kalmag model has been extended by another internal source. As stated before, one commonly distinguishes between two types of OIMFs: the one associated with tidal motion and the one caused by ocean circulation. In the context of this thesis, the focus lies on the magnetic field generated by global ocean circulation. Regarding the separation of the oceanic component from the other geomagnetic field contributions, there is a clear advantage of tidal-induced magnetic signals due to the well-known temporal behavior of oceanic tides. The magnetic field induced by tides is strongly constrained by tidal frequencies. In contrast, the temporal behavior of magnetic signals induced by ocean circulation is much more complex and cannot be characterized by a single frequency. Even though both tidal and circulation-induced magnetic fields are of comparable amplitude, this fundamental difference makes separating magnetic signals

induced by circulation a much more demanding task. For one thing, this is why tidal magnetic signals have already been successfully extracted from CHAMP and Swarm satellite data before (Tyler et al., 2003; Sabaka et al., 2016, 2018, 2020), and magnetic signals from ocean circulation have not yet been identified in satellite observations. Secondly, this emphasizes the need for a different approach to characterize the oceanic source for the separation in the Kalmag model. Indeed, different extensions of the Kalmag model have been performed for both tidal and circulation-induced EM signals.

Tidal-induced EM signals

An extension of the Kalmag model for tidal-induced EM signals was performed and successfully used to extract these signals from satellite magnetometer observations of CHAMP and Swarm in (Saynisch-Wagner et al., 2021). Contrary to the other magnetic contributions in the Kalmag model, the tidal-induced magnetic source is not characterized using autoregressive processes. Instead, the harmonic tidal signals are described entirely by their frequency. Additionally, only an initial first guess of the spherical harmonic power spectra is assumed. Furthermore, physical ocean properties influencing the tidal EM signal (e.g., oceanic conductivity) are assumed to be static. Therefore, instead of the potential in Equation (2.17), the tidal-induced magnetic field can be described by the following potential using a superposition of a cosine (real) part and a sine (imaginary) part:

$$\mathrm{V} = a_0 \sum_{\ell=0}^{\ell_{\max}} \sum_{m=0}^{m=\ell} \left(\frac{a_0}{r}\right)^{\ell+1} g^c_{\ell,m} Y_{\ell,m} \cos(\omega t) + a_0 \sum_{\ell=0}^{\ell_{\max}} \sum_{m=0}^{m=\ell} \left(\frac{a_0}{r}\right)^{\ell+1} g^s_{\ell,m} Y_{\ell,m} \sin(\omega t), \quad (2.20)$$

whereby $g^c_{\ell,m}$ and $g^s_{\ell,m}$ are the spherical harmonic coefficients for the cosine and sine part, respectively. This tidal potential is assumed to be static over the assimilation period. Different tidal constituents are only described by their period of harmonic oscillation through the specific angular frequency ω. Subsequently, the real and imaginary parts can be used to derive the amplitude and phase of the extracted tidal signal. This way, the Kalmag model was used to simultaneously estimate the ocean-induced magnetic signals by eight major tides up to a spatial resolution of SH degree of 30 (Saynisch-Wagner et al., 2021). Thereby, the Kalman filter-based approach already showed its particular value since, for the first time, also a robust posterior error distribution for the tidal OIMF could be derived.

Circulation-induced EM signals

The ocean-circulation-induced EM signals can neither be sufficiently characterized by an autoregressive process nor a specific frequency. However, an adequate temporal prior

characterization of circulation-induced EM signals is crucial to separate these from other magnetic sources. Therefore, the extension of the Kalmag model by a source accounting for the OIMF by circulation must be performed differently. For this purpose, the novel KREMS was developed in this thesis.

In this method, the entire temporal behavior of the searched signals is characterized via a given presumed estimate. This way, complex temporal patterns from the irregular ocean flow can be prescribed and used as prior characterization instead of only a specific frequency, as with tidal-induced EM signals. Hence, Kalmag is extended by a magnetic source where prior estimated proxies of the OIMF are imposed to predict and constrain the temporal behavior. The Kalman filter is then used to locally rescale the given presumed estimates by a temporal constant factor. Thus, local corrections of the amplitude of these presumed estimates are determined by assimilating geomagnetic observations. The aim is to use these local scale factors as a measure of detectability and to evaluate the signal identification of the presumed estimates in geomagnetic observations. The implementation of this idea is described and extensively studied in Chapter 4 of the thesis.

2.3 Observation-based estimates of the ocean-induced magnetic field

2.3.1 Basic idea

As outlined in Section 2.2.4, the proposed KREMS used to investigate the detectability of ocean-circulation-induced magnetic fields relies on presumed estimates of the OIMF. In the first place, these presumed OIMF estimates are taken from ocean model data. However, this thesis additionally examines the possibility of using KREMS with observation-based instead of model-based OIMF estimates, which would allow for a purely observation-based identification of circulation-induced EM signals. The basic idea is to obtain a rough estimate of the OIMF by circulation from independent non-geomagnetic observations and subsequently use this to constrain the temporal behavior. This thesis investigates obtaining such a first OIMF estimate using independent observations from satellite altimetry, as already proposed by Saynisch et al. (2018).

2.3.2 Satellite altimetry

In satellite altimetry, the altimeter range, which is the distance between the satellite and the Earth's surface, is measured using radar. This allows the determination of the sea surface height related to a reference ellipsoid, which can be calculated from the difference

in satellite altitude and the altimeter range. The sea surface height is used to determine sea level anomalies (SLA) with respect to the mean dynamic topography (MDT), which is the temporal mean sea surface height over a certain period and the reference surface for altimetry (e.g. Rio et al., 2011; Mulet et al., 2021). Finally, the SLA is used to obtain the absolute dynamic topography (ADT), which is the instantaneous height over a geoid (equipotential surface corresponding to an ocean at rest) and contains information on the ocean dynamics (Stammer and Cazenave, 2018). The ocean dynamics can then be further specified using the ADT and the geostrophic approximation, as explained in the following subsection. The first satellite altimetry mission started already in the 1970s with GEOS-3 (Stanley, 1979) and SeaSat (Grantham et al., 1977). At the latest, since the TOPEX/POSEIDON missions (Fu et al., 1994) in the 1990s, satellite altimetry has been widely used to monitor ocean dynamics (Stammer and Cazenave, 2018; Le Traon, 2013). Since then, various applications of satellite altimetry have evolved and demonstrated the benefit of altimetry measurements (Eldardiry et al., 2022).

2.3.3 Geostrophic approximation

Satellite altimetry provides global measurements of the sea surface height. However, oceanic velocities are required for estimating the OIMF. Consequently, these ocean velocities must first be derived from sea surface height data in order to predict ocean-induced EM signals from satellite altimetry measurements. For this purpose, the geostrophic approximation is assumed. The geostrophic approximation is already widely used to obtain ocean velocities from sea surface height measurements (Holton and Hakim, 2013; Ivchenko et al., 2011; Doglioni et al., 2023). This approximation assumes a so-called geostrophic balance between horizontal pressure gradients and the Coriolis force. Under the assumption of a steady state of the ocean (ocean velocities do not change with time) and assuming zero other forces (e.g., no friction), the geostrophic balance can be deduced from the equations of motion (see Appendix A.4 for a detailed derivation). The approximations are justified for large-scale mean circulation in the ocean's interior (Pond and Pickard, 1983): Finally, the geostrophic balance can be expressed by (Gill, 1982; Stammer and Cazenave, 2018):

$$f\mathbf{v}_x^{\text{geo}} = -\frac{1}{\rho}\frac{\partial p}{\partial y} \qquad f\mathbf{v}_y^{\text{geo}} = \frac{1}{\rho}\frac{\partial p}{\partial x}, \tag{2.21}$$

where $\mathbf{v}_x^{\text{geo}}$ and $\mathbf{v}_y^{\text{geo}}$ are the desired zonal and meridional geostrophic velocity, $f = 2\Omega \sin\phi$ describes the Coriolis parameter (where Ω is the magnitude of the angular velocity of the Earth's rotation and ϕ the geographical latitude), ρ represents the density and p denotes the pressure. However, horizontal pressure gradients cannot be measured in-situ and must

be linked to the sea surface elevation in order to be accessible by satellite altimetry. In fact, assuming that density is constant and pressure is proportional to depth, one can relate the pressure gradients in Equation (2.21) to slopes of sea surface elevation (see again Appendix A.4 for more details), yielding (Stammer and Cazenave, 2018):

$$\mathbf{v}_x^{\mathrm{geo,s}} = -\frac{g}{f}\frac{\partial \eta}{\partial y} \qquad \mathbf{v}_y^{\mathrm{geo,s}} = \frac{g}{f}\frac{\partial \eta}{\partial x}, \tag{2.22}$$

where η describes the sea surface height, respectively ADT, and g the Earth's gravitational acceleration. Equation (2.22) eventually allows estimating geostrophic surface velocities from sea surface height measured by satellite altimetry.

In conclusion, the geostrophic balance is sketched in Figure 2.5. The figure highlights the link between sea surface height and pressure and illustrates the ocean flow orthogonal to the resulting pressure gradients.

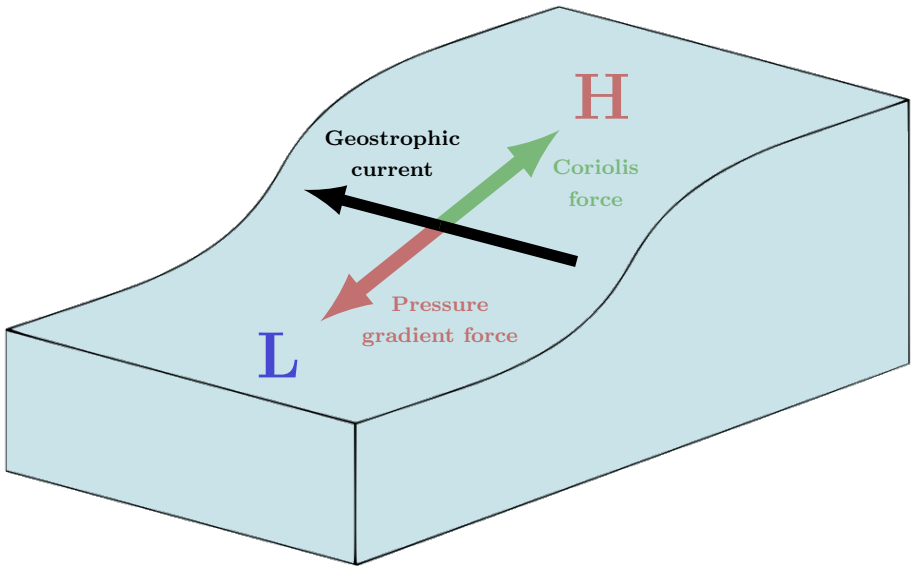

Figure 2.5: Sketch illustrating the geostrophic balance. The pressure gradient force (red arrow) is balanced by the Coriolis force (green arrow). The resulting movement of the water is a geostrophic current (black arrow) proportional and orthogonal to the pressure gradient. High-pressure areas can be linked to high sea surface elevation (H) and low-pressure areas with low sea surface elevation (L).

Finally, according to Equation (2.12), the geostrophic surface velocities derived from sea surface height are combined with the oceanic conductivity and used to derive an external electric current density. Although this represents a strong simplification, it first poses a rough estimate of the OIMF. It has to be noted that the goal is to estimate the temporal behavior rather an accurate amplitude for the application with KREMS. The approach to obtain OIMF estimates using the geostrophic approximation is validated and examined in more detail in Section 3.3.

2.3.4 Combination of satellite altimetry with in-situ observations

The geostrophic velocities estimated using Equation (2.22) are limited to the surface. Therfore, geostrophic transport estimations can be improved by complementing sea surface height observations with in situ measurements (Stammer and Cazenave, 2018). The additional measurements used for a better estimation of the geostrophic velocity at any depth and allow generating 3D geostrophic currents (Vigo et al., 2018). Instead of assuming that density is constant with depth, additional in-situ measurements of ocean temperature, salinity, and pressure are used to obtain the density ρ. For example, such in situ temperature and salinity profiles can be measured by Argo floats (Wong et al., 2020). The geostrophic velocities with respect to a reference velocity can then be calculated by the thermal wind equation:

$$\mathbf{v}_x^{\mathrm{geo}}(z) = \frac{g}{\rho f}\int_{z_0}^{z}\frac{\mathrm{d}\rho}{\partial y}\,dz + \mathbf{v}_x^0 \qquad \mathbf{v}_y^{\mathrm{geo}}(z) = -\frac{g}{\rho f}\int_{z_0}^{z}\frac{\partial\rho}{\partial x}\,dz + \mathbf{v}_y^0, \tag{2.23}$$

where v_x^0 and v_y^0 are the zonal and meridional velocities at reference depth z_0, which in the case of altimetry would be the surface velocity. This combination of satellite altimetry observations and in situ measurements is widely used to estimate oceanic geostrophic transports (Gray and Riser, 2015; de Verdière and Michel Ollitrault, 2016; Ollitrault and de Verdière, 2014; K. et al., 2007). These obtained geostrophic transports provide an opportunity to estimate the OIMF, in particular, the combination with temperature and salinity measurements is advantageous since these also allow the calculation of the required oceanic conductivity.

3

Datasets and preparatory studies

3.1 Datasets

The calculations of the OIMF in this thesis rely on various datasets of different types ranging from numerical models to in-situ and satellite observations. The following section introduces and briefly describes these datasets. Each dataset provides a distinct set of variables with specific spatial and temporal resolutions and with a particular number of depth layers. On the one hand, for ocean-model-based OIMF calculations, the data is taken either from an Estimating the Circulation and Climate of the Ocean, Phase II (ECCO2) project or a Global Ocean Ensemble Reanalysis (GLOCER), which are both based on an ocean general circulation model (OGCM). On the other hand, for observation-based OIMF calculations, the data are taken from the Data Unification and Altimeter Combination System (DUACS) or a Multi-Observational Global Ocean Product (ARMOR3D), which are both based on altimetry observations and in case of the ARMOR3D product additionally in-situ observations. Finally, the ocean conductivity can additionally also be taken from the World Ocean Atlas 2018 (WOA18). An overview of the used datasets is given in Table 3.1. For each dataset, the original spatial resolution was reduced by interpolation through conservative remapping onto a 1° grid before the OIMF calculation. Typically, a data period of 7 years is considered (from 2014.0 until 2021.0) corresponding to the Swarm satellite mission. However, the provided temporal resolution and the considered depth layers of the datasets vary.

Table 3.1: Datasets used in this thesis

Dataset	Source/Type	Temporal resoultion	Depth levels	Variables
ECCO2 Estimating the Circulation and Climate of the Ocean (ECCO2, 2022)	Numerical model	3-daily	50	T, S $\mathbf{v}_x$, $\mathbf{v}_y$
GLOCER Global Ocean Ensemble Reanalysis (GLOCER, 2022)	Numerical model	daily	75	T, S, η $\mathbf{v}_x$, $\mathbf{v}_y$
DUACS Data Unification and Altimeter Combination System (DUACS, 2022)	Satellite observations	daily	1	$\mathbf{v}_x^{\text{geo}}$,$\mathbf{v}_y^{\text{geo}}$
ARMOR3D Multi-Observation Global Ocean Product (ARMOR3D, 2022)	In-situ & satellite observations	weekly	50	T, S $\mathbf{v}_x^{\text{geo}}$,$\mathbf{v}_y^{\text{geo}}$
WOA18 World Ocean Atlas 2018 (WOA18, 2019)	In-situ observations	climatological mean	102	σ

ECCO2

The ECCO2 dataset (ECCO2, 2022) is provided by the Jet Propulsion Laboratory (JPL). The ECCO2 model uses a Green's function approach to estimate the ocean state (Menemenlis et al., 2005) and is constrained by several in-situ and remote observational data (Menemenlis et al., 2008). In this thesis the *cube92* model output of ECCO2 is used. The 3D output fields of the ocean model have been provided as 3-day averages on 50 depth levels. The OIMF calculations made use of the four oceanic variables: zonal and meridional velocity ($\mathbf{v}_x$,$\mathbf{v}_y$), as well as temperature (T) and salinity (S), which can be used to obtain oceanic conductivity.

GLOCER

The GLOCER dataset (GLOCER, 2022) is taken from Copernicus Marine Environment Monitoring Service (CMEMS). This global ocean reanalysis dataset consists of an ensemble of three homogeneous gridded descriptions of the physical state of the ocean. The

reanalyses are based on the numerical OGCM of the Nucleus for European Modelling of the Ocean (NEMO) (Gurvan et al., 2022) framework and are constrained with data assimilation of satellite and in-situ observations. The dataset provides 3D output fields from zonal and meridional velocities as well as temperature and salinity as daily averages on 75 vertical depth levels. Additionally, the sea surface height is available as a daily 2D output field. In this thesis, an ensemble of three members is considered (listed in Table 3.2): The Ocean Reanalysis System 5 (ORAS5) (Zuo et al., 2017, 2019) from the European Centre for Medium-Range Weather Forecasts (ECMWF), the Global Seasonal forecast system (GloSea5) (MacLachlan et al., 2015; Blockley et al., 2014) from the Met Office, and the Global Ocean Reanalysis and Simulation (GLORYS) (Ferry et al., 2010) from Mercator Ocean International organization. The individual reanalyses slightly differ in surface forcing (e.g., sea surface temperature (SST) or sea surface salinity (SSS)) the used assimilation system (NEMOVAR, Mogensen and Balmaseda (2012) or SEEK, Pham et al. (1998)), and corresponding assimilation window (one to seven days). The differences are summarized in Table 3.2 and further details can be found in Desportes et al. (2022).

Table 3.2: Considered ensemble members of the GLOCER dataset

Ensemble member	Production center	Surface Forcing	Assimilation
ORAS5	ECMWF	No surface nudging	5-day NEMOVAR
GloSea5	Met Office	SST and SSS	1-day NEMOVAR
GLORYS	Mercator Ocean	Surface waves forcing, SST and SSS	7-day SEEK

DUACS

The Sea Level Thematic Assembly Center (SL TAC) from the CMEMS, as part of the DUACS, provides a comprehensive dataset of sea surface height observations (DUACS, 2022). In this dataset, different altimeter missions are combined. Along-track measurements of sea level anomalies (SLA) with respect to a twenty-year mean (1993-2012) are taken to produce gridded data using optimal interpolation (Pujol et al., 2016). In addition, the absolute dynamic topography (ADT) and especially the derived geostrophic currents (see Section 2.3.3) are also directly provided by the DUACS dataset. The 2D surface variables are available as daily averages (more detail can be found in Pujol et al. (2023)).

ARMOR3D

The ARMOR3D dataset (ARMOR3D, 2022) is a multiobservational ocean product also provided by CMEMS. This dataset combines satellite altimetry observations and in-situ temperature and salinity measurements (see Section 2.3.4). Satellite observations of sea surface temperature and sea surface salinity are used to derive synthetic temperature and salinity profiles with multiple linear regression and covariances deduced from historical observations (Guinehut et al., 2012). These profiles are combined with in-situ observations using an optimal interpolation method (Bretherton et al., 1976). The temperature and salinity profiles are combined with geostrophic surface currents from altimetry to generate 3D geostrophic ocean velocities based on the thermal wind equation (2.23). Therefore, 3D output fields of temperature, salinity, and geostrophic ocean velocities are available as weekly averages on 50 depth levels (more details can be found in Greiner et al. (2021)).

3.2 Ocean-induced magnetic field studies

In order to investigate and evaluate the detectability, it is necessary to know and estimate possible influences, effects, and sources of error on the OIMF calculations. The following considers and quantifies the most important influences on these magnetic field calculations. Three major parts were investigated: First, the main influences on the electric current density as the source of the OIMF. Second, the influences of the surrounding conductance model, and third, the quasi-stationary approximation used with X3DG. Finally, a comparison to the simple OIMF estimation from Biot-Savart is drawn.

3.2.1 Influences of electric current density

As described in Section 2.1, the electric current density depends on three physical quantities (Equation (2.11)): The oceanic conductivity σ, the oceanic velocities $\mathbf{v}$, and the Earth's main magnetic field $\mathbf{B}^{\text{earth}}$. All three quantities are subject to temporal variations: ocean conductivity due to temperature and salinity changes in the ocean, oceanic velocities or rather transports due to the general wind-driven ocean circulation, and the Earth's magnetic field due to changes known as secular geomagnetic variation (Aubert et al., 2013). These temporal variations are crucial for the detectability of ocean circulation-induced EM signals. Therefore, it is essential to know the three quantities' influences on the variability of electric current density and the resulting magnetic field.

The daily time series of the ensemble mean of the GLOCER dataset was used to inverstigate this in a preparatory study. The OIMF was calculated in three different ways to study the influence of the three quantities separately. The variations due to ocean

conductivity (σ - variations) was investigated by varying only the ocean conductivity when calculating the electric current density and assuming constant mean values for the oceanic velocities and the Earth's magnetic field. On the other hand, when investigating the variations due to oceanic transports ($\mathbf{v}$ - variations), only the oceanic velocities were varied daily, and the conductivity and the Earth's magnetic field were assumed to be constant. Finally, only the Earth's magnetic field was varied ($\mathbf{B}^{\text{earth}}$- variations), and oceanic conductivity and velocities were assumed to be constant over the considered period.

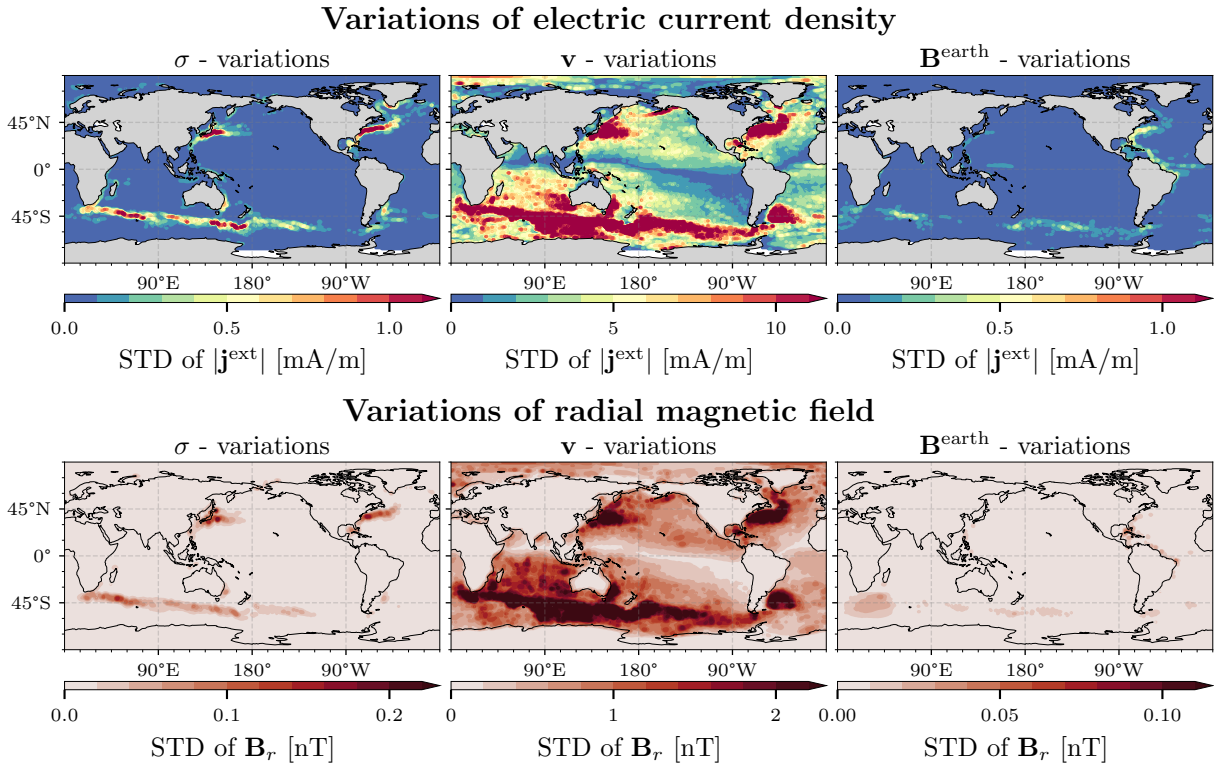

Figure 3.1: Influence of external electric current density variations on the radial component of the OIMF. Different variations due to conductivity σ (left), oceanic velocities $\mathbf{v}$ (middle), and Earth's magnetic field $\mathbf{B}_{\text{earth}}$ (right) on the electric current density and its resulting radial OIMF are considered. At the top, the standard deviation of the electric current density (STD of $\mathbf{j}^{\text{ext}}$) is shown when only the specified quantity (σ, $\mathbf{v}$ or $\mathbf{B}^{\text{earth}}$) is varied. At the bottom, the corresponding standard deviation of the radial OIMF (STD of $\mathbf{B}_r$) is displayed. Note the different plotting ranges for each quantity.

Figure 3.1 summarizes the resulting variations in the electric current density. The variability of the electric current density is illustrated by the standard deviation over the considered period of 7 years. Figure 3.1 (top row) clearly shows that the variability caused by temporal variations in oceanic transports has the most significant influence on the electric current density. Variations caused by conductivity changes are an order of magnitude smaller. Nevertheless, for example, seasonal temperature variations can also cause significant changes in electrical conductivity. Temporal variations due to the

secular variation of the Earth's magnetic field turn out to be the smallest and have only a minimal influence on the variability of the electric current density. The larger temporal scales of the secular geomagnetic variation compared to the considered period of 7 years can explain this small influence of the Earth's magnetic field variations.

Finally, Figure 3.1 also shows the variability of the corresponding radial magnetic field (STD of $\mathbf{B}_r$). As expected, the major part of the OIMF variability is caused by variations in oceanic transports. The variations due to ocean conductivity are again an order of magnitude smaller but still within the range of measurement accuracy of high-precision magnetometers (0.1 nT) used in satellite missions like Swarm. However, the fluctuations due to secular variation are much smaller and below the current measurement accuracy. The main conclusion from this preparatory study is that the temporal variations of the OIMF are dominated by oceanic transports.

3.2.2 Influences of the conductance model

As described in Section 2.1 (see also Figure 2.2), the conductance model consists of two parts: A 2D ocean conductance layer and a 1D mantle conductivity profile. The two components were varied to determine the influence of the conductance model, and the resulting changes on the OIMF were determined. For this test calculations, the ocean model data from the GLOCER data set was used. Two different ocean conductance layers were considered. First, an ocean conductance layer was calculated from the temperature and salinity of the ocean model data (as described in Section 2.1.2). Second, another conductance layer was obtained from a globally uniform constant ocean conductivity of 3.3 S/m (volumetrically weighted mean of the global ocean conductivity, Tyler et al. (2017)). In both cases, the OIMF was calculated at sea surface height using X3DG. Figure 3.2 shows the difference in the ocean conductance (top left) and the corresponding difference in the resulting OIMF (top right). In particular, near the coast, the OIMF exhibit significant deviations caused by the differences in the ocean conductance layers. The magnetic field differences can be in the order of several nT locally. This mainly shows that the lateral conductivity differences are important and influence the radial OIMF decisively by coupling poloidal and toroidal components.

Finally, in another test, the assumed mantle conductivity was varied. Instead of the commonly used conductivity profile of Grayver et al. (2017), the OIMF was also calculated with the conductivity profile of Püthe et al. (2015). Both 1D conductivity profiles are shown in the bottom left plot of Figure 3.2. The corresponding resulting differences in the OIMF are presented in the bottom right plot of Figure 3.2. The mantle conductivity mainly influences the penetration depth of the OIMF. Therefore, the differences are more related to the OIMF signal strength than land-ocean conductivity differences. The

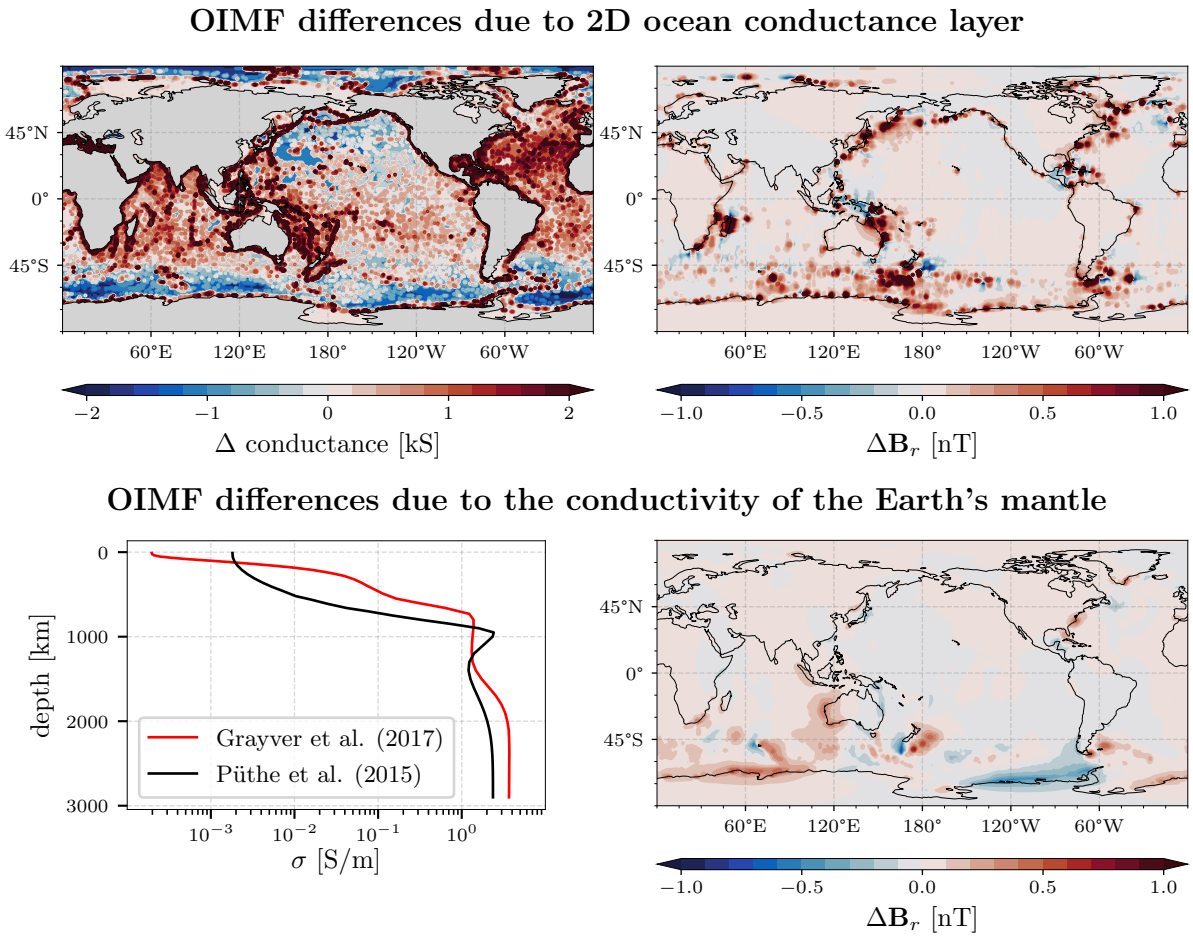

Figure 3.2: Influence of the assumed ocean conductance model on the OIMF calculations. Differences in the OIMF due to variations in the 2D ocean conductance layer (top row) and due to the Earth's mantle conductivity (bottom row) are shown. The left side shows the different model assumptions: difference in the assumed ocean conductance (top) and different mantle conductivities (bottom). The right side shows the corresponding resulting differences in the OIMF.

differences in the OIMF are also smaller than those caused by the 2D conductivity layer but can still reach values up to 0.5 nT. Overall, this preparatory study shows that the surrounding conductance model can significantly influence the calculation of the OIMF and must therefore be considered a major source of error.

3.2.3 Quasi-stationary approximation

As stated in Section 2.1.2, the quasi-stationary case is simulated in X3DG using an excitation frequency smaller than $10^{-12}\,\mathrm{days}^{-1}$. This criterion was determined in a preparatory study, where the OIMF was calculated from ECCO2 data using different excitation fre-

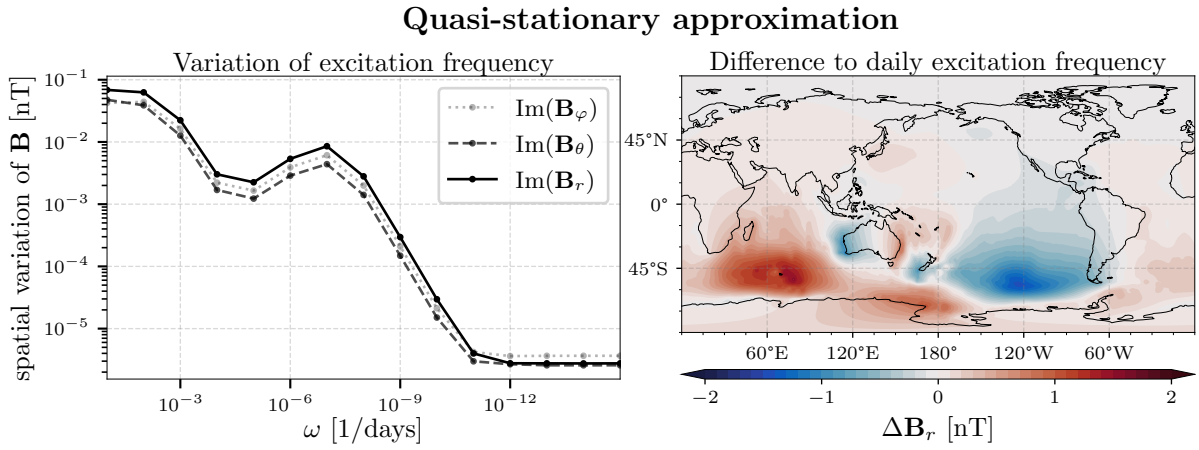

Figure 3.3: The left side shows the spatial variations of the imaginary part of the magnetic field in dependence on the excitation frequency ω used in X3DG. The right side shows the differences between the radial magnetic field calculated with a daily excitatory frequency and the quasi-stationary approximation.

quencies in X3DG. For each excitation frequency, the imaginary part of the corresponding magnetic field solution was considered to examine wheather the quasi-stationary case is justified. In the stationary case, any spatial variation of the imaginary part should vanish. Therefore, Figure 3.3 presents the spatial variation of the imaginary part for all magnetic field components dependent on the corresponding excitation frequency. From Figure 3.3 (left plot) can be seen that spatial variations of the imaginary part decrease for smaller frequencies until $10^{-12}\,\text{days}^{-1}$. Accordingly, the excitation frequency must be chosen larger to satisfy a quasi-stationary regime.

However, the quasi-stationary approximation introduces some errors since the magnetic field calculation is assumed frequency independent. The shortest time intervals considered in this thesis are daily. Therefore, the spatial difference between the radial magnetic field calculated with a daily excitation frequency and using the quasi-stationary approximation is calculated. The differences are shown in Figure 3.3 (right plot) and serve as an extreme estimation of error which can occur in a single frequency band due to the quasi-stationary approximation. The deviations decrease for lower frequencies and are already halved for a weekly excitation frequency (see Appendix A.5 for additional plots). It should be noted that the magnetic field in this study was calculated again on surface height, and the error at satellite height is reduced. Nevertheless, minor inaccuracies are introduced, especially for higher frequencies due to the quasi-stationary approximation.

3.2.4 Comparison between X3DG and Biot-Savart solver

Apart from the OIMF calculations using the complete Maxwell solver X3DG, the law of Biot-Savart (Equation (2.13)) allows for a simplified and approximate estimate of the OIMF. As shortly introduced in Section 2.1.3, the Biot-Savart approach does not consider the surrounding conductivity and, therefore not consider the coupling between the poloidal and toroidal magnetic field components. On the one hand, this poses an inaccurate electromagnetic framework; on the other hand, this simplifies the OIMF calculations and would facilitate a future inversion of the OIMF.

In order to investigate the deviations due to this simplified approach, the OIMF calculated using Biot-Savart is compared to the solutions obtained from the electromagnetic induction solver X3DG. In both cases, the OIMF is derived from a complete time series of the electric current density resulting from the ECCO2 model. The temporal mean of the radial OIMF ($\overline{\mathbf{B}}_r$)at surface height and spatial resolution of SH degree 30 are shown for both calculations in Figure 3.4 (top row).

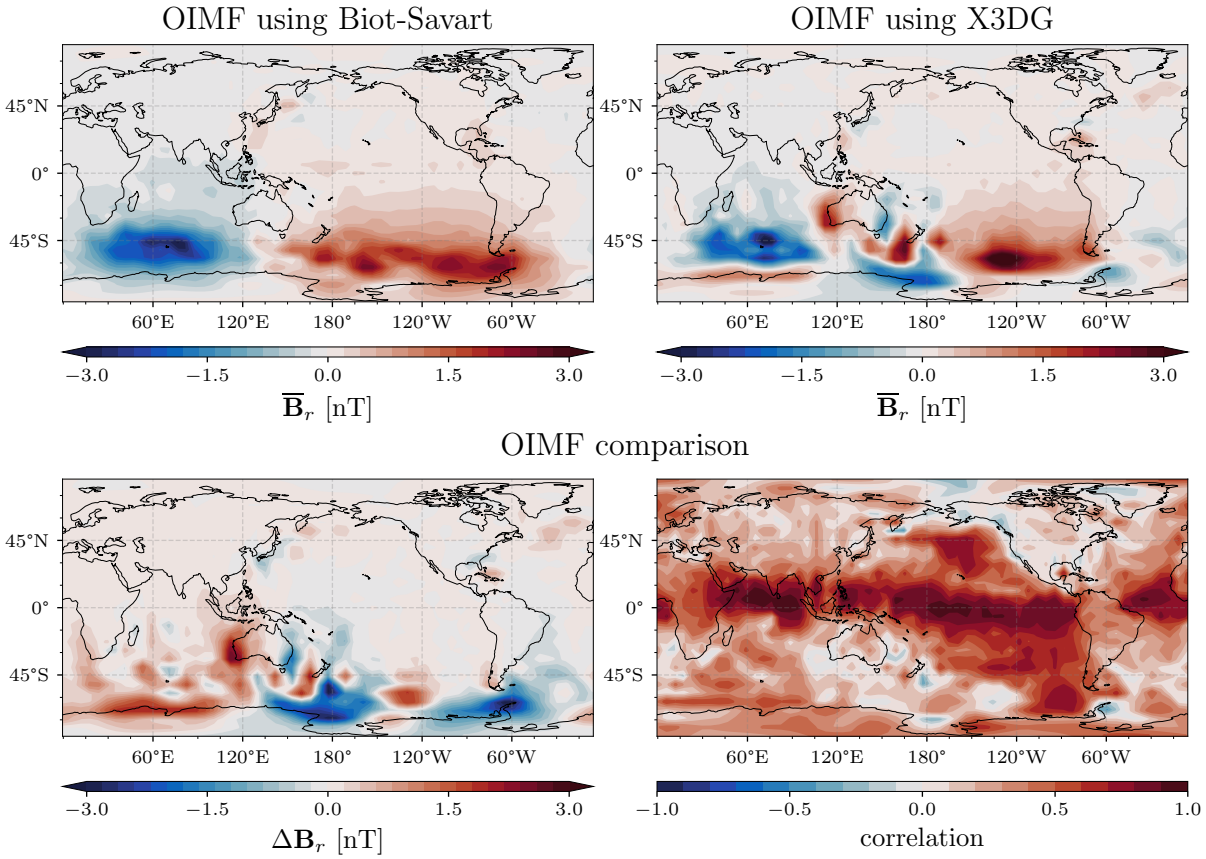

Figure 3.4: Comparison of the OIMF resulting from the Biot-Savart approximation and from the electromagnetic induction solver X3DG. On the top, both temporal means of the radial OIMF are shown. On the bottom, the difference (left) between both fields and their correlation (right) are shown.

In this comparison, two aspects are of interest, namely the extent of the inaccuracies and the question of whether the temporal behavior can still be sufficiently described by the Biot-Savart approach. The differences in the mean radial magnetic field (bottom left plot in Figure 3.4) quantify the inaccuracies and illustrate a maximal error due to an inaccurate electromagnetic framework. The OIMF calculated by the law of Biot-Savart captures the large-scale dipole caused by the Antarctic Circumpolar Current (ACC). The global average of the mean absolute difference is 0.3 nT. However, deviations at medium and smaller scales are clearly visible. Most notably, larger deviations occur in the southern ocean around Australia and New Zealand caused by the unaccounted effect of lateral conductivity variations between coastal and marine areas. The magnitude of the radial OIMF can deviate in some areas by about up to 3 nT, although the same electric current density is used for both calculations. The correlation between both radial magnetic fields (bottom right plot in Figure 3.4) indicates the similarities in temporal behavior. The correlation ranging from -0.56 to 0.96 with a global average of 0.41 emphasizes a good agreement in temporal behavior in some larger parts of the ocean (e.g., the Pacific Ocean). However, areas with more significant deviations (e.g., the Southern Ocean around Australia) also reveal a lower correlation (average correlation in the Southern Ocean is 0.24). Additionally, it should be noted that the highest correlation arises around the equator, where the ocean-induced magnetic signal is typically very low. This comparison justifies using the Biot-Savart approach only as a rough approximation and indicates already areas of significant deviations in both spatial and temporal patterns due to the inaccurate electromagnetic framework.

3.3 Validation of observation-based ocean-induced magnetic field estimates

3.3.1 Model-based validation of the geostrophic approach

In Section 2.3.3, it was already proposed to use altimetry for estimating the temporal behavior of the large-scale OIMF from circulation. Thereby, the OIMF is estimated from sea surface height data, accessible by altimetry, based on the geostrophic approximation. In the following, this geostrophic approach to obtain the OIMF is first examined and validated in an entirely model-based framework according to Saynisch et al. (2018). For this purpose, the global ocean ensemble reanalysis (GLOCER) dataset from CMEMS is used to calculate the OIMF in two different ways. First, for the geostrophic approach, the OIMF is derived from sea surface height data of the GLOCER ensemble mean, mimicking altimetric observations (geostrophic OIMF). Second, as a comparison, the OIMF is derived

directly from the ocean velocities of the GLOCER ensemble (full-model OIMF). Finally, both OIMF predictions are compared to validate the geostrophic approach (Figure 3.5 illustrates the validation framework).

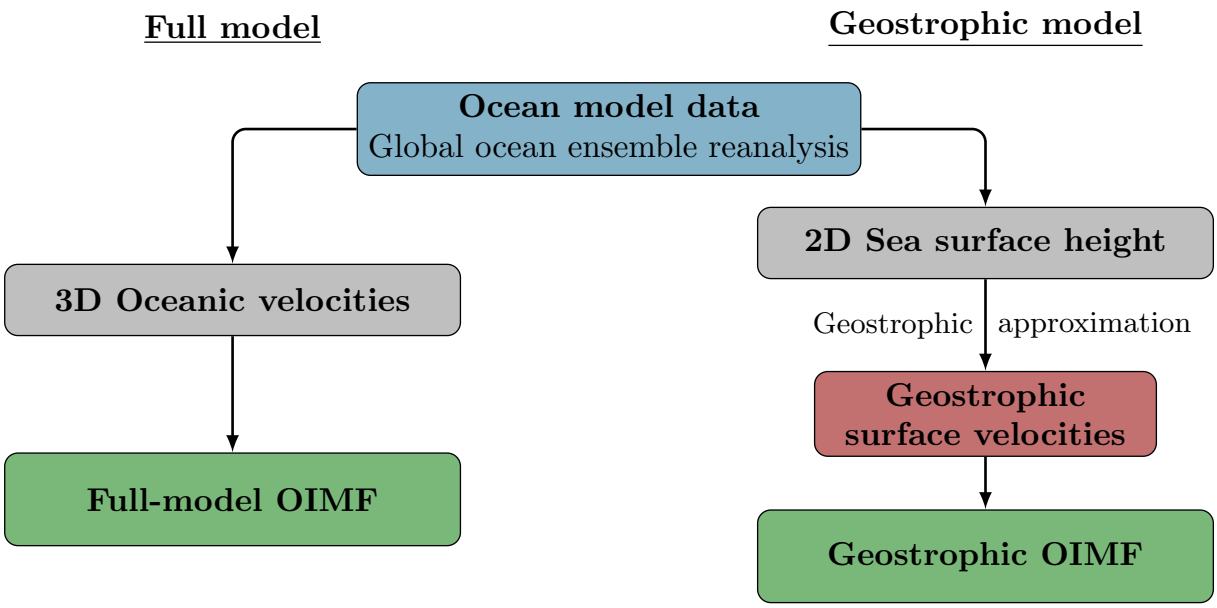

Figure 3.5: A sketch showing the setup of the two approaches to validate the geostrophic approach and the processing steps to obtain the geostrophic and the full-model OIMF.

According to Equation (2.22), in the geostrophic approach, the sea surface height will be converted into zonal and meridional geostrophic surface velocities (Equation (2.21)). Since the ocean-induced electromagnetic signal depends on the entire water column, these geostrophic surface currents are projected until the ocean bottom to obtain depth-integrated ocean velocities. Thereby, the geostrophic velocity is assumed to be constant over depth, which leads to an unrealistic overestimation of the geostrophic transports (i.e., depth-integrated ocean velocities). However, it should be noted the primary goal is more to estimate the temporal behavior rather than absolute values. The ocean depth is taken from the ETOPO1 dataset. In order to evaluate the geostrophic approach, the correlation between the geostrophic and the ocean full model-based transports is considered. The correlation is shown for both zonal and meridional directions in Figure 3.6 (top row).

Except for the equatorial area, zonal and meridional transports exhibit a high correlation, with a global average of 0.6 (for both zonal and meridional transports), demonstrating remarkable temporal correspondence. The invalidity of the geostrophic assumption due to the vanishing Coriolis force causes a lower correlation around the equator. This comparison indicates that sea surface height variations can describe the most temporal behavior of oceanic water transport in most areas.

Subsequently, these geostrophic transports are multiplied with the depth-weighted

averaged ocean conductivity (derived from salinity and temperature of the GLOCER dataset) to obtain the depth-integrated electric current density, which serves as input for X3DG. The geostrophic electric current density has to be preprocessed to avoid an exaggerated amplified magnetic signal around the equator due to the spatial expansion of the OIMF. A simple way to avoid such an extreme magnetic signal is to mask the geostrophic electric current density at latitudes below 7°. The resulting geostrophic OIMF is again compared to the full ocean-model-based OIMF by showing the correlation between both time series in Figure 3.6 (bottom left). In many parts of the oceans, a correlation of 0.8 is achieved, but the global average is 0.14.

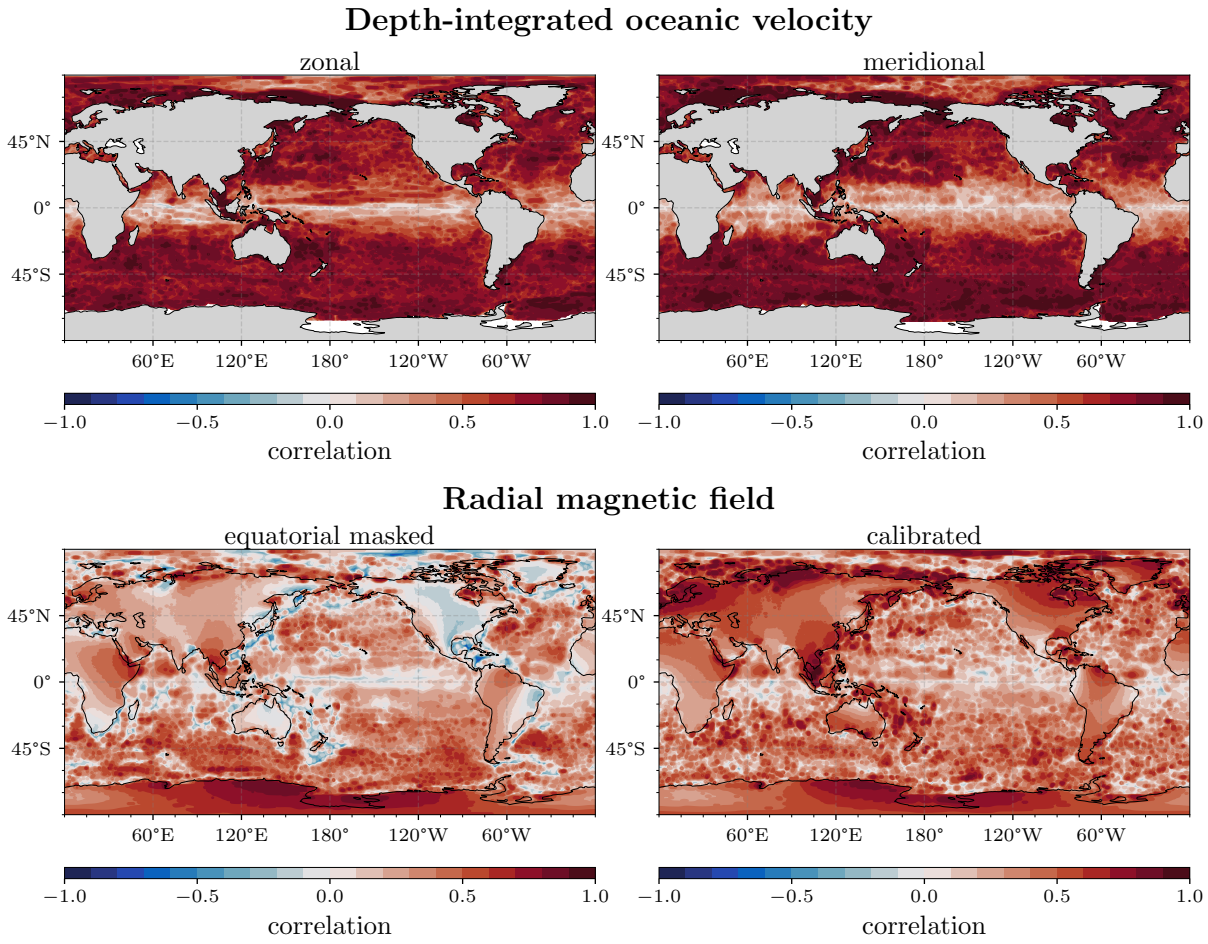

Figure 3.6: Comparison between geostrophic and full-model-based approach. The top row shows the correlation between the geostrophic (derived from sea surface height data) and the full-model-based depth-integrated ocean velocities for the zonal (left) and meridional (right) components. The bottom plots show the correlation between the corresponding OIMF. On the left side, the geostrophic electric current density is equatorial-masked, and on the right side, its complete time series was calibrated by linear rescaling.

A more advanced approach is calibrating the electric current density instead of simple equatorial masking. In doing so, an inadequate estimation caused by the inaccurate assumption of constant geostrophic velocity until the ocean's depth can be additionally corrected. The calibration can be performed by linearly rescaling the geostrophic electric current density to a model-based reference independently chosen from the comparison period. Here, such a rescaling is performed using the GLOCER data from the year 2013 (which is not included in the comparison period of 2014-2021). The calibration of the geostrophic electric current density is then determined through a least-square fit based on the following equation:

$$\mathbf{j}^{\text{model}}(t) \;=\; a \cdot \mathbf{j}^{\text{geo}}(t) + b, \tag{3.1}$$

where $\mathbf{j}^{\text{model}}$ and $\mathbf{j}^{\text{geo}}$ denote the model-based and geostrophic electric current density from year 2013, and a and b are the calibration parameters. These calibration parameters are finally used to rescale the complete time series of the electric current density and can be found in the Appendix A.6. Finally, the calibrated geostrophic OIMF resulting from the calibrated electric current density is once again compared to the full ocean-model-based OIMF, and their correlation is shown in Figure 3.6 (bottom right). A significantly higher correlation is visible when comparing the correlation of the calibrated versus the previous equatorial-masked OIMF with the full model-based OIMF (bottom row in Figure 3.6). The global average correlation increased from 0.14 to 0.27, emphasizing the improvement through the calibration using linear rescaling. However, it must be noted that the calibration depends again on model data.

In both cases, using an equatorial-masked or a calibrated electric current density, the geostrophic approach can estimate the temporal behavior of the OIMF to a large extent. Accordingly, this model-based validation justifies the geostrophic approach as an attempt to derive observation-based OIMF estimates. Three essential points can be concluded from this preparatory study: First, sea surface height variability explains large parts of the OIMF variability, and the geostrophic approach can be used to predict the temporal behavior of the ocean-circulation-induced EM signal in a first approximation. Second, the correlation of electric current densities derived by the geostrophic approach is significantly higher than the correlation of the corresponding radial magnetic field. Third, linear rescaling of the electric current density used as calibration can improve these predictions of the OIMF.

3.3.2 Observation-based validation of the geostrophic approach

After the purely model-based validation of the geostrophic approach, a short comparison with real observation-based data is given. In Section 3.1, two different datasets based on altimetry measurements are introduced. Firstly, the purely altimetry-based DUACS dataset providing the geostrophic surface currents, as described in Section 2.3.3, was considered. Secondly, since the model-based validation demonstrated that the geostrophic approach could be further improved (e.g., by calibrating the electric current density), the more advanced ARMOR3D dataset is considered. Therefore, the OIMF is derived from altimetry observations in combination with additional in-situ measurements based on the thermal wind equation (2.23). In doing so, the in-situ measurements are used to better project the geostrophic surface currents into the ocean depth, which results in a more realistic estimation of the oceanic transports.

As in the model-based validation, the observation-based OIMF estimates from DUACS and ARMOR3D are compared with the ensemble mean of the ocean reanalysis dataset GLOCER. The correlations of both radial magnetic fields with the model-based OIMF are slightly smaller than those obtained before in the model-based validation. Although the global average correlations of 0.12 (DUACS) and 0.13 (ARMOR3D) are rather low, the temporal behavior is in good agreement in decisive parts of the ocean (e.g., the Southern Ocean and the area of the Antarctic Circumpolar Current), achieving correlations of 0.82 (DUACS) and 0.77 (AMRO3D). The correlation for both observation-based OIMF estimates are shown in the Appendix A.7.

Neither the observation-based OIMF derived from DUACS nor the one derived from ARMOR3D show a significantly better temporal agreement with the OIMF derived from GLOCER since both originate from similar altimetry data. However, the amplitude of the OIMF estimate derived from DUACS deviates significantly more prominent from the model-based OIMF than the OIMF derived from ARMOR3D. This deviation is illustrated by the root-mean-square-deviation (RMSD) between the time series of the observation-based and the model-based OIMF, which is presented in Figure 3.7. The global average RMSD between the OIMF from DUACS and the OIMF from GLOCER is 1.96 nT, whereas the global average RMSD between the OIMF from ARMOR3D and the OIMF from GLOCER is 0.69 nT. This reduction of the RMSD of about 1.27 nT reveals the improvement by using multiobservational data.

Generally, the observation-based estimates also confirm the potential to derive a realistic temporal behavior of the OIMF from the altimetry data. In particular, this comparison shows that observation-based OIMF estimates can be further improved by the combination with in-situ measurements. However, the improvements due to in-situ measurements affect more the amplitude of the magnetic field than the temporal behavior.

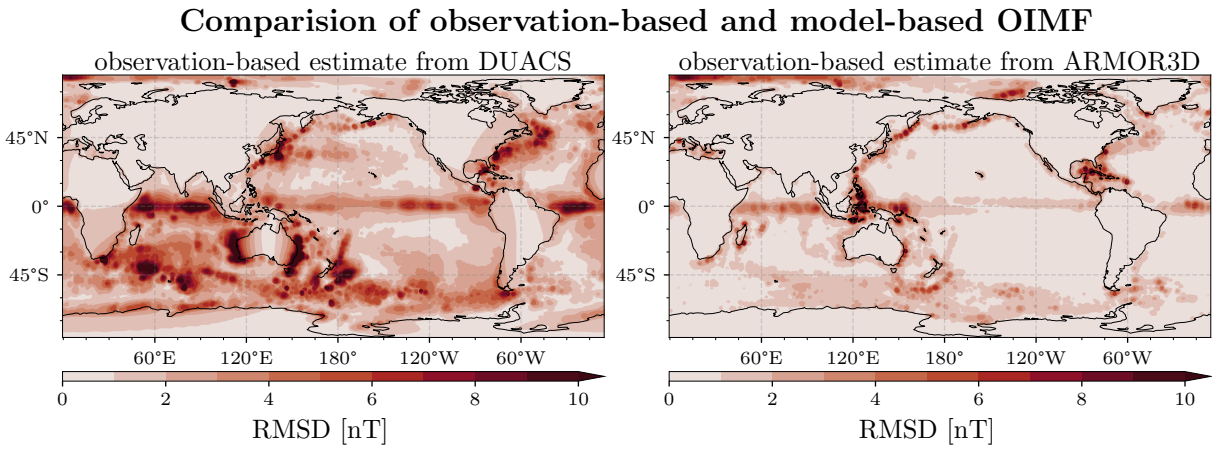

Figure 3.7: The RMSD between the time series of the observation-based and model-based OIMF estimates. The observation-based OIMF is derived either from the DUACS dataset (left side) or the ARMOR3D dataset (right side), while the model-based OIMF is derived from the GLOCER dataset.

4

A magnetic field observation system simulator

4.1 Design of the observation system simulator

4.1.1 Basic concept

The idea of using Kalman-filter-based rescaling of EM signals (KREMS) to identify magnetic signals induced by ocean circulation in geomagnetic satellite observations was introduced in Section 2.2.4. The following chapter introduces KREMS in detail and describes the approach as a detection method of ocean-circulation-induced EM signals in geomagnetic satellite observations. To validate the suggested method and to extensively study the advantages and limitations of this approach, an observing system simulation experiment (OSSE) was performed. Hence, the OSSE is presented in this chapter as proof of concept of the proposed KREMS method. The development of this completely new method is the first approach made so far to identify OIMF in geomagnetic satellite observations. The validation and analysis in the context of the presented OSSE have already been published in Hornschild et al. (2022). The following chapter will strongly refer to this publication and recapitulate and expand on its findings.

The central goal is to obtain a posterior separation of the individual magnetic field contributions through the assimilation of satellite magnetometer data by using an adequate prior spatio-temporal characterization. In the OSSE, synthetic artificial measurements instead of real satellite magnetometer data are used for assimilation. In this way, the

crucial advantage of the OSSE is the knowledge of actual individual magnetic parts contained in the artificial data. This fact allows a precise evaluation of the separation and potential identification of the OIMF by circulation. Finally, the assimilation of the artificial observations is performed using the Kalman filter algorithm and Bayesian inversion of the Kalmag model, described in Section 2.2.2.

After introducing the framework, the OSSE is used in an ideal scenario (Section 4.2) to demonstrate the general capability of KREMS and the main dependencies of the results. Subsequently, Section 4.3 presents a further development of the method using additional spatial constraints, while afterward, the OSSE is considered in different non-ideal scenarios (Section 4.4) to prove the method's optimality and robustness. The chapter is finally closed with a further discussion of the limitations of KREMS and a comparison to the existing approach for tidal-induced EM signals (Section 4.5).

4.1.2 Creating artificial Swarm-like observations

In order to create artificial Swarm-like observations, the orbiting positions of the satellites Alpha and Bravo from the Swarm constellation between 2014 and 2021 are extracted. The satellites fly at two different low orbits, Alpha at an initial altitude of 460 km with an inclination of 87.4° and Bravo at a slightly higher initial altitude of 530 km with an inclination of 88°. The third satellite of the Swarm mission, Charlie, was not taken into account due to problems with its backup magnetometer. Additionally, the following selection was applied to this track set to obtain a similar data distribution as the one used to derive the Kalmag model. The satellite positions were picked at a sampling interval of 10 s and further selected to satisfy relatively geomagnetic quiet conditions. Therefore, at low magnetic latitudes (below 60°), only nighttime locations were considered, and in addition, a low level of geomagnetic activity is required. For this purpose, the planetary K_p index of geomagnetic activity (Matzka et al., 2021) is chosen, and only satellite positions at times with $K_p \leq 2$ are taken into account.

In a further step of producing artificial observations, realistic measurements have to be generated. Therefore, seven magnetic contributions, one associated with ocean circulation and six others, which are components of the Kalmag model, were simulated: a core field, a lithospheric field, an ionospheric field, and three magnetospheric fields (close, remote and fluctuating). Table 4.1 shows the maximum spatial resolution in spherical harmonics for each of these components used in the presented OSSE to create the artificial observations. The prior characterization of these non-oceanic contributions is realized using the autoregressive processes (ARPs) mentioned before in Section 2.2.3 and described in detail in Baerenzung et al. (2020, 2022). Using these established ARPs of the Kalmag model, it is possible to generate some random time series for each non-oceanic magnetic

Table 4.1: Non-oceanic magnetic sources considered in the OSSE

Internal sources	**SH degree**	**External sources**	**SH degree**
Core	20	Close magnetosphere	15
Lithosphere	75	Remote magnetosphere	1
Residual/Ionosphere	5	Fluctuating magnetosphere	1

source. The initial state of these time series was randomly drawn from the ensemble of the Kalmag model in 2014.0 and then propagated with a time step of 30 minutes accordingly to the associated ARPs until 2021.0. Finally, at each time step, these sources are evaluated as vector field components at the current satellites' locations. Since a characterization through autoregressive processes is insufficient for magnetic signals induced by ocean circulation, the oceanic contribution has to be taken into account differently. To incorporate the oceanic part into the artificial measurements, the OIMF is directly derived from ECCO2 ocean model data (introduced in Section 3.1) using the electromagnetic induction solver X3DG, as described in Section 2.1.2. The resulting 852 snapshots (7 years of 3-daily values) of the OIMF were first converted in spherical harmonic functions (SH) up to a degree of 30 using SHtools (Wieczorek and Meschede, 2018), interpolated in time and then evaluated at the different satellite positions. The temporal mean ($\overline{\mathbf{B}}_r$) and corresponding standard deviation (STD of $\mathbf{B}_r$) of the time series of OIMF from the ECCO2 model used in this OSSE is displayed in Figure 4.1. In the OSSE, especially the OIMF from the ECCO2 model but also the other randomly generated magnetic field contributions constitute the ground truth that is tried to recover with the assimilation algorithm.

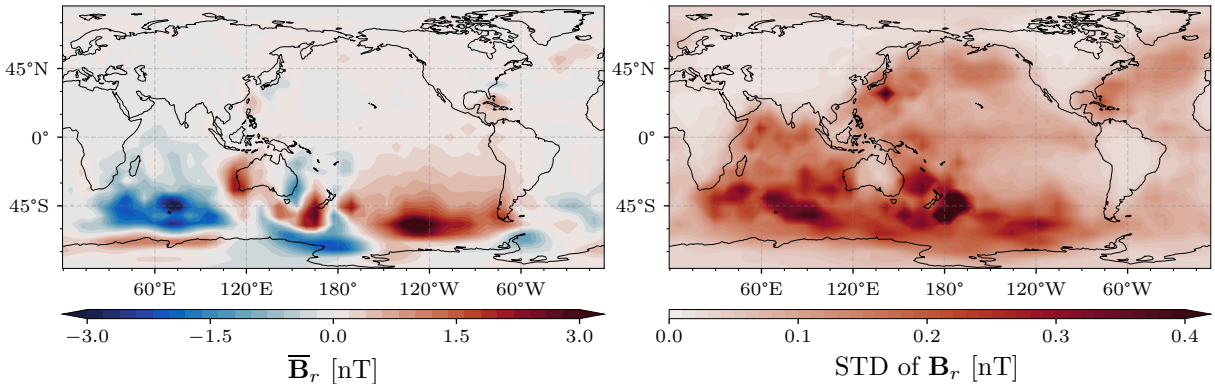

Figure 4.1: Temporal mean (left) and standard deviation (right) of the radial component of the magnetic field from ocean circulation (calculated from ECCO2 data) at sea surface height. The spatial resolution corresponds to a decomposition to spherical harmonic functions up to degree 30.

4.1.3 Kalman-filter based assimilation

Subsequently, after the creation of the artificial observations, their assimilation can be initiated. The assimilation is performed using the Kalman filter algorithm of Kalmag, as described in Section 2.2.2. Accordingly, the prior characterization of the non-oceanic contributions is once more realized using the ARPs, which are thereby parameterized in the same way as for the generation of the artificial observations. The spatial resolution of the non-oceanic contributions corresponds to the SH degree listed in Table 4.1. The prior characterization of the magnetic source accounting for the oceanic contribution is chosen differently. Following the idea outlined in Section 2.2.4, the complete temporal behavior of the oceanic contribution is prescribed by some a priori presumed estimates. Therefore, proxies of the OIMF are calculated in parallel to the Kalman filter algorithm, and the assimilation is used to rescale these presumed estimates, i.e., to determine a scale factor. This scale factor is assumed to be constant in time but variable in space. The general detectability (whether the oceanic contribution can be extracted from the data or not) at different locations can be assessed by this scale factor. Subsequently, the factor also provides a quality measure of how well the assimilated data reflect the a priori assumed OIMF.

In the OSSE, the presumed OIMF estimates used for KREMS are denoted as imposed oceanic field $\mathbf{B}^{\text{imp}}$, and the magnetic contribution induced by ocean circulation in the artificial observations is denoted as the true oceanic field $\mathbf{B}^{\text{true}}$. Consequently, the scale factor $k(x, y)$ to be determined by the assimilation aims to satisfy the following relation:

$$k(x, y) \cdot \mathbf{B}^{\text{imp}}(t, x, y) \approx \mathbf{B}^{\text{true}}(t, x, y) \, . \tag{4.1}$$

In order to achieve this, first, the radial component of the imposed oceanic magnetic field is projected on a grid of the Earth's surface and point-wise modulated by scale factor from the assimilation k_i on each grid point i, described by:

$$\mathbf{B}_{r,i} = k_i \cdot \mathbf{B}^{\text{imp}}_{r,i} \, , \tag{4.2}$$

whereby $\mathbf{B}_{r,i}$ denotes the radial magnetic field on the corresponding grid point i. Using a Gauss Legendre grid (containing $N = (\ell_{max}+1)\cdot(2\ell_{max}+1)$ points) allows the conversion of the radial magnetic field into a potential ϕ in the spherical harmonics domain through the following relation:

$$\phi_{\ell,m} = \sum_{i=1}^{N} \mathbf{B}_{r,i} \, \omega_i \, P_{\ell,m,i} \, , \tag{4.3}$$

where i indicates the i^{th} Gauss node of the grid, $P_{\ell,m,i}$ the associated Legendre polynomials of degree ℓ and order m, ω_i the Gaussian quadrature weights, and $\phi_{\ell,m}$ describes the

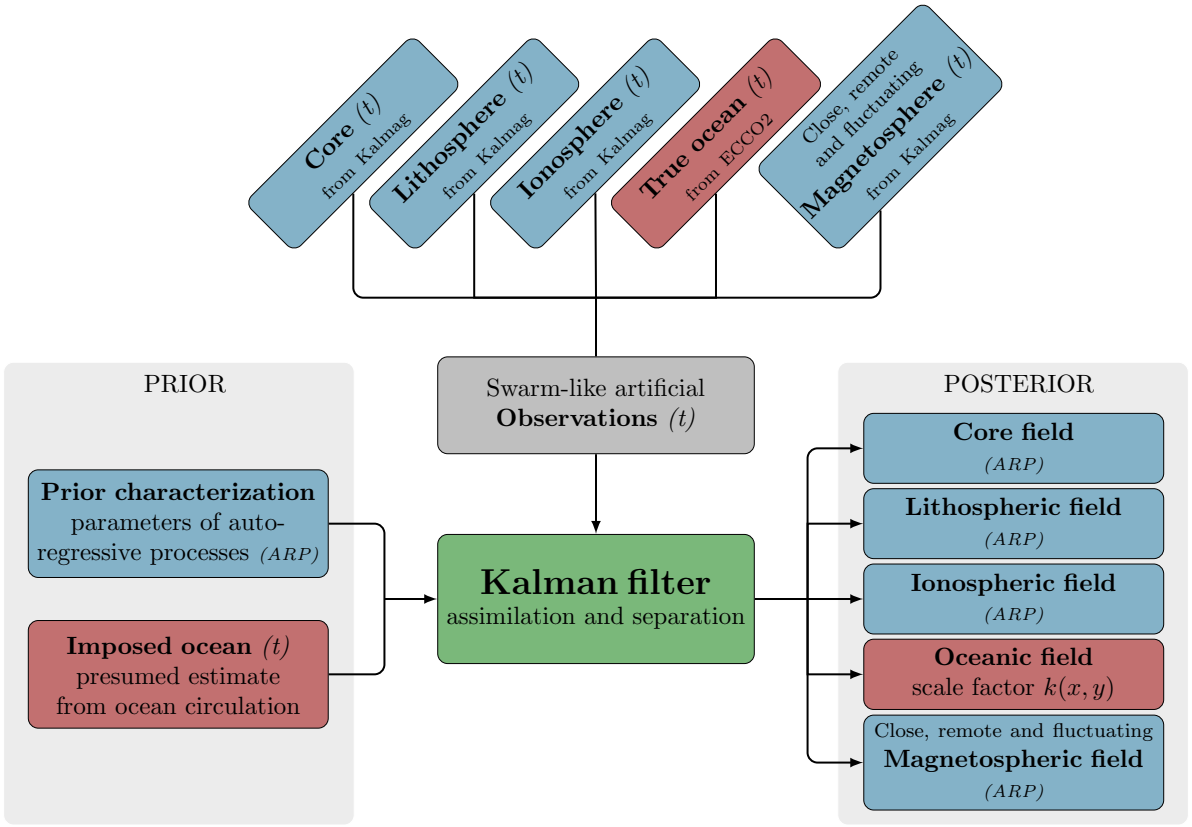

Figure 4.2: Sketch of the OSSE illustrating the input of the assimilation and the separation of the different magnetic field contributions. The magnetic component from ocean circulation is highlighted in red. The other contributions modeled by autoregressive processes (ARP) are marked in blue.

potential expanded up to SH of degree $\ell = \ell_{max}$. The potential $\phi_{\ell,m}$ allows evaluating the predicted oceanic induced field everywhere above the Earth's surface, particularly at the different satellite positions, which is required to perform the analysis of the Kalman filter algorithm. Through the assimilation, the predicted radial oceanic magnetic field can be corrected by updating the scale factor. The OSSE is initialized with an ensemble of scale factors, and through the assimilation, the convergence of the ensemble mean value k and the associated standard deviation is observed. In the beginning, the scale factors are typically drawn on each grid point from a normal distribution $\mathcal{N}(0, 1)$ with zero mean and standard deviation of one. The structure of the OSSE is summarized in a scheme displayed in Figure 4.2.

4.2 Results in an ideal scenario

4.2.1 Scale factor determination

First of all, an ideal scenario of the OSSE is considered. In this case, the imposed oceanic magnetic field (the presumed OIMF estimate) is chosen to be identical to the true oceanic contribution in the artificial observations. Consequently, the scale factor should be precisely one at each time step and each location (see equation 4.1). Although imposing the exact OIMF from circulation may not be the most realistic scenario, it exhibits the general principle and upper limit of the proposed method. Therefore, this idealistic scenario serves also as a reference. In the following, the main results of this scenario are used to evaluate the scale factor determination.

At the beginning of the assimilation in 2014.0, at each node of the Gauss Legendre grid, an ensemble of scale factors is distributed following the Gaussian normal distribution $\mathcal{N}(0,1)$. Under the influence of 7 years of Swarm-like artificial observations, the Kalman filter updates the scale factors making them converge to the actual values. Therefore, for the analysis, the final ensemble of scale factors of the year 2021.0 is considered. The final results of the assimilation are then expressed in two quantities: the final posterior ensemble mean and its corresponding final posterior standard deviation of the scale factors at each node of the Gauss Legendre grid. The final mean (k_f) is used as a measure of OIMF detectability, and its standard deviation (STD of k_f) is viewed as the associated uncertainty. Eventually, the final determined scale factor can be used to rescale the presumed estimates of the OIMF:

$$\mathbf{B}^{\text{res}}(t,x,y) \;=\; k_f(x,y)\cdot\mathbf{B}^{\text{imp}}(t,x,y)\;. \tag{4.4}$$

The chosen distribution $\mathcal{N}(0,1)$ of the scale factors at the beginning of the assimilation implies that initially, no contribution from the OIMF is assumed. Therefore, the rescaled field $\mathbf{B}^{\text{res}}$ reflects the detected OIMF and emphasizes the part of the signal gained from the true OIMF by assimilating artificial observations (under the given imposed magnetic field). Both quantities mean and STD of k_f are shown in Figure 4.3 (top row). In the ideal scenario of the OSSE, the actual scale factor is known to be one. Therefore, the accuracy of the final scale factor determination can be examined by the absolute deviation ($|k_f - 1|$), and the precision of the scale factor determination can be analyzed through the uncertainty (STD of k_f). For the evaluation of the scale factor determination, this absolute deviation is also depicted in Figure 4.3 (bottom left). It is mentionable again that both the scale factor deviation as well as the standard deviation of the scale factor are initially equal to one.

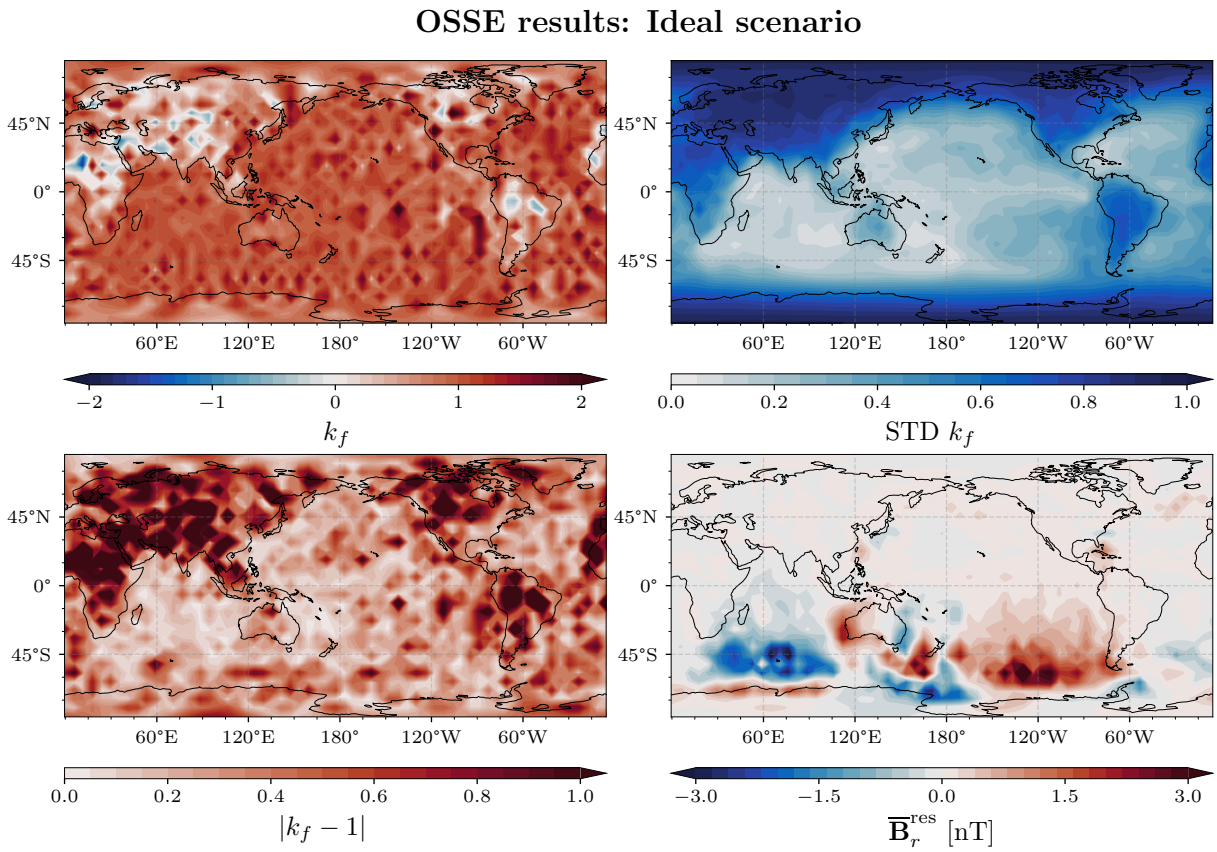

Figure 4.3: The assimilation results for the ideal test case scenario with identical true and imposed magnetic fields. The upper row shows both the final scale factor (k_f) on the left and the associated uncertainty (posterior standard deviation) of the final scale factor (STD of k_f) on the right. The bottom row shows both the absolute deviation of the final scale factor from the true value ($|k_f$ - 1|) on the left and the temporal mean of the rescaled radial magnetic field ($\overline{\mathbf{B}}_r^{\text{res}}$) on the right. Dark red in the bottom left plot (respectively blue in the upper right) indicates unchanged major deviations (respectively large remained uncertainty) after the assimilation, whereas lighter colors point out areas with lower deviations and reduced uncertainty.

The results in Figure 4.3 show clearly that the Kalman filter strongly reduces the deviation of the scale factor (Figure 4.3, bottom left panel) in nearly all oceanic areas. Expectedly, in large parts of the continental regions, where no magnetic signals from the ocean arise, the scale factor's deviations remained close to their initial value. Moreover, the standard deviation of the final factor (Figure 4.3, top right panel), which is considered as associated uncertainty, also exhibits a significant reduction in the oceanic areas. The pattern of this reduced uncertainty correlates well with the high variance of the OIMF (see Figure 4.1, right panel). Areas characterized by high variability of the OIMF evince low uncertainties, whereas areas with a tiny OIMF variability evince high uncertainties. The temporal fluctuations of the imposed magnetic field are decisive to the scale factor

determination. Thus, the mean of the OIMF (Figure 4.1, left panel) does not affect the results (neither the scale factor nor its associated uncertainty). In other words, KREMS is sensitive to the imposed magnetic field anomalies.

It can be noted that the standard deviation of the scale factor strongly increases at higher latitudes (larger than 60°). This latitude dependence corresponds to the chosen nighttime data selection below 60°. Therefore, an increased influence of ionospheric magnetic field contribution and field-aligned currents at higher latitudes can explain this substantially larger uncertainty. The dependence of the scale factor determination on the imposed magnetic field variability and the latitude will be analyzed in more detail later.

Finally, the determined scale factor can be used to rescale the imposed OIMF according to Equation (4.4). The radial component of the temporal mean rescaled field $\overline{\mathbf{B}}_r^{\text{res}}$ is shown in Figure 4.3 (bottom right panel). When rescaling the mean OIMF, it must be noted that the scale factor is determined from the OIMF anomalies because, as stated before, it is not sensitive to the mean magnetic field. Nevertheless, the rescaled field reflects the detectable part of the OIMF and emphasizes the part of the signal gained from the true OIMF by the assimilation. The mean rescaled field (Figure 4.3 bottom right panel) is very similar to the mean of the true OIMF (compare to Figure 4.1). The only slight deviations between the rescaled and true oceanic field demonstrate that KREMS provides a correct rescaling of the imposed oceanic field.

Spatial analysis

An advantage of the approach is locally varying rescaling, which allows for spatial analysis of the scale factor determination. Although the results of the OSSE indicate a reasonable scale factor determination globally over large parts of the oceans, some local differences are noticeable. Large parts of the Indian Ocean and the Western Pacific evince only tiny deviations of the scale factor. However, some local deviations are more increased in parts of the Atlantic, the Eastern Pacific, or the Southern Ocean.

In order to compare the main oceans, the area-weighted spatial average of the final scale factor, its associated uncertainty and its deviation from one is considered in the corresponding areas. Therefore, the basin masks of the World Ocean Atlas 2018 (WOA18) were used to define areas of the main oceans and adapted to the Gauss Legendre grid. These resulting areas for the Atlantic, Pacific, Indian, and Southern Oceans are highlighted in Figure 4.4. Additionally, the ETOPO1 dataset (Amante and Eakins, 2009) was used to define a global oceanic area. Table 4.2 lists the area-weighted spatial averages over the main oceans and the overall oceanic spatial average.

The spatial average is close to one in all cases; in particular, one is always within the average uncertainty. The closeness of the final scale factor to the true value is also high-

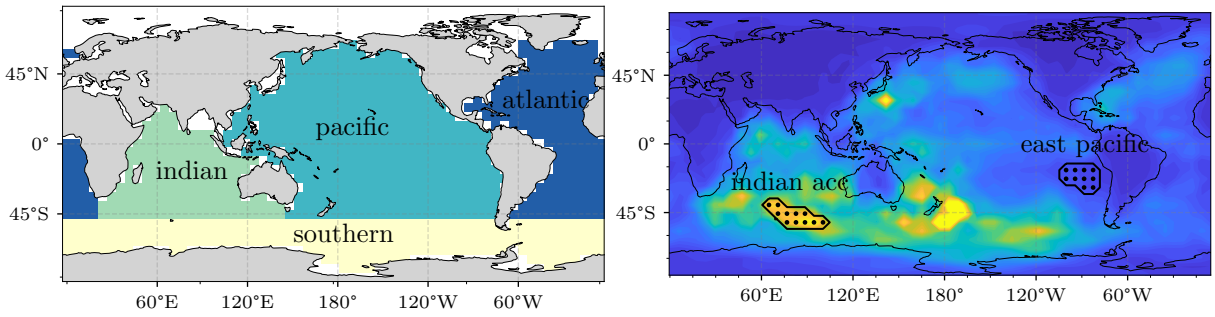

Figure 4.4: On the left side, a world map with highlighted areas for the main oceans: Atlantic, Pacific, Indian and Southern Ocean. The marked areas are used for area-weighted spatial averages and correspond to the used spatial resolution of SH degree 30. On the right side, two specific areas are marked, which comprise a small selection of grid points corresponding to SH of degree 30. Several connected grid points with higher OIMF variability define the Indian ACC area; conversely, grid points with lower OIMF variability define the East Pacific area. In the background, the standard deviation of the radial OIMF from the ECCO2 model underlines the OIMF variability.

Table 4.2: Area-weighted spatial averages of the final scale factor, its associated uncertainty and its deviation

Area	**scale factor** k_f	**uncertainty (STD of** k_f**)**	**deviation** $\lvert k_f - 1 \rvert$
Atlantic	0.93	0.33	0.33
Pacific	0.95	0.24	0.26
Indian Ocean	0.99	0.14	0.15
Southern Ocean	0.96	0.43	0.28
Full oceanic area	0.93	0.30	0.27

lighted by the average deviations, which correspond well to the uncertainties. The Indian Ocean provides the best average scale factor and lowest uncertainty results. Likewise, the scale factor determination results in the Pacific are slightly better than in the Atlantic. These results indicate that regions with minor deviations of the scale factor from the actual value coincide with a low standard deviation of the scale factor. Conversely, more significant deviations occur in areas with higher standard deviations. Interestingly, the Southern Ocean shows a comparable small average deviation of the scale factor despite its relatively high average uncertainty. This discrepancy again indicates that the uncertainty covers the influence of other magnetic sources in this area. Generally, the results demonstrate a reasonable scale factor determination on global and finer spatial scales, and the posterior standard deviation of the scale factor proves to be a valuable measure to assess the quality of the assimilated scale factor.

4.2.2 Evolution and convergence of the scale factor

Further insight can be gained by looking at the development of the scale factor in the Kalman filter over assimilation time. The changes from the initial value of the scale factor under the influence of new observations and its convergence towards the true value are investigated.

First, the scale factor evolution in two different areas is considered in more detail: One area with high and another with relatively low variability of OIMF. According to the previous results, this corresponds to a relatively low, respectively high uncertainty of the scale factor. The high-variability area (low scale factor uncertainty) is located in the Southern Indian Ocean between Africa and Australia, around 45° South (named Indian ACC area), and the low-variability area (high scale factor uncertainty) is located in the Eastern Pacific close to the coast of central South America, around 15° South (named East Pacific area). The comprised grid points and areas are marked in Figure 4.4 (right side).

The OIMF at the Indian ACC area evinces a spatial area-weighted mean of the OIMF's standard deviation of around 0.35 nT. Contrary, in the East Pacific, it is an order of magnitude lower around 0.05 nT. Correspondingly, the spatial area-weighted average of the scale factor uncertainty also differs in both areas (0.13 at the Indian ACC area, 0.44 in the East Pacific area). Consequently, a different evolution of the scale factor is also expected in both areas. The pointwise local results from several connected grid points and their spatial area-weighted mean in these specifically chosen areas are presented together in Figure 4.5.

As can be seen from this figure, the factor evolves remarkably fast towards the true value of 1.0. The spatial mean in the high-variability area (Indian ACC, Figure 4.5 left panel) converges already close to one after less than one year of assimilated data. It is clearly visible that the convergence in the case of the low-variability (East Pacific, Figure 4.5 right panel) area takes a longer time. However, the spatial mean in this area also approaches the correct value after approximately two years of assimilated data. This relatively short time suggests sufficient assimilated observations to obtain a reasonable scale factor. In comparison, the spread of the local scale factor results is significantly narrower for the high-variability area, which corresponds well to the lower standard deviation of the scale factor. Some individual local results with low OIMF variability show large deviations from the true value, indicating that a proper scale factor determination at these locations is impossible. Promisingly, the fast convergence of the scaling factors, especially of the spatial area-weighted mean, emphasizes the sensitivity of KREMS to magnetic signals from OIMF.

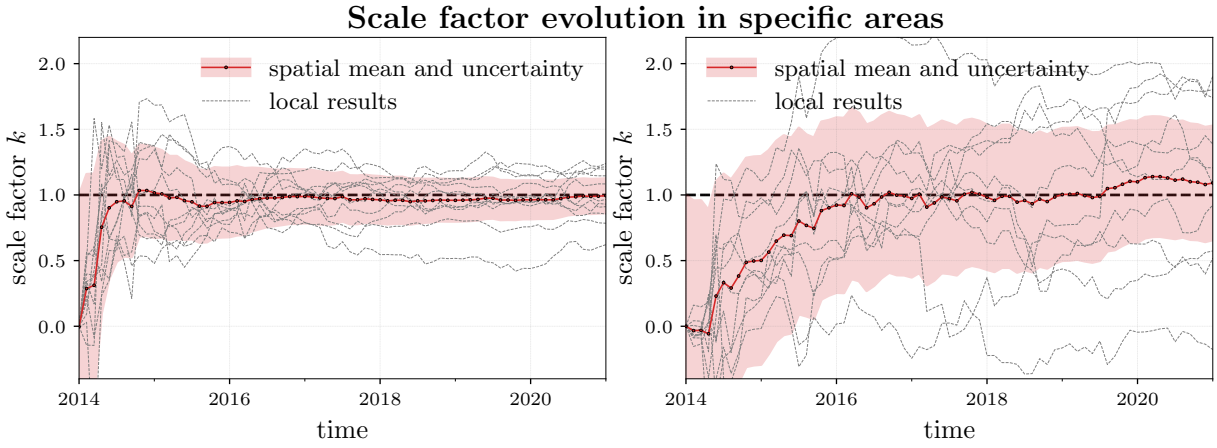

Figure 4.5: The evolution of the scale factor over the entire assimilation period is considered in two different areas: An area of high OIMF variability located in the Southern Indian Ocean (Indian ACC) on the left side and an area of low OIMF variability located in the Eastern Pacific (East Pacific) on the right. The grey lines denote the pointwise local factors, and the red lines highlight the spatial area-weighted averaged mean and uncertainty (posterior standard deviation). The horizontal, dashed, black line indicates the true scale factor.

Scale factor convergence

The final convergence can be examined separately by inspecting two assimilations with different start values of the scale factor. Besides the already studied assimilation with initially drawn scale factors from Gaussian distribution $\mathcal{N}(0,1)$, another one with an identical setup but initial scale factors following an $\mathcal{N}(2,1)$ distribution was performed. Thus, in the ideal scenario, both assimilations start with a scale factor one standard deviation distant from the true value. Theoretically, the scaling factors should still match at the end of the assimilation despite the initial difference. The convergence can then be considered as the difference between the final scale factor from different initial conditions: $|k_f^2 - k_f^0|$.

The difference is shown in Figure 4.6. In large parts of the ocean, the convergence is close to zero, which implies a conclusive result from the assimilation in most areas. As expected, the pattern corresponds to the scale factor uncertainty, and higher convergence differences occur only in areas of higher uncertainty. Convincingly, at all grid points over the ocean, the convergence difference is below the uncertainty of the scale factor. Actually, in some areas, e.g., at higher latitudes in the Southern Ocean, the convergence difference is tiny, but the scale factor uncertainty (see Figure 4.3 top right panel) is significantly larger. It can be concluded from this that the convergence indicates a consistent scale factor determination. However, additional aspects (like other magnetic sources or nighttime data selection) influence the scale factors' uncertainty. Furthermore, an advantage of

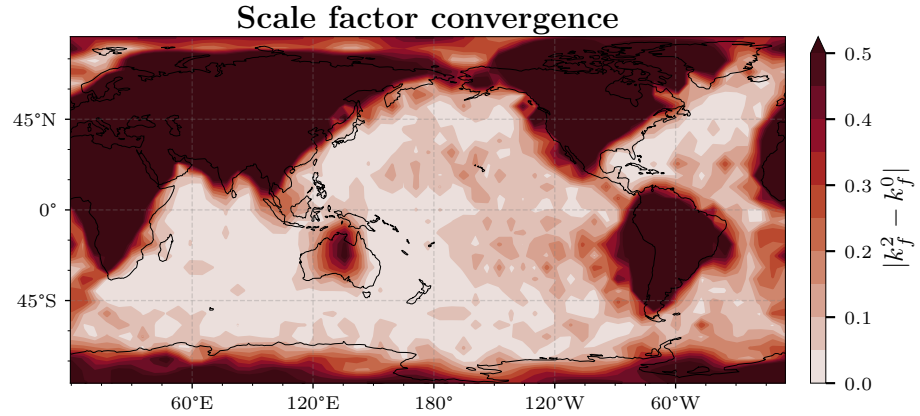

Figure 4.6: The convergence of the scale factor is illustrated by the absolute difference between the final scale factors from two differently initiated assimilations. One scale factor (k_f^2) stems from assimilation with a scale factor start value of two. The other scale factor (k_f^0) stems from assimilation initiated with a zero scale factor. Light colors indicate a satisfactory consistency in the final scale factor results despite different initial conditions. Dark colors indicate a poor convergence and reveal that the assimilation results are inconclusive.

the convergence is that it can be computed without knowing the true scale factor, thus allowing to test the conclusiveness of the scale factor determination outside the OSSE.

4.2.3 Scale factor dependence on imposed variability and geographical latitude

The results of the OSSE in an ideal scenario indicate two major dependencies of the scale factor determination. First, the uncertainty of the scale factor determination depends on the temporal variability of the imposed magnetic signal. Furthermore, there is also a dependence on the geographical latitude of the scale factor's location. Both dependencies will be investigated in more detail in the following section.

For this purpose, the standard deviation of the final scale factor (STD k_f) is plotted over the standard deviation of the imposed radial magnetic field (STD $\mathbf{B}_r^{\text{imp}}$) for each grid point. Additionally, the absolute latitude position $|\varphi|$ of each grid point is marked in color. This illustration can be viewed in Figure 4.7. The presentation undoubtedly confirms the hypothesis that the scale factor's uncertainty strongly depends on the temporal variability of the imposed magnetic field and latitude position. The higher the imposed variability is at a given grid point, the more the uncertainty of the scale factor can be reduced from the initial value of one by the assimilation. However, this effect is much more increased at lower latitudes than at high latitudes (can be seen in Figure 4.7, where only dark colors show a strong uncertainty reduction). Remarkably, the minimal uncertainty for a

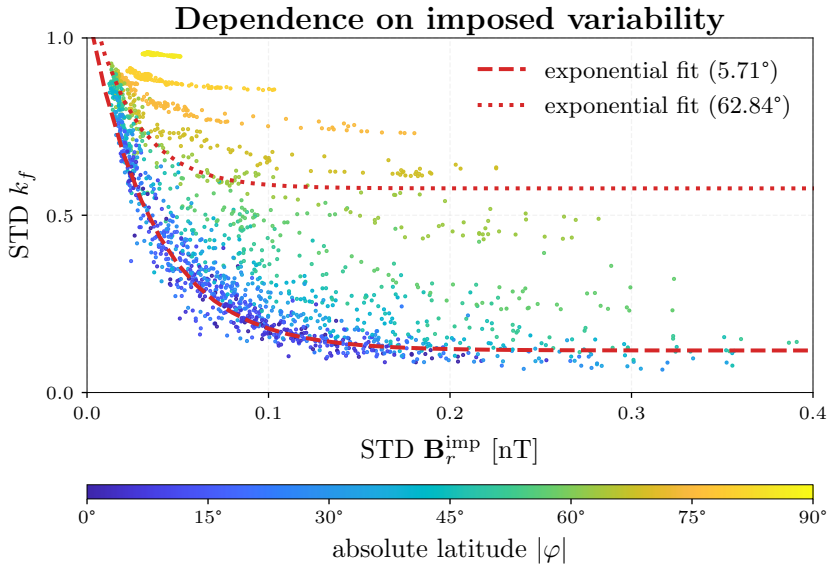

Figure 4.7: The final scale factor uncertainty (STD k_f) over imposed variability (STD of $\mathbf{B}_r^{\mathrm{imp}}$) for each scale factor on the Gauss -Legendre grid corresponding to SH of degree 30. The absolute latitude of each grid point is marked in color. The blueish color highlights low latitudes, whereas the yellowish color highlights high latitudes. Exemplarily, for two different latitudes, the result of an exponential fit is shown to analyze the imposed variability dependence.

fixed latitude is limited and cannot be substantially reduced further by higher imposed variability.

The uncertainty reduction exhibits a clear exponential dependence on the variability. This dependency can be validated by fitting a 3-parametric exponential function to all grid points of a given latitude of the form: $f(x) = a \cdot \exp(b \cdot x) + c$. The fit results for two exemplary different latitudes are additionally shown in Figure 4.7. Generally, the exponential fit describes the dependence adequately. On the one hand, the most significant difference is revealed by the fit parameter c, which can be interpreted as the minimal achievable uncertainty. Close to the equator (latitude of 5.71°), the minimal uncertainty of the scale factor is around 0.12 compared to the higher latitude (62.84°), where only 0.58 can be achieved. On the other hand, high values of the fit parameter b but similar for different latitudes indicate the minimal uncertainty is already reached for relatively small imposed variability in this OSSE.

4.2.4 Spatial and temporal scales

Finally, the ideal scenario of the OSSE was used to explore the sensitivity of KREMS to different spatial and temporal scales of the ocean-induced magnetic field. Therefore, the spatial and temporal resolution of the OIMF is varied. Three different temporal

resolutions of the OIMF of *3-daily*, *weekly*, and *monthly* means are considered. In addition, also three different spatial resolutions corresponding to SH of degree and order of 15, 30, and 45 are tested. In all cases, the true OIMF included in the artificial data and the imposed OIMF are still chosen identically to keep the ideal scenario. A separate assimilation was performed for each combination of these different spatial and temporal scales of the OIMF. Afterward, the results are compared in terms of the global area-weighted averaged scale factor deviation and the associated scale factor uncertainty.

An overview of these results is illustrated in Figure 4.8, where the final values are given for each test case. From this figure, two clear tendencies can be identified: First, a higher temporal resolution of the OIMF leads to an improved scale factor determination (lower scale factor deviation and uncertainty). Since the higher temporal resolution is accompanied by higher variability, the imposed signal is easier to identify in this case. Secondly, a higher spatial resolution of the OIMF deteriorates the scale factor determination (larger scale factor deviation and uncertainty). Interestingly, although a higher spatial resolution also provokes a higher variability, the scale factor determination is diminished in this case.

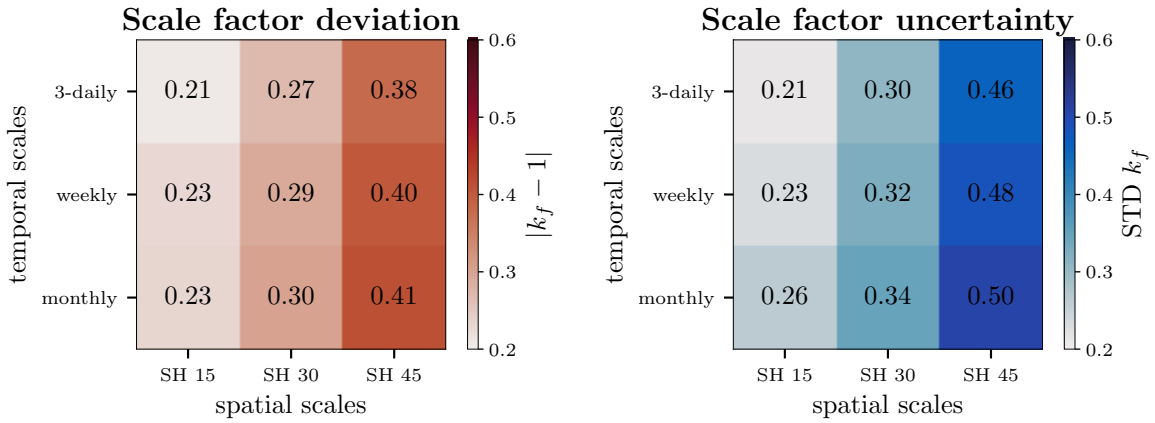

Figure 4.8: Globally averaged scale factor determination results for different spatial and temporal scales of the OIMF in the ideal scenario of the OSSE. The area-weighted spatial averages are shown for the final scale factor determination (left side) and its associated uncertainty (right side). The temporal scales are varied from monthly to 3-daily temporal resolution, and the spatial scales from SH degree of 15 up to 45.

The influence on the scale factor determination by different spatial resolutions is larger than by different temporal resolutions. The better scale factor determination for lower spatial scales indicates a higher sensitivity of KREMS to lower SH degrees. However, it should be noted that the OIMF identification using KREMS is also based on strong temporal constraints via the imposed OIMF and only weaker spatial constraints.

In order to examine this more closely, the energy spectra of the true and the final rescaled OIMF are considered and shown in Figure 4.9. From the comparison of the

energy spectrum, one can see that the rescaled OIMF matches the true OIMF very well for lower SH up to degree 15. For higher SH degrees, minor deviations can be recognized, and the uncertainty increases. On the one hand, this is to be expected since the energy per SH degree is significantly lower for higher SH degrees. On the other hand, this is consistent with the better scale factor determination for lower spatial scales and the noisy pattern seen in the scale factor determination (see Figure 4.3). As a conclusion from the analysis of spatial and temporal scales of the OIMF, it can be noted that the temporal resolution of the imposed OIMF has a minor influence on the scale factor determination and that the proposed KREMS yields better results for lower SH degrees.

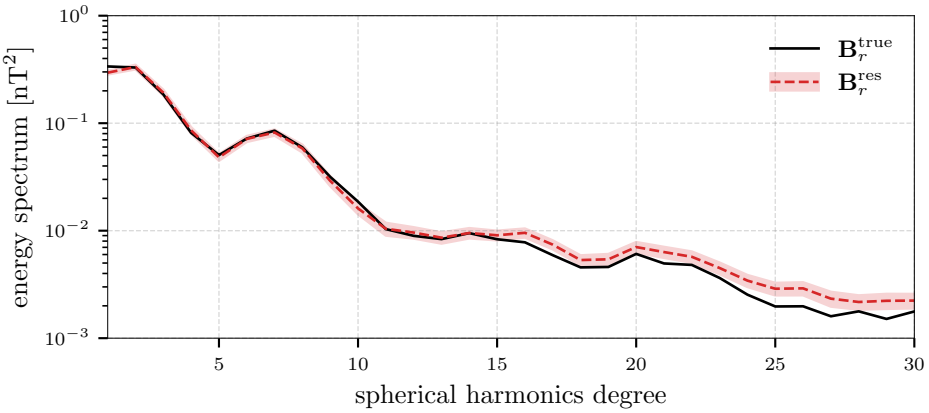

Figure 4.9: The energy spectrum of the true and the rescaled OIMF in the ideal scenario. The mean true OIMF energy spectrum is drawn in black; the mean rescaled OIMF and its associated uncertainty are shown in red.

4.3 Improvements by spatial constraints

4.3.1 Motivation

In the previously presented results, the temporal behavior of the presumed OIMF estimate was the only constraint at each grid point. So far, the scale factors at each grid were uncorrelated and could evolve independently during assimilation. However, it is reasonable to assume that nearby factors are related and not independent of one another. First, the possible relation of the rescaling to oceanic quantities suggests a spatial correlation among the local scale factors. Typically, oceanic quantities (like temperature, salinity, and transport) are also correlated over some spatial extent. Large-scale correlations of such oceanic quantities like oceanic heat (Mazloff et al., 2018) or salinity (Bao et al., 2020) are already found and analyzed in a different context. Second, the spatial expansion of the magnetic field itself causes neighboring grid points to be affected by each other, which justifies a spatial correlation among nearby scale factors. Moreover, the final scale factor of the ideal scenario analyzed before exhibits a partially unrealistic noisy spatial pattern, indicating a potential for improvement by incorporating spatial constraints. The Kalman filter algorithm allows us to incorporate such spatial information via the parametrization of the prior covariance. That can be achieved by adding a spatial correlation for the scale factors at the beginning of the assimilation. Such a potential approach to incorporate spatial constraints by a simplified prior covariance structure is introduced and described in the following subsection.

4.3.2 Exponentially decaying covariance matrix

The goal is to specify a spatial constraint of the scale factors by a simplified covariance structure, where no specific patterns but distance-dependent correlations are imposed. Thereby, nearby scale factors are assumed to correlate more than distant ones. One possible parametrization of the covariance, which takes this into account, is based on an exponentially decaying correlation of the scale factors. In doing so, the prior spatial covariance is initialized by the following parametrization:

$$\mathbf{C}_{ij} = \exp\left(-\frac{d_{ij}}{l}\right), \tag{4.5}$$

where, i and j indicate the Gauss node of the grid, and d_{ij} denotes the distance between two grid points. The covariance $\mathbf{C}_{ij}$ between two scale factors is supposed to exponentially decay with distance compared to a characteristic correlation length scale l. The correlation length then determines the strength of the spatial constraint. Exponential or gaussian

covariance structures using a correlation length a few times larger than the grid size are already established in the context of Kalman filters (Brankart et al., 2010; Park et al., 2022). In order to estimate a reasonable characteristic correlation length for the scale factors, both the spatial correlation of related oceanic quantities and the spatial expansion of the magnetic field are considered in more detail.

First, the correlation length of the zonal depth-integrated velocity and the depth-weighted averaged conductivity is analyzed. For both quantities, the correlation averaged over 100 km between each grid point on the Gauss-Legendre grid corresponding to SH of degree 30 is plotted against the distance in Figure 4.10. Subsequently, an exponential function is fitted using the form: $f(x) = a \cdot \exp(-\frac{x}{l}) + b$, where a and b are fit parameters and l corresponds to the correlation length. For one thing, the results of this exponential fit justify the assumption of an exponentially decaying correlation in both cases. Additionally, they provide a first estimation for the correlation length of the scale factors ($l = 357$ km for zonal depth-integrated velocity and $l = 1108$ km for depth-weighted averaged conductivity). Taking into account the larger influence of oceanic velocities on the OIMF (see Section 3.2.1), the correlation length of the zonal depth-integrated velocity should be considered more dominant for the scale factors.

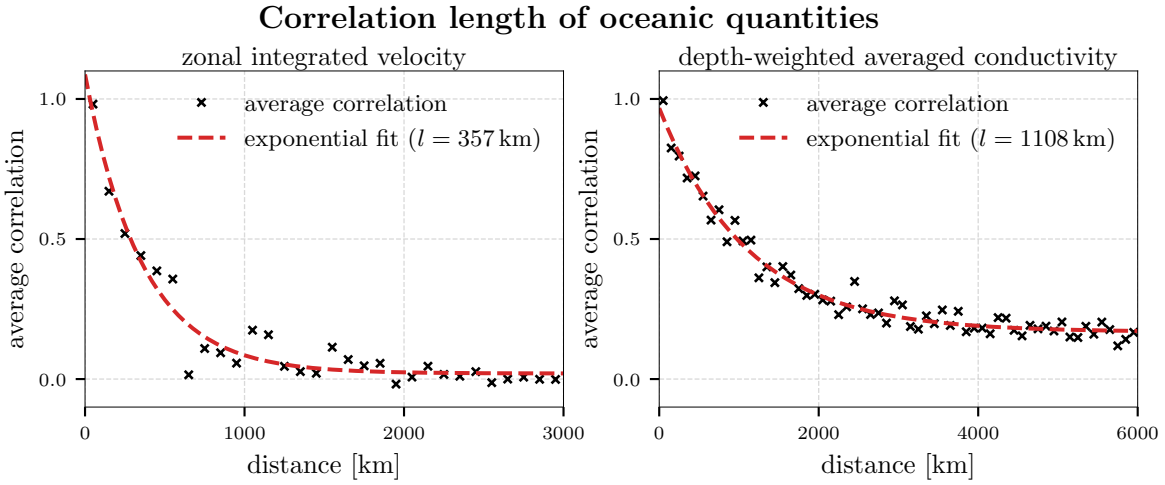

Figure 4.10: Analysis of the correlation length on OIMF-related oceanic quantities. The correlation averaged over 100 km between each grid point of the Gauss-Legndre grid corresponding to SH of degree 30 is plotted against the distance. The distant-dependent correlation of the zonal depth-integrated ocean velocity is shown on the left side and the depth-averaged ocean conductivity on the right. For both, the exponentially decaying correlation is highlighted through an exponential fit (red dashed line), determining a characteristic correlation length.

Secondly, the spatial expansion of the OIMF is approximately estimated using the law of Biot-Savart. Under simplified conditions, a rough formula can be analytically derived to estimate the distance dependence of the magnetic field magnitude. The derivation of

the formula is given in the Appendix A.2.

Based on this consideration, an exponentially decaying covariance structure is employed using a correlation length of $l = 500\,\text{km}$. Additionally, also correlation lengths of $l = 1000\,\text{km}$ and $l = 2000\,\text{km}$ are tested to investigate the effect of stronger spatial constraints. Also, other data assimilation experiments using OIMF showed the best results with a higher observation radius (Irrgang et al., 2017). However, one has to be careful not to over-restrict the scale factors by too strong correlations. Since there is no source of OIMF over land, the prior spatial correlation between scale factors is only applied between different grid points over the oceans ($\mathbf{C}_{ij}$ is set to zero for $i \neq j$ if i or j indicate a Gauss node located on land). The ETOPO1 dataset (Amante and Eakins, 2009) was used again to distinguish ocean and land grid points. The resulting exponentially decaying covariance matrix is then included at the beginning of the assimilation. The structure of such an exponentially decaying covariance matrix can be seen in the Appendix A.8. In addition, this appendix section also compares the covariance matrix with the covariance resulting from the OIMF estimates based on the ECCO2 model. Finally, the incorporated spatial covariance matrix is tested within the OSSE, and the corresponding results are presented in the next section.

4.3.3 Results using spatial constraints

An assimilation using a prior spatial covariance with an exponentially decaying correlation structure and a characteristic correlation length of 500 km as described in the previous subsection was performed are presented in Figure 4.11.

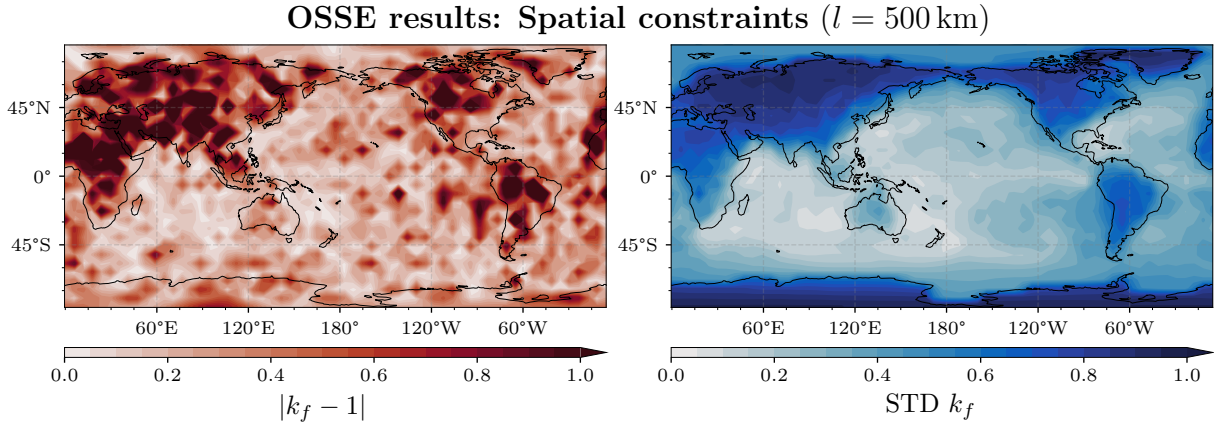

Figure 4.11: The assimilation results of an OSSE using an ideal scenario and incorporated spatial constraints. An exponentially decaying covariance matrix with a correlation length of $l = 500\,\text{km}$ is used. The left side shows the final scale factor deviation, and the right side shows the corresponding uncertainty of the scale factor.

Table 4.3: Area-weighted spatial averages of the final scale factor, its associated uncertainty and its deviation

Area	**scale factor** k_f	**uncertainty (STD of** k_f**)**	**deviation** $\lvert k_f - 1 \rvert$
Atlantic	0.98	0.31	0.30
Pacific	0.98	0.23	0.24
Indian Ocean	1.00	0.14	0.14
Southern Ocean	0.98	0.31	0.21
Full oceanic area	0.97	0.27	0.24

In comparison to Figure 4.3, there is an overall improvement in the scale factor determination by incorporating the exponentially decaying correlation structure. The scale factor deviation from the true value, as well as the associated uncertainty of the scale factor, are further reduced compared to the previous result. Due to the spatial correlations, the STD of k_f decreased significantly also at latitudes larger than 60°. Furthermore, the improved scale factor determination is also emphasized by the area-weighted spatial averages given in Table 4.3.

Compared to the previous results in Table 4.2, the scale factors are closer to one, and the uncertainty is lower (especially in areas like the Southern ocean). On average, the scale factor is strikingly close to one indicating excellent detectability. The average scale factor deviation is within the uncertainty. Expectantly, the enforced spatial relation between the scale factor at the beginning of the assimilation results in slightly smoother scale factors. However, large parts of the noisy pattern still remain in the final scale factor deviations. The effect of the type of prior spatial covariance also influences the scale factor evolution. On the one hand, the spread of the local pointwise results will be narrower according to the lower uncertainty. On the other hand, the spatial correlation expedites the convergence toward the correct value at the beginning of the assimilation.

Finally, the effect of different higher correlation lengths is considered. Overall, the scale factor determination in this OSSE can be slightly further improved using a higher correlation length. However, it should be noted that in this idealistic OSSE, the true value of all scale factors equals one at each location, which means that they are perfectly correlated. The results of these further assimilations using a higher correlation length are included in the Appendix A.8.

In conclusion, these OSSE results evidently demonstrate that incorporating spatial constraints improves scale factor determination. Already a simplified spatial covariance structure based on distance-dependent exponentially decaying correlations between the scale factors enhances the detectability of the imposed signal. Accordingly, further assimilation results in this thesis are based on a prior covariance with exponentially decaying correlation structure using a correlation length of $l = 500\,\mathrm{km}$.

4.4 Results in non-ideal scenarios

4.4.1 Optimal scale factor

The previous results were obtained in an ideal scenario. However, imposing the exact OIMF from circulation may not be the most realistic scenario. Therefore, more realistic scenarios are considered where the presumed OIMF estimates deviate from the true oceanic contribution in the synthetic observations. The objective of these non-ideal scenarios are to show the robustness and optimality of KREMS in the presence of slight deviations between the imposed and true OIMF. Obviously, in such scenarios, the true value of the scale factor is not precisely one at each location and time step anymore. Hence, a theoretically optimal scale factor is of interest for evaluating the method. In the OSSE, such an optimal scale factor can be calculated and used as a reference due to the known true and imposed magnetic field.

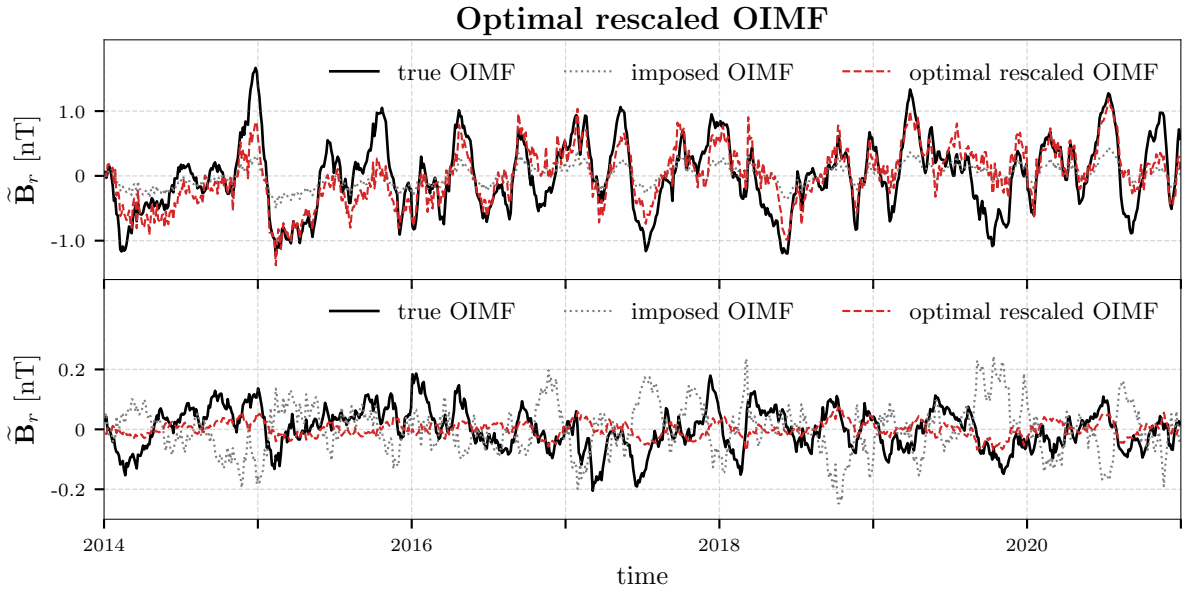

Figure 4.12: Exemplary time series of the OIMF anomalies to illustrate the optimal scale factor. At two arbitrary locations in a non-ideal scenario, the OIMF anomalies of the deviating true (black) and imposed (dotted grey) OIMF are shown. Additionally, the optimal rescaled OIMF anomaly time series is drawn in red. The optimal scale factor k^{opt} is calculated by a least-squares method. In the top example, the imposed signal is scaled up to fit the true signal better ($k^{\text{opt}} = 2.7$). At the bottom example, the imposed signal is scaled down with the opposite sign ($k^{\text{opt}} = -0.3$).

In this thesis, the optimal scale factor $k^{\text{opt}}(x, y)$ is determined by a least-squares fit of the time series between the true and the scaled imposed field at each grid point. Since the presented method is not sensitive to the mean value of the OIMF, the radial magnetic field anomalies ($\widetilde{\mathbf{B}}_r$) are used to calculate this optimal scale factor. The scale factor obtained

by a least-square method is considered the best possible result of the Kalman filter-based assimilation. Figure 4.12 illustrates the optimal scale factor.

In this example, the time series of the differing true and imposed OIMF anomalies are compared to the optimal rescaled ones. In one case (top plot of figure 4.12), the imposed signal is too weak compared to the true OIMF anomaly and is scaled up by an optimal factor ($k^{\text{opt}} = 2.7$). In the other case (bottom plot of figure 4.12), the imposed signal is too strong and even of the opposite sign compared to the true OIMF anomaly, which therefore results in a negative downscaling by the optimal scale factor ($k^{\text{opt}} = -0.3$). In addition, it should be kept in mind that the optimal rescaling depends on the temporal accordance of the imposed and true OIMF anomalies. This example illustrates the rescaling of the imposed OIMF anomaly that is considered achievable in the optimal case. Both examples also highlight the necessity to allow a locally different rescaling with a wide range of scale factors.

Normalized root mean square deviation (NRMSD)

Moreover, an appropriate quality measure of how well the final rescaled magnetic field reflects the true magnetic field is helpful. For this purpose, the normalized root mean square deviation (NRMSD) is considered as a measure of differences between time series of magnetic field anomalies. The NRMSD is calculated with respect to the true magnetic field and defined as follows:

$$\text{NRMSD}(\widetilde{\mathbf{B}}_r) = \sqrt{\frac{\sum_{t_i=0}^{N} \left(\widetilde{\mathbf{B}}_r(t_i,x,y) - \widetilde{\mathbf{B}}_r^{\text{true}}(t_i,x,y)\right)^2}{\sum_{t_i=0}^{N} \widetilde{\mathbf{B}}_r^{\text{true}}(t_i,x,y)^2}}\,, \tag{4.6}$$

where t_i denotes the time steps and $\widetilde{\mathbf{B}}_r^{\text{true}}$ the true radial OIMF anomalies. The normalization accounts for the relation of deviations to the strength of the true signal. In doing so, the NRMSD($\widetilde{\mathbf{B}}_r^{\text{res}}$) describes the differences between rescaled and true OIMF. Accordingly, optimal rescaling minimizes the NRMSD between the true and rescaled OIMF anomalies. The zero magnetic field assumed at the beginning of the assimilation yields NRMSD($\mathbf{0}$) = 1 An optimally rescaled magnetic field after the assimilation would result in NRMSD($\widetilde{\mathbf{B}}_r^{\text{true}}$) = 0. It should be noted that the NRMSD corresponds to the already shown absolute deviations $|k_f - 1|$ in the case of an ideal scenario discussed before (see Appendix A.9).

Furthermore, the NRMSD can be employed to quantify the changes due to the rescaling of the presumed OIMF estimate by assimilation. Thereby, two different aspects can be considered: First, the signal recovery ($\Lambda^{\text{recovery}}$) describes how much the rescaled magnetic field changed from the initially assumed zero magnetic field due to the assimilation. It

can be defined by:

$$\Lambda^{\text{recovery}} \;=\; 1 - \text{NRMSD}(\widetilde{\mathbf{B}}_r^{\text{res}}). \tag{4.7}$$

A positive signal recovery (at most 1 in case of optimal signal recovery) demonstrates a decreased deviation between the rescaled and true magnetic field compared to the beginning of the assimilation.

Second, the signal correction ($\Lambda^{\text{correction}}$) indicates how much the final rescaled magnetic field actually reflects the true signal better than the one originally imposed. It is expressed by:

$$\Lambda^{\text{correction}} \;=\; \text{NRMSD}(\widetilde{\mathbf{B}}_r^{\text{imp}}) - \text{NRMSD}(\widetilde{\mathbf{B}}_r^{\text{res}}). \tag{4.8}$$

Here, a positive signal correction exemplifies that the assimilation successfully improved the imposed magnetic field. Finally, the signal correction can be examined by using the rescaling from assimilation ($\Lambda_{\text{assim}}^{\text{correction}}$) or the introduced optimal rescaling from the least-squares fit ($\Lambda_{\text{opt}}^{\text{correction}}$).

4.4.2 Deviations by spatial resolution

In the first place, deviations between the imposed and true OIMF caused by differently chosen spatial resolutions is considered. Since the magnetic field is not restricted to a fixed point in space, both spatial and temporal differences influence each other, and therefore, spatial and temporal deviations are not strictly distinguishable. Nevertheless, in the following case, the OIMF primarily differs in the spatial domain emphasizing the leading cause of the deviations. In order to ensure comparability, the imposed field was initially kept the same in this scenario as in the assimilations before, and only the true oceanic contribution in the Swarm-like artificial data was replaced. In doing so, the results are not affected by a different imposed OIMF variability.

The effect of spatial deviations is tested by investigating spatial undersampling of the true OIMF. The true OIMF was included in the artificial satellite data with a higher spatial resolution instead of using the same spatial resolution as the imposed OIMF. In this way, a more realistic scenario is mimicked where the presumed proxies of the OIMF are imposed with lower spatial resolution than the true field. Exemplarily, the assimilation results, including the true OIMF in the artificial satellite data up to SH degree 60, are shown and discussed. Spatial constraints were incorporated in the assimilation of this scenario by using the exponentially decaying covariance with a correlation length of 500 km, as discussed in Section 4.3. Figure 4.13 presents the final results of this test case scenario.

Despite the spatial deviations of the imposed magnetic field, the scaling factor is still expected to be close to one on average. The results (top left plot in Figure 4.13)

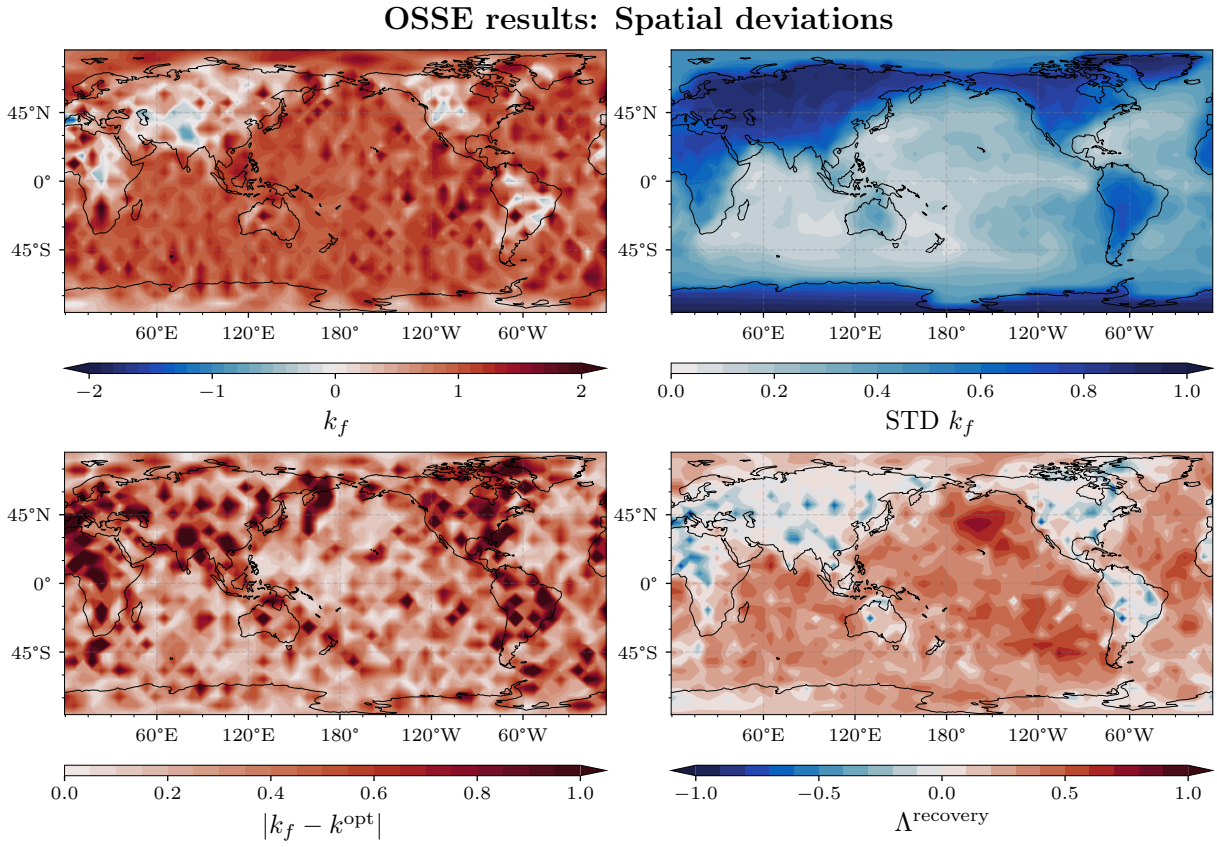

Figure 4.13: The OSSE results for the test case considering deviations by different spatial resolution. The true OIMF is resolved up to SH degree 60; however, the imposed OIMF only up to SH 30. The top row shows the final scale factor k_f (left side) and its associated uncertainty STD of k_f (right side). The bottom left plot shows the deviation of the final scale factor to the optimal scale factor k^{opt} calculated by least-squares. The bottom right plot shows the signal recovery by the assimilation ($\Lambda^{\mathrm{recovery}}$).

confirm that the final scale factor over the oceans is globally close to one. Since the imposed magnetic field and the parametrization of the other magnetic sources remained unchanged, its associated uncertainty (top right plot in Figure 4.13) is identical to the previous results.

The accuracy of the scale factor determination is evaluated by considering the difference to the optimal scale factor. (described in Section 4.4.1). This scale factor deviation $|k_f - k^{\mathrm{opt}}|$ is presented in the Figure 4.13 bottom left panel. Compared to the scale factor deviation of the previous ideal scenario (see Figure 4.3), an apparent similarity is visible. Only in some individual grid points, the deviation is slightly increased. One can draw two conclusions from this: First, KREMS determines a scale factor close to the optimal scale factor resulting from the least-square method without explicitly knowing the true OIMF. Second, minor spatial deviations caused by different spatial resolution only slightly

influence the scale factor determination.

Finally, the signal recovery (explained in Section 4.4.1) is shown in the bottom right plot in figure 4.13. The globally positive signal recovery over the oceans (with an global averag of 0.31) demonstrates the improvement of the final rescaled magnetic field compared to the beginning of the assimilation. This again underlines the ability to identify a given EM signal in artificial observations using KREMS regardless of slight spatial deviations.

However, the signal recovery only reflects the improvement compared to the initially assumed scale factor of zero, which raises the question of whether the method also allows for a correction of the imposed field. Accordingly, the signal correction (as introduced in Section 4.4.1) is examined and shown in Figure 4.14. From this figure, it can be seen

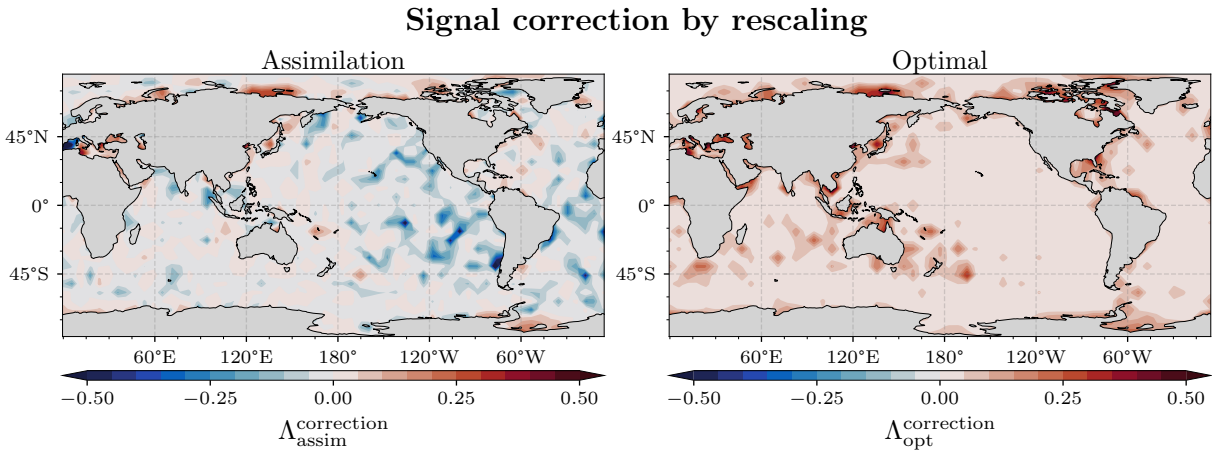

Figure 4.14: Signal correction by rescaling in terms of NRMSD differences. The left plot shows signal correction using the final determined scale factor taken from the assimilation for the rescaling. The right plot shows the optimal signal correction determined using an scale factor resulting from a least-squares fit for rescaling.

that the imposed OIMF cannot be significantly improved by rescaling at most grid points. Especially in areas of low variability of the imposed OIMF and higher uncertainty of the scale factor (e.g., East Pacific), there is even a deterioration of the imposed OIMF. The result is also compared to the optimal achievable signal correction ($\Lambda^{\text{correction}}_{\text{opt}}$) using the optimal scale factor (k^{opt}) for rescaling. The optimal signal correction clearly indicates a limitation of the scale factor approach. Even the optimal scale factor barely allows an improvement in the case of the considered imposed magnetic field in this test case scenario. In most oceanic areas, the optimal signal correction is nearly zero or only very tiny, which means the NRMSD to the true signal is not reducible by a constant factor in this scenario. One can summarize that despite small spatial deviations of the imposed magnetic signal, KREMS, on the one hand, allows the identification of the signal but, on the other hand, is limited in its correction.

4.4.3 Deviations by temporal behaviour

Deviations between the true and the imposed OIMF can not only be caused by different spatial resolutions but also arise when only an incomplete temporal behavior is imposed. Therefore, in this scenario, the full OIMF time series signal is included in the artificial data, but only parts of the signal are imposed. Since a different imposed OIMF is used in this case, the comparability to previous results is hampered. However, this scenario allows evaluating robustness of KREMS to imposing an incomplete temporal behavior.

For this purpose, the OIMF anomalies derived from the ECCO2 model at each grid point are decomposed into several parts according to certain frequency bands. The decomposition of the time-discrete ocean-induced magnetic signal in its frequency components is based on the Fast Fourier Transformation (FFT). Subsequently, several frequencies are combined in four different frequency bands. These four frequency bands correspond to signal periods of: > 365 days, $182 - 365$ days, $30 - 182$ days, and $7 - 30$ days. Note, since the underlying dataset consists of 3-daily time steps, at least a minimum period of 7 days (higher than corresponding Nyquist frequency) is considered. Such a temporal decomposition of the OIMF is exemplarily shown at an arbitrary location in Figure 4.15.

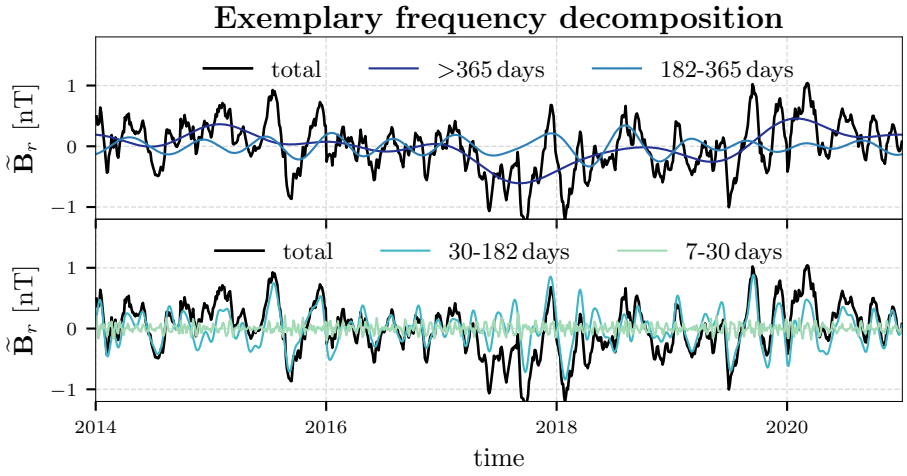

Figure 4.15: The frequency band decomposition of time series of the imposed OIMF anomalies at an exemplary grid position. The black line denotes the complete imposed signal. The decomposed parts of the signal (four frequency bands) are shown additionally in bluish colors. At the top, the two low-frequency bands are shown, and at the bottom high-frequency bands.

This figure presents the total signal and its four temporal components according to the frequency bands (lower frequencies at the top and higher frequencies at the bottom). After that, each of these temporal components was used in a separate assimilation as an imposed signal. In all cases, the true OIMF was represented by the total signal.

Accordingly, in this OSSE scenario, only different components of the true signals are imposed. Since only a part of the signal is used as a presumed estimate, the imposed variability is evidently reduced. Consequently, the scale factor determination becomes more difficult. When evaluating the signal recovery, the reduced imposed variability has to be taken into account.

The results of each assimilation, i.e., for each frequency band, are summarized in Figure 4.16 by showing the area-weighted averages of the final scale factor and its corresponding uncertainty in different oceanic areas (see Figure 4.4). Additionally, the average imposed

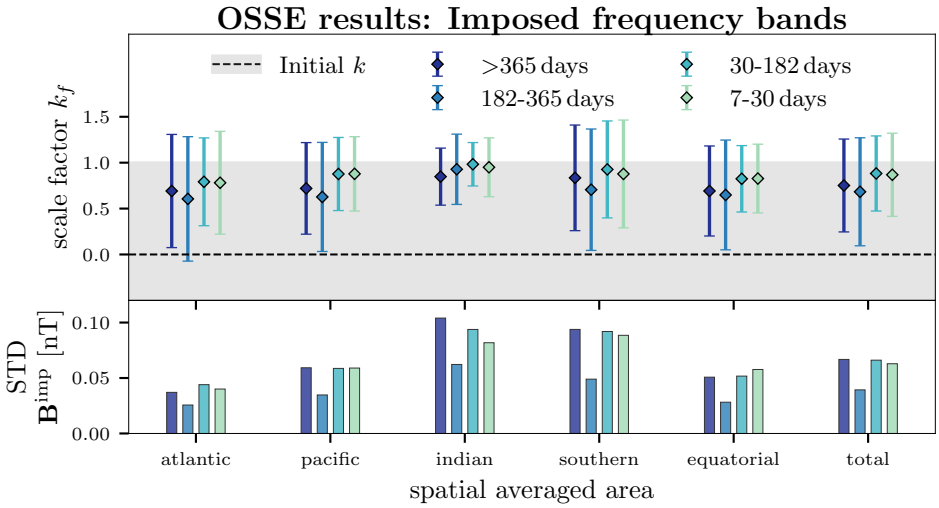

Figure 4.16: The summarized OSSE results for the test case scenario using different frequency bands as imposed OIMF. The area-weighted spatial average of the scale factor and its uncertainty are provided for different areas and each considered frequency band at the top panel. At the bottom, the corresponding imposed variability is shown in comparison for better evaluation.

standard deviation of the imposed signal is shown for better evaluation. Despite the lower imposed variability, the final scale factor distinctly evolved from its initial value of zero to one for all frequency bands in all areas indicating the detectability for all frequency bands. Likewise, the decreased associated uncertainty highlights the robustness of KREMS in recovering the signal when imposing an incomplete temporal behavior. Of course, the scale factor determination depends on the imposed variability again (see Section 4.2.3). Both areas (e.g., the Indian Ocean), as well as frequency bands (e.g., period of 30-182 days) with higher imposed signal, exhibit better scale factor determination (higher scale factor and lower uncertainty). Contrarily, areas (e.g., the Atlantic) and frequency bands (e.g., period of 182-365 days) with lower imposed signal, reveal a poorer scale factor determination (lower scale factor and higher uncertainty). The uncertainty in the Southern Ocean is increased due to higher latitudes despite relatively high imposed variability (e.g., compared to the equatorial region). Besides the already established

and analyzed sensitivities, in the results of Figure 4.16, a slightly better scale factor determination for higher frequency bands is notable. Interestingly, especially also when the imposed variability is comparable (e.g., frequency bands with a period of >365 days and 30-182 days in the Pacific).

In summary, this scenario demonstrates certain robustness of the KREMS to slightly incompletely imposed OIMF temporal behavior. Moreover, the method reveals a sensitivity to a broad frequency spectrum, although higher frequencies seemed a little more favorable.

4.4.4 Deviations by electromagnetic framework

After the consideration of spatial and temporal deviations between the presumed OIMF estimate and the true signal, an explicit test case scenario is presented to examine the influence of differences in the electromagnetic framework used for the OIMF calculations. As already studied and explained in Chapter 3.2, the calculations of the OIMF can be influenced by various quantities and model assumptions (e.g., surrounding conductance model, mantle conductivity, and quasi-stationary approximation).

In this scenario, a rather extreme case is tested, where the simplified Biot-Savart approximation is used to calculate the presumed OIMF estimate, and the true magnetic field (used for the artificial data construction) is calculated using the full electromagnetic solver X3DG. The spatial and temporal resolutions of both true and imposed OIMFs are identical in this scenario. As already described in Section 3.2.4, the insufficient electromagnetic framework based on the law of Biot-Savart (e.g., missing assumption on surrounding conductance model) introduces significant deviations in the radial magnetic field, both on spatial and temporal scales. The OSSE in this scenario investigates how such imperfect assumptions affect the scale factor determination by KREMS. The results are summarized and presented as in the previously studied test case scenarios and displayed in Figure 4.17.

The scale factor (top left plot in Figure 4.17) indicates already larger discrepancies and does not globally tend to a uniform value. Particularly in areas like the Southern Ocean around Australia and parts of the Indian Ocean, where the imposed OIMF variability is high, the scale factor clearly deviates from a value of one, which would imply a correct imposed OIMF. Despite a different imposed magnetic field, the associated uncertainty of the final scale factor (top right plot in Figure 4.17) is exceptionally similar to the previous test cases. The similar variability of the imposed magnetic field explains the striking resemblance. Furthermore, the deviations between the resulting scale factor and the optimal scale factor (bottom left plot in Figure 4.17) obtained from a least-squares fit are considered. A similar pattern as seen before in the scale factor deviation (e.g., compare Figure 4.13) demonstrates once again that KREMS provides a suitable scale

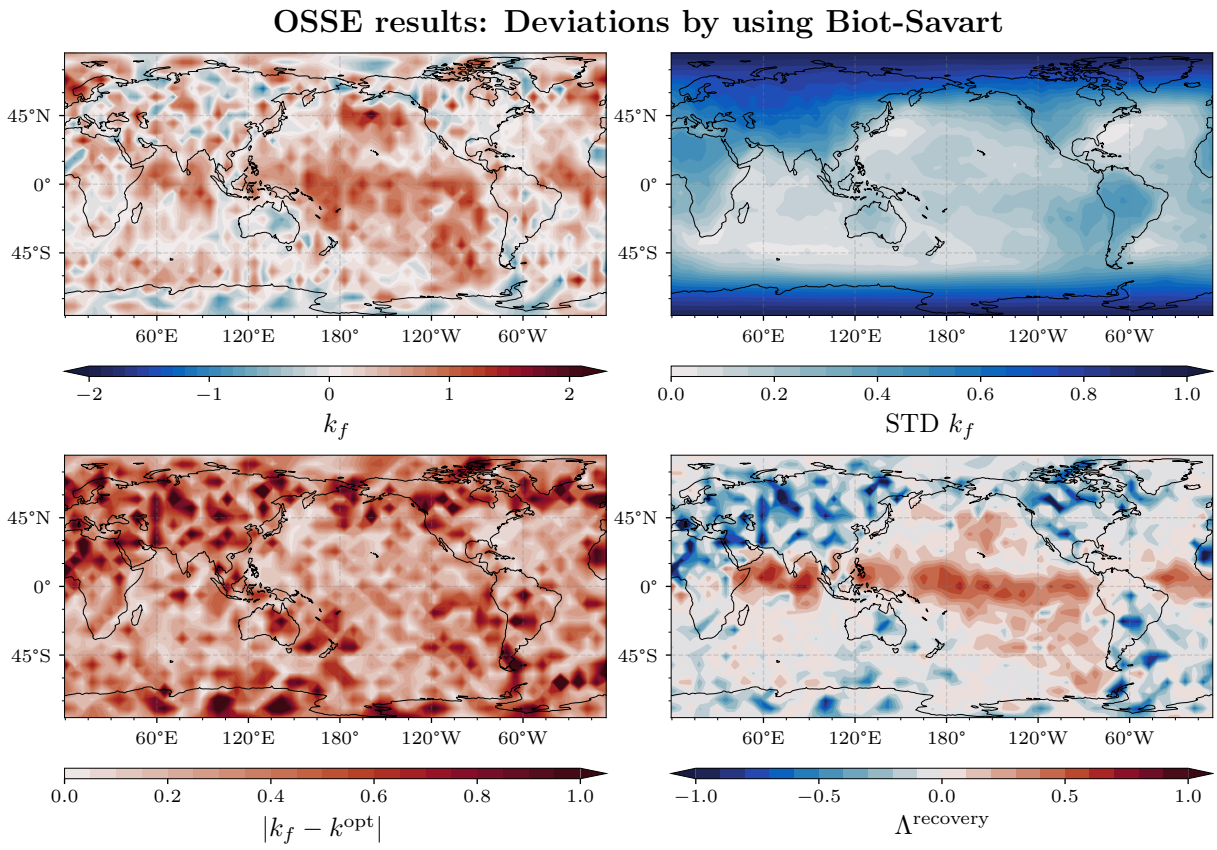

Figure 4.17: The summarized OSSE results for the test case considering deviations by an inaccurate electromagnetic framework. The true OIMF is calculated using X3DG, but the imposed field is approximated using the law of Biot-Savart. The top row shows the final scale factor k_f (left side) and its associated uncertainty STD of k_f (right side). The bottom left plot shows the deviation of the final scale factor to the optimal scale factor k^{opt} calculated by least-squares method. The bottom right plot shows the signal recovery by the assimilation ($\Lambda^{\mathrm{recovery}}$).

factor determination close to the optimal rescaling regardless of significant deviations between the imposed and true OIMF. Consequently, the discrepancies in the scale factor to previous scenarios cannot be justified by an incorrect rescaling. Instead, the small final scale factors (e.g., in the Southern Ocean around Australia and parts of the Indian Ocean) indicate incompatibilities in the temporal behavior between the true and imposed signal.

Finally, signal recovery by the assimilation (bottom right plot in Figure 4.17) clearly exemplifies this by showing substantial differences. Compared to the test case scenario considering slight spatial deviations (see Figure 4.13), the initial chosen scale factor of zero cannot be improved significantly in extended oceanic areas. The average global signal recovery is 0.04 (compared 0.31 in the OSSE scenario described in Section 4.4.2). The imposed EM signal can only be recovered in areas around the equator and the East Pacific. These areas are in perfect accordance with the correlation between the OIMF

prediction from X3DG and Biot-Savart (see Section 3.2.4 and especially Figure 3.4).

It can be concluded that a high correlation between the imposed and true signal is an essential condition for adequate signal recovery. Since temporal behavior is the crucial part of the separation, this underlines distinctly that a high correlation between the imposed and the true OIMF is necessary to identify the oceanic magnetic signal. This test case scenario also revealed that an appropriate electromagnetic framework is of great relevance, and identifying oceanic EM signals requires precise modeling of the electromagnetic induction processes. Accordingly, discussed influences on the OIMF calculation (like the surrounding conductance or the quasi-stationary approximation) will indeed affect the detection of EM signals using KREMS. Moreover, this scenario proved the simplified Biot-Savart approach to be insufficient as presumed OIMF estimate. The lack of predicting the correct temporal behavior using Biot-Savart in decisive areas prohibits oceanic EM signal identification.

4.4.5 Deviations by observation-based presumed estimate

This final test case scenario is addressed to the observation-based detection of oceanic EM signals using KREMS. The OSSE was used to investigate whether observation-based presumed OIMF estimates would lead to a reasonable scale factor using KREMS. Therefore, the geostrophic approach was used to derive the OIMF. This approach was already explained in Section 2.3 and validated in Section 3.3. According to that, the geostrophic OIMF, which was derived from sea surface height data of the GLOCER ensemble mean, is used in this OSSSE to mimic an observation-based OIMF estimate. In this OSSE scenario, the geostrophic OIMF estimate was used as imposed magnetic field, and a full-model-based OIMF estimate was incorporated in the artificial observations as the true oceanic signal. In doing so, the deviations between the true and imposed field in this OSSE stem from the geostrophic approach.

The results of this OSSE scenario are shown in Figure 4.18. The scale factor could be determined with a globally very low scale factor uncertainty, 0.14 % on average. The scale factor shows larger values deviating from the initial zero value in the Southern Ocean (0.25 on average). Near the equator, the scale factors remain close to zero, 0.02 on average.

The last test case using Biot-Savart (Section 4.4.4) already indicated the importance of the correlation between imposed and true magnetic fields. Therefore, the scale factor determination was additionally analyzed regarding the correlation between the geostrophic OIMF and the true model-based EM signal. Hence, the results are presented in Figure 4.18 (bottom plots) by showing the absolute final scale factor and its final uncertainty for each grid point in dependence on the absolute correlation between the imposed and true signal. Additionally, either the deviation from the optimal scale factor or the variability

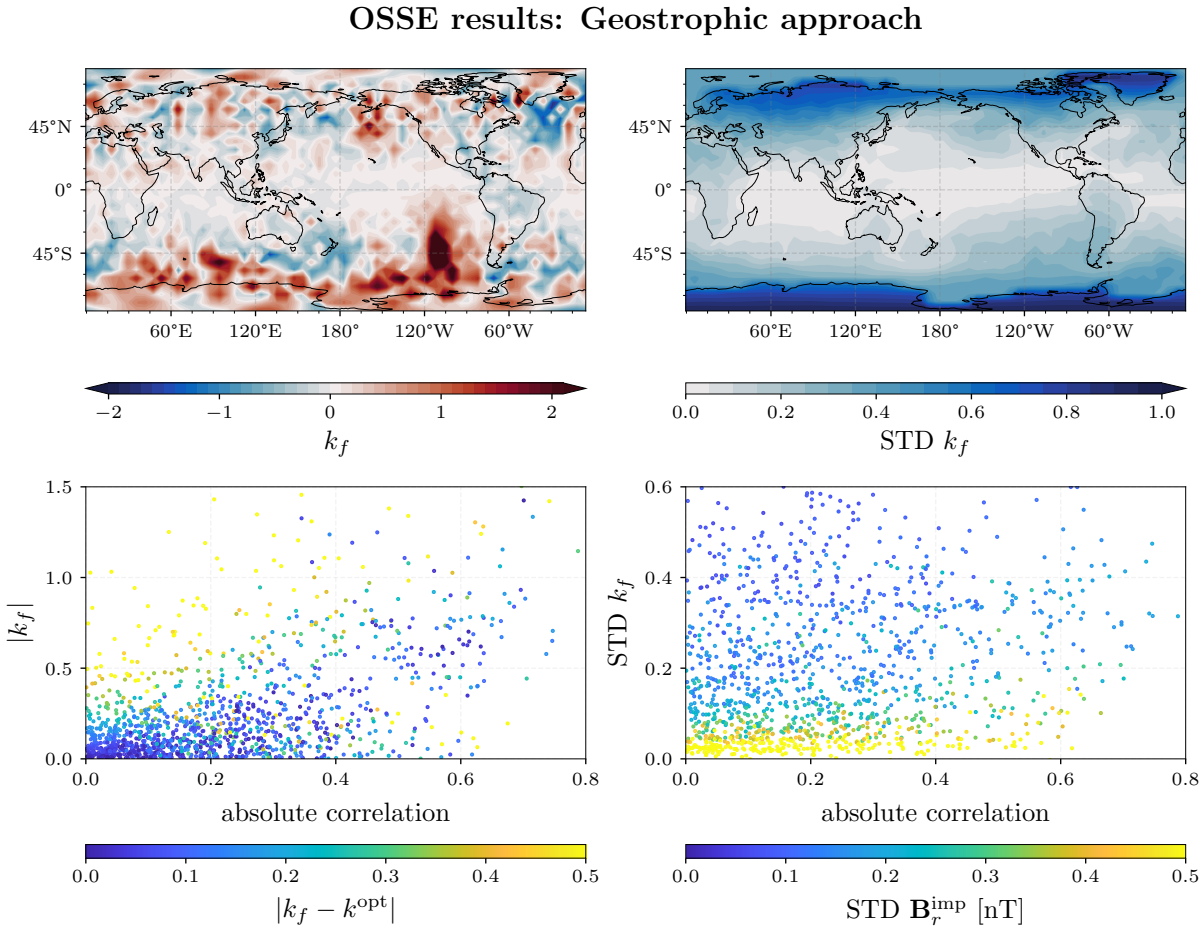

Figure 4.18: The OSSE results using a geostrophic OIMF as imposed magnetic field and a full-model-based as the true magnetic signal. The top row shows the final scale factor and corresponding uncertainty after the assimilation. At the bottom, the absolute final scale factor $|k_f|$ (left) and corresponding uncertainty STD of k_f (right) is plotted over the absolute correlation between imposed and true signal. In the bottom left, the deviation to the optimal scale factor is highlighted in color. In the bottom right, the imposed variability is highlighted in color.

of the imposed oceanic signal is highlighted. In accordance with the previous findings, two important conditions for an appropriate scale factor determination can be derived from Figure 4.18.

First, the determined scale factor, which represents a measure of detectability, increases for higher correlations between true and imposed signals (Figure 4.18, bottom left panel). In particular, higher scale factors with lower deviation from the optimal scale factor, i.e. an accurate signal identification, showed also a higher correlation. On the one hand, this leads to a weak correlation between the geostrophic OIMF and the true signal; on the other hand, to an unrealistic, exaggerated geostrophic EM signal. Therefore, a scale factor close to zero near the equator could either indicate a weak detectability due

to the weak correlation or a reasonable downscaling of the exaggerated signal. Without further information, these scenarios are indistinguishable.

Secondly, as already stated several times, high variability in the imposed OIMF is needed to reduce the final scale factor uncertainty and achieve a precise scale factor determination. Scale factors at grid points with high imposed OIMF variability (colored in Figure 4.18 bottom right panel) expose remarkably lower uncertainty (STD k_f). Interestingly though, Figure 4.18 also indicates that this is independent of the correlation between the imposed and true signal. Consequently, a high correlation is not required to achieve a low uncertainty of the scale factor. In turn, a result of the scale factor with low uncertainty does not necessarily reveal a high correlation. Therefore, based on the uncertainty, a low value of the scale factor (e.g., near the equator) can still indicate both a weak detectability (low correlation) or reasonable downscaling (high correlation).

Overall, it can be concluded from this scenario that in areas where the geostrophic OIMF show high variability, a scale factor with low uncertainty can be determined independent of the correlation between geostrophic and true OIMF. If the imposed geostrophic OIMF also strongly correlates with the true one, the resulting scale factors exhibit higher values indicating good detectability. Finally, the scale factor results with low values and low uncertainty are challenging to interpret. In this OSSE, the geostrophic OIMF estimate was, in principle, successfully used as an observation-based OIMF estimate. However, the correlation proved vital to obtain conclusive results, which must be considered when applying the geostrophic approach.

4.5 Further discussion and conclusion

4.5.1 Limitations by temporally constant rescaling

In some cases, the result of the previous scenarios already exemplified a limitation of KREMS. Despite a reasonable scale factor determination, the signal correction was limited (e.g., test case scenario of Section 4.4.2), and even a weak signal recovery occurred (e.g., test case scenario of Section 4.4.4). In these cases, even the optimal scale factor calculated using a least-square fit revealed these limitations. In general, KREMS aims for an amplitude correction and assumes a rescaling constant in time. However, temporally constant rescaling strongly restricts the signal correction in these cases. When the scale factor is assumed to be constant over time, it cannot correct temporally varying deviations between the imposed magnetic field. In order to overcome these limitations in correcting the imposed signal, a time-dependent rescaling would be required.

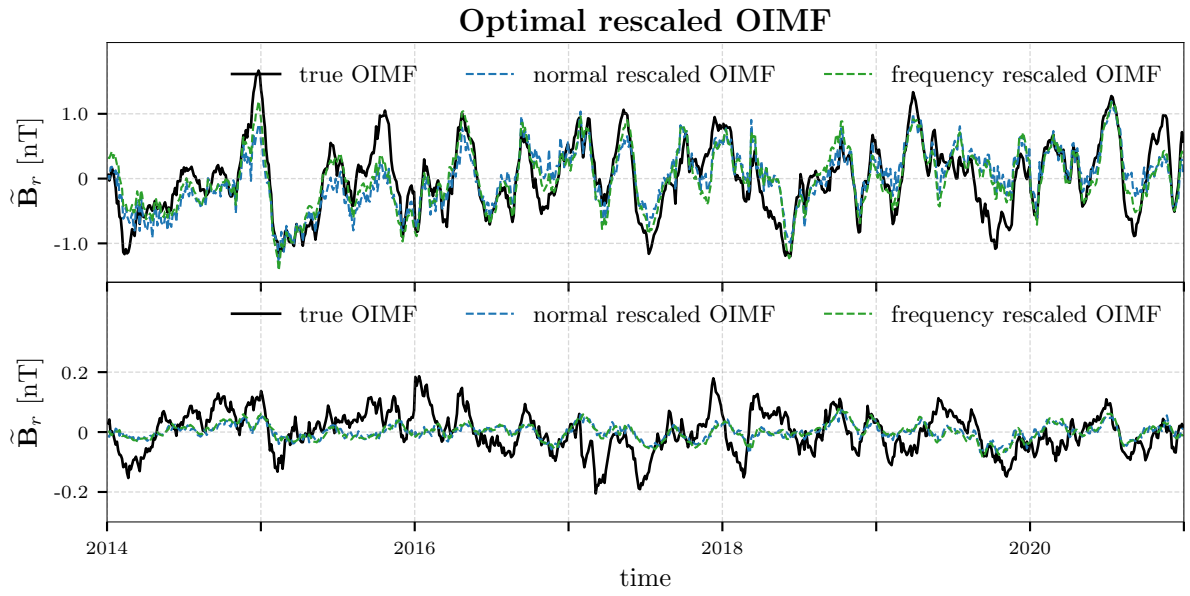

Figure 4.19: Exemplary time series of true and rescaled OIMF. Two types of rescaled imposed OIMF are drawn. The normal-rescaled OIMF using a constant optimal scale factor (blue) and a frequency-rescaled OIMF using a scale factor for each considered frequency band (blue).

A possible approach to introduce a time dependence of the scale factor is to decompose the imposed signal in different components and, afterward, determine a scale factor for each part. A simple frequency decomposition of the imposed signals was performed in Section 4.4.3, demonstrating that a scale factor could also be determined for each imposed signal component. Separately imposing the frequency components takes advantage of the fact that KREMS can be used with any predetermined EM signal. Instead of one, the

total EM signal would then be rescaled with four different frequency band-dependent scale factors. This frequency-rescaling is compared with the normal rescaling as used before based on a single scale factor. The comparison is shown in an example in Figure 4.19.

It can be seen from this figure that determining several scale factors for each frequency component only slightly increases the correction compared to a normal rescaling based on one single scale factor for the total EM signal. On the one hand, decomposing the OIMF into several parts heavily decreases the imposed variability and, therefore, the method's sensitivity. On the other hand, determining a scale factor only for a small number of signal components has only a little effect on the temporal dependence of the correction. Therefore, even though rescaling several temporal components is easy to perform using KREMS, it must be carefully chosen. In the example shown here, the frequency-rescaling does not represent a significant improvement. Consequently, achieving an effective time-dependent rescaling would require a different approach. One has to conclude that the assumption of a constant scale factor remains a major limitation of KREMS.

4.5.2 Influence of other magnetic sources

Modeling and recovering the other magnetic sources will affect the scale factor determination of the oceanic source. In general, the Kalmag assimilation distinguishes between internal and external sources. As one of the internal sources, the ionospheric field is arguably a strong competitor for the separation of ocean-induced magnetic fields. In comparison, the other two internal sources from the core and lithosphere differ more clearly in time behavior since they develop much slower. Most of the ionospheric influence is avoided by the selection of nighttime data and low geomagnetic activity. Moreover, the crucial areas of this assimilation are the mid-latitudes (due to the applied data selection below 60° and low ocean-induced signals at the geomagnetic equator). In this case, the solar-quiet magnetic fields dominate the ionospheric component. Since studies like Suzuki (1978) and Takeda (2002) found that low degrees of SH can capture the solar-quiet fields, the ionospheric component was simulated in the OSSE up to an SH degree of 5 in the first place. However, the treatment of the ionospheric magnetic field still affects the sensitivity of KREMS. Therefore, the possible ionospheric influence must be considered when applying KREMS outside of this OSSE.

4.5.3 Comparison to tidal-induced electromagnetic signals

In conclusion, a comparison is drawn to the existing approach to detect tidal-induced EM signals with Kalmag (see Section 2.2.4). As stated in Section 2.2.4, the successfully employed extension of the Kalmag model for tidal OIMFs can not be used to identify

OIMF from circulation. However, the introduced KREMS in this thesis could also be applied to tidal-induced EM signals. Instead of a single frequency, KREMS allows the identification of signals with a more general temporal behavior. In principle, this more general imposed temporal behavior could also be chosen as a simple harmonic oscillation. Although this is less promising as a direct frequency-dependent separation, it allows for the comparison to the detection of tidal-induced EM signals.

Another simple OSSE is performed to show the generality of KREMS and demonstrate the scale factor determination in a different context. In this scenario, the tidal transports from the TPXO8 dataset (Egbert and Erofeeva, 2002) are used to compute the tidal-induced EM signals. Instead of the OIMF derived from the ECCO2 model data, the principal lunar semi-diurnal constituent ocean tide constituent (M2) is derived from TPXO8. The OIMF time series derived from TPXO8 is then included in the artificial Swarm-like observations. Hence, in this scenario, the true OIMF is a magnetic signal induced by the semi-diurnal M2 tide. Subsequently, an hourly time series of a simple harmonic oscillation is used as imposed OIMF.

In doing so, the correct temporal behavior is imposed, and at each grid point, a scale factor corresponding to the oscillation amplitude can be determined. In this scenario, a valid scale factor at each location would describe the amplitude of the tidal OIMF from the M2 ($\hat{\mathbf{B}}_r$). Thus, the M2 tidal signal contained in the artificial data can be extracted using KREMS. The results of this OSSE are presented in Figure 4.20.

The top row shows the final scale factor and its associated uncertainty. Additionally, these results are compared to the amplitude of the M2 tidal-induced magnetic signal. As a first comparison, a direct forward calculation of the tidal OIMF based on TPXO8, which represents the true OIMF in this scenario, is presented (bottom left). Secondly, the M2 OIMF amplitude extracted from real Swarm satellite data using the extended Kalmag model is also shown (bottom right). The scale factor determined using KREMS clearly reveals the pattern of the M2 amplitude. The results of the OSSE showed a strongly decreased uncertainty. Consequently, the amplitude of the presumed harmonic oscillations was adapted with very low uncertainty to the correct M2 amplitude. The spatial pattern of the amplitude obtained by KREMS is much noisier than the results using the direct approach for tidal-induced EM signals of Kalmag. However, the spatial resolution of the scale factor is slightly higher (SH degree of 30), and no spatial constraints are included. The OSSE results demonstrate the generality of KREMS to rescale the amplitude of any EM signal.

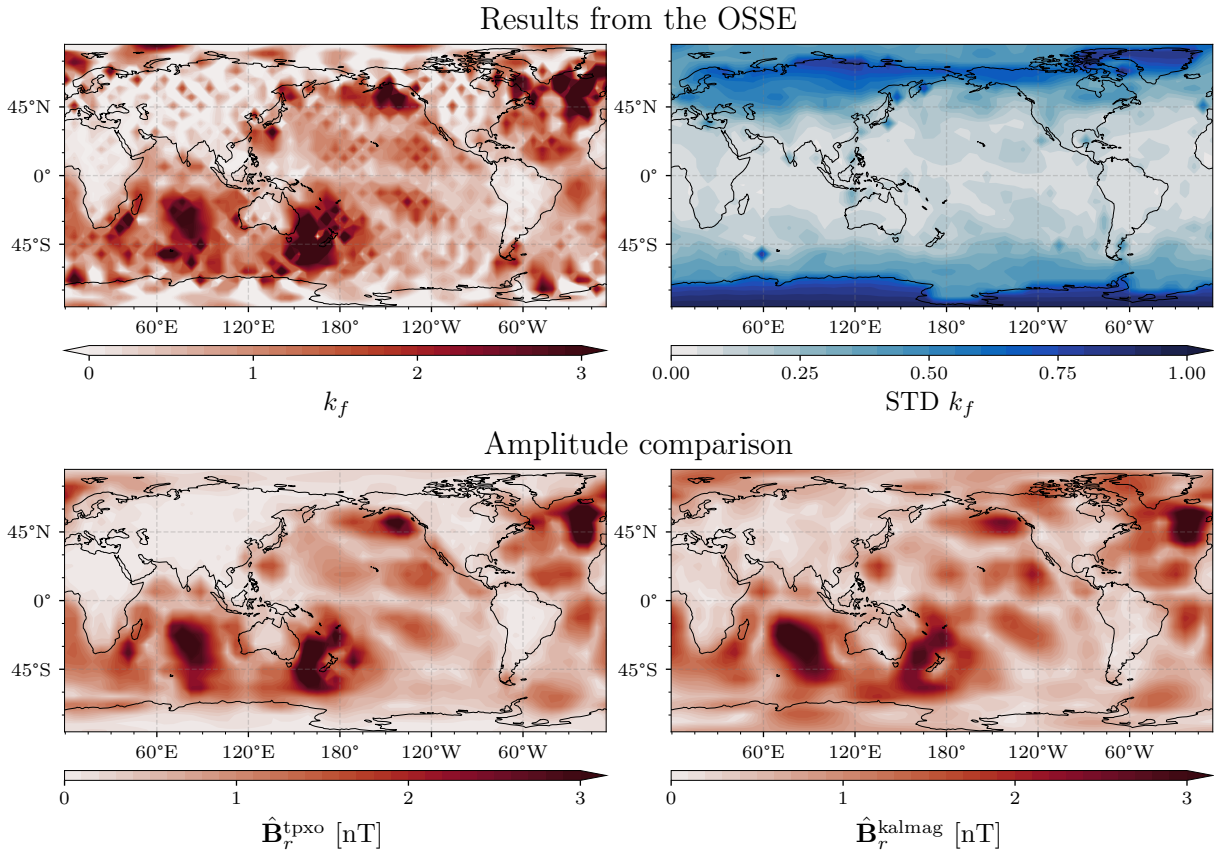

Figure 4.20: Comparison of KREMS with the existing approach to detect tidal-induced EM signals. The results of an OSSE considering the EM signals induced by the M2 tide are shown in the top row. Both the final scale factor (left), which in this case corresponds to the amplitude of the OIMF by the M2 tide, and the associated uncertainty (right) are presented. At the bottom, the amplitude of the radial magnetic field induced by the M2 is shown as a comparison. The left side presents the M2 amplitude directly from TPXO ($\hat{\mathbf{B}}_r^{\text{tpxo}}$), which is considered the truth in the OSSE. The right side shows the M2 amplitude recovered by the Kalmag model from satellite data ($\hat{\mathbf{B}}_r^{\text{kalmag}}$) using the existing approach to detect tidal-induced EM signals.

4.5.4 Conclusion

In this chapter, KREMS as detection method for possible identification of ocean-circulation-induced magnetic signals in geomagnetic satellite observations was introduced. In the context of an OSSE, the method could be successfully validated. The challenging separation of the oceanic signals from other magnetic field contributions could successfully be achieved by imposing the temporal behavior and using a Kalman filter-based assimilation. The results of this OSSE show that a scale factor could be determined regardless of the complex temporal behavior and the low intensity of the magnetic field from ocean circulation. A reasonable scale factor determination in the ideal scenario of the OSSE (Section 4.2) indicates a high capability of the proposed method to detect EM signals from ocean

circulation. A clear advantage of KREMS is the combination of a scale factor and the associated uncertainty allowing a meaningful interpretation of the results. Another benefit is the locally varying rescaling allowing a more specific analysis in different ocean regions. Based on the analysis in Section 4.2.4, KREMS yielded accurate results, especially for larger spatial resolution (up to SH degree 15). The sensitivity of KREMS proved to be sufficient for a scale factor determination within the considered period of seven years of assimilated data. The results of the OSSE also pointed out the main dependencies on the variability of the presumed OIMF estimate and latitude. Furthermore, the optimality of KREMS was demonstrated by showing that the determined scale factor is close to a rescaling obtained by a least-squares fit. The optimality also remained unchanged in non-ideal scenarios indicating a certain robustness of the KREMS. Finally, the comparison of KREMS to the approach for tidal-induced EM signal detection showed the generality of KREMS.

Apart from that, the rescaling in some cases revealed also limitations of KREMS. A rescaling constant in time is limited in corrections of the presumed OIMF estimates. Therefore, KREMS cannot sufficiently correct the presumed OIMF estimate when deviations between this estimate and the ground truth vary strongly with time. A high correlation of the presumed OIMF estimate with ground truth revealed a necessary condition for signal identification.

5

Real-world application: Detectability of the ocean-induced magnetic field in Swarm satellite observations

5.1 Applicability to geomagnetic satellite observations

5.1.1 Comparision of real and artificial satellite observations

The last chapter has introduced KREMS as method to detect OIMFs from the ocean circulation. The analysis and evaluation have been discussed in the context of an OSSE and, therefore, were based on synthetic artificial measurements. The following chapter aims to adapt the method for its application to actual satellite observations. The detectability of different presumed proxies of the ocean-circulation-generated magnetic field in Swarm satellite data will be investigated. Furthermore, a purely observation-based identification of OIMF is examined by estimating the presumed estimates from altimetry or multiobservational data.

The used geomagnetic satellite observations from the Swarm satellite mission are identical to the ones used before to derive the orbiting positions for the artificial data. The measurements of the Alpha and Bravo satellite at a sampling rate of every 10 s were taken, and the same selection was applied (nighttime selection below 60° and low level of geomagnetic activity). First, with regard to the application of the method on this real Swarm satellite data, a comparison of these magnetometer data with the artificial measurements

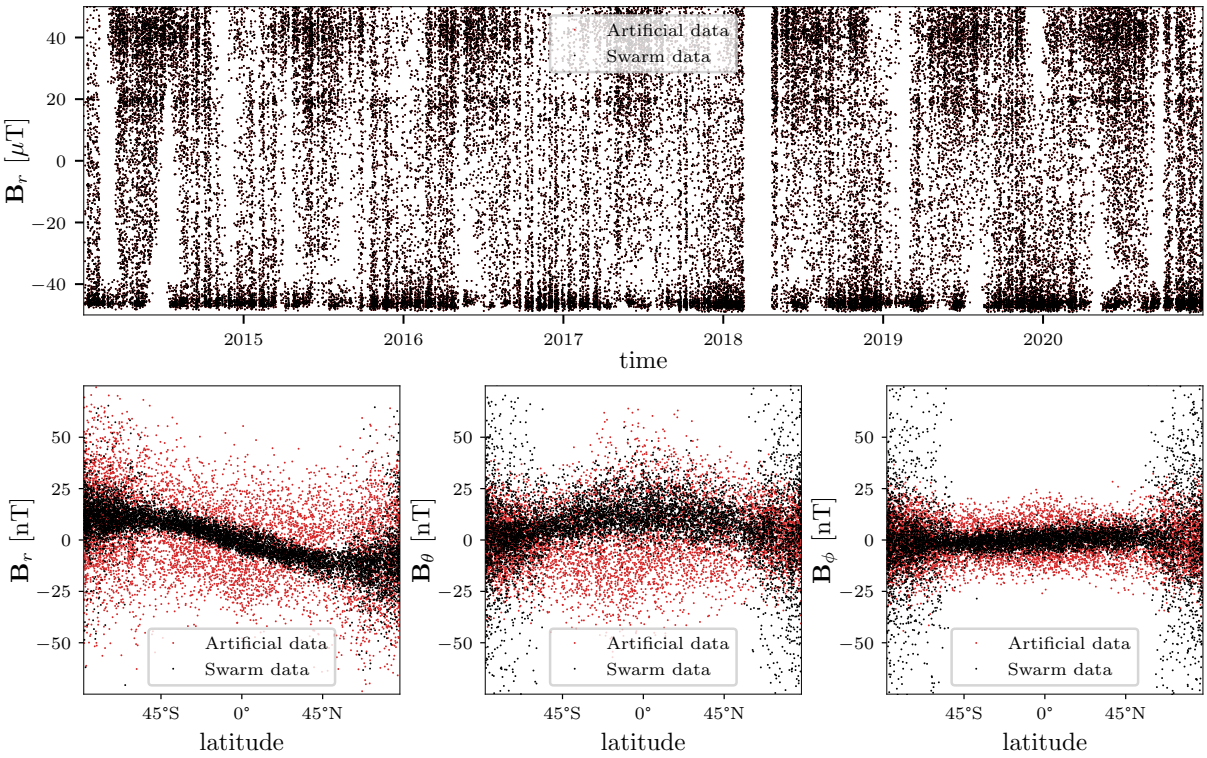

Figure 5.1: Comparison of the selected vector field magnetic satellite measurements from Swarm and the artificial data used in the OSSE. The top panel shows the radial component of each 100th satellite measurement over the complete time series. The residuals from the core and lithosphere components, depending on the latitude, are shown in the bottom row for each vector field component of the year 2014 (again, each 100th measurement) The artificial data used in the presented OSSE are marked in red; the real Swarm observational data are marked in black.

used in the OSSE was made to identify potential differences. This comparison of artificial and real data is shown in Figure 5.1.

The upper images of Figure 5.1 initially present the comparison of every 100th measurement of the crucial radial component of the geomagnetic field over the complete time series. The measurement series of artificial and real geomagnetic satellite observations are very similar due to the equivalent satellite track selection,. The individual measurements are close together and barely distinguishable compared to the radial magnetic field magnitude range (see top plot in Figure 5.1). The core and the lithospheric component of the geomagnetic field dominate the satellite measurements. The similarity in the time series of measurements indicates that these components are captured well in the artificial data and that the artificial data reasonably represent realistic satellite observations.

However, a more detailed comparison is needed to investigate more minor deviations which are important for oceanic contributions. Therefore, the core and lithosphere components of the Kalmag model were subtracted from both datasets. The corresponding

residuals of all three vector components ($\mathbf{B}_r$, $\mathbf{B}_\theta$, $\mathbf{B}_\phi$) of each 100th measurement are analyzed in dependence on the satellite latitude position. This comparison of the remaining magnetic field measurements is presented in the bottom plot of Figure 5.1, exemplary for the year 2014. On the one hand, the comparison shows that the residuals of both artificial and Swarm magnetic field measurements are again in the same order of magnitude and similar shape. On the other hand, the comparison also discloses differences between the artificial and the real Swarm measurements. The variability of the residuals in the artificial data, especially in the radial component, is larger around the equator and lower at higher latitudes than in the Swarm observations in the θ and ϕ components. The lower variability in the higher latitudes of the non-radial components could be well explained by missing field-aligned currents, which are not considered when building the synthetic data set. The increased variability of the artificial data residuals at lower latitudes, particularly the radial component, could indicate an overestimation in the prior of the ionosphere component around the equator.

5.1.2 Adaptation to real satellite observations

When KREMS is applied to real swarm data, the magnetic field sources are treated the same way as in the OSSE. However, in contrast to the OSSE, a source accounting for field-aligned currents is also included in the Kalman filter. This source of field-aligned current is evaluated as in the original Kalmag model and described in Section 2.2.3. The ionosphere is considered as before. On the one hand, Baerenzung et al. (2022) demonstrated that the ionosphere-induced magnetic source of the Kalmag model is consistent within induction processes. On the other hand, the data comparison of artificial and real observations indicates some deviations the ionosphere could cause. Especially, modeling the ionosphere at nighttime remains challenging and may require further investigations. Therefore, in the context of this thesis, at least different spatial resolutions are considered for the ionosphere. For the ocean-induced magnetic field, the method is exactly applied as introduced and analyzed in the OSSE. The following will examine the detectability of several imposed magnetic field (i.e., presumed OIMF estimates). Thereby, the scale factor is considered as a measure of detectability and will be initiated at the beginning of the assimilation again following a Gaussian normal distribution $\mathcal{N}(0, 1)$. The ocean-induced magnetic field is typically considered up to a spatial resolution of SH of degree 30 or 15.

Additionally, also ground-based observatory measurements are taken into account during the assimilations of Swarm satellite observations. Further information about the included observatories and their locations are listed in Baerenzung et al. (2022). Consequently, the number of assimilated data is increased compared to the OSSE. The inclusion of observatory measurements will primarily help to constrain the core field and its secular

variation. That, in turn, will facilitate the separation of the ocean-induced magnetic field from the other sources.

5.2 Detectability of ocean model based estimates

5.2.1 Presumed estimate from ECCO2

The investigations about the detectability will depend on the initial assumptions utilized for the imposed magnetic field. In the first place, the ECCO2 model data (see Section 3.1), which was employed in the OSSE, is considered a presumed estimate and taken to constrain the temporal behavior of the OIMF. In this first detectability study using real Swarm satellite observations, the imposed signal relies entirely on the ECCO2 model. As in the OSSE, oceanic velocities, as well as conductivity (resulting from temperature and salinity), were used to provide seven years of a 3-daily-mean time series of snapshots of OIMF from 2014.0 until 2021.0. According to the previous results of the OSSE, spatial constraints of the scale factor are incorporated by an exponential decaying covariance. First, a correlation length of 500 km is considered. Furthermore, the source accounting for the ionosphere is performed up to a spatial resolution of SH degree 5.

Results

The results of the assimilation of the real Swarm satellite data and the imposed ocean-induced magnetic field from ECCO2 are presented in Figure 5.2. The final scale factor determined in 2021 (Figure 5.2, upper left panel) clearly deviates from its initial value of zero, indicating a partial temporal accordance with the imposed signal in the assimilated observations. In this case, a comparison to the optimal scale factor is impossible since the true signal in the Swarm observation is unknown. Therefore, the associated uncertainty of the determined scale factor is of particular value for the evaluation of the results. The uncertainty of the scale factor (measured as STD of k_f, Figure 5.2 upper right panel) show, as expected, a weak pattern related to the variability of the imposed magnetic signal. However, the uncertainty is generally much higher than in the OSSE at all locations, implying less uncertainty reduction could be achieved by the assimilation. Especially, the minimal arisen uncertainty is only 0.54 compared to 0.06 in the OSSE. The high uncertainty is also pointed out in the area-weighted spatial averages of the scaled factor and its associated uncertainty over the main oceanic areas listed in Table 5.1. Consequently, the determination of the scale factor is much more inaccurate in this case compared to the OSSE (see Table 4.2). The bottom plots of Figure 5.2 also visualize the mean imposed and rescaled ocean-induced magnetic field. Thereby, the mean rescaled field again exem-

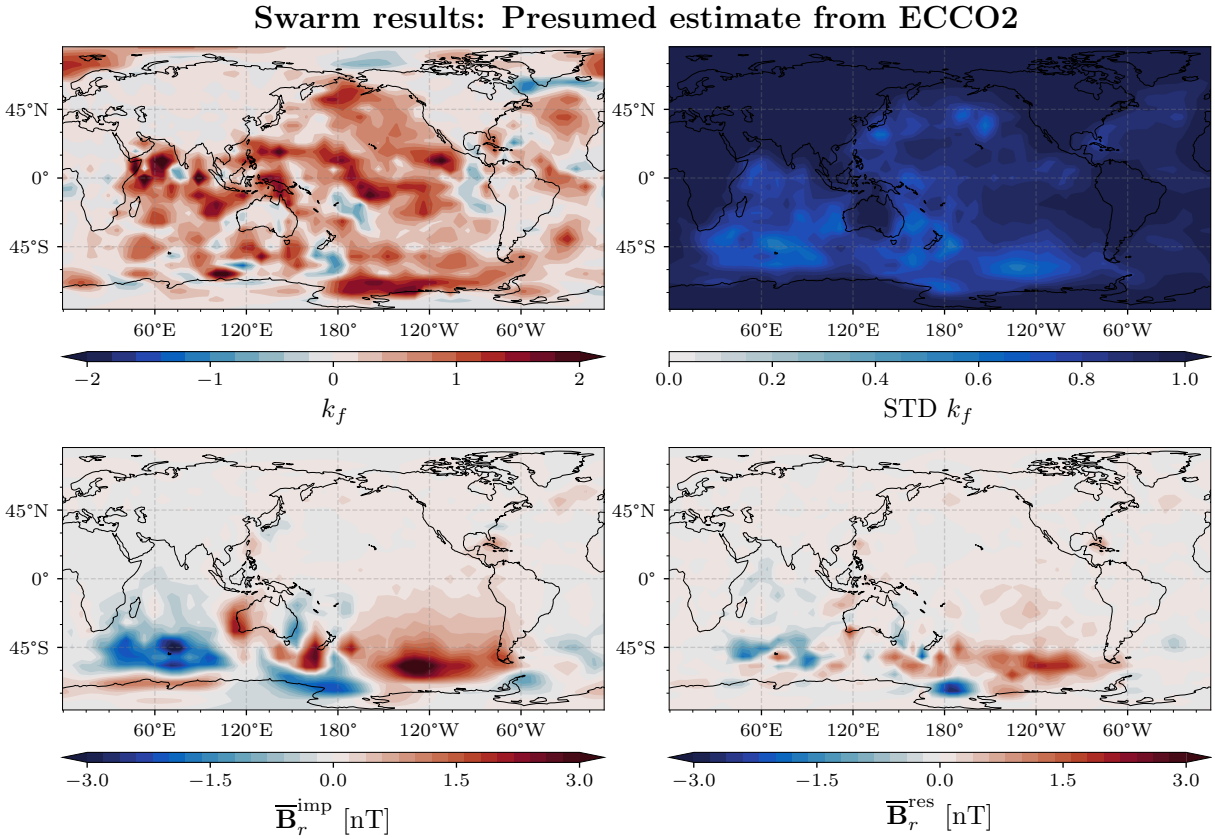

Figure 5.2: The assimilation results based on Swarm observations and using an imposed OIMF estimated from the ECCO2 ocean model data. The upper plots show both the final scale factor k_f (left) and the associated uncertainty (posterior standard deviation) of the final scale factor k_f (right). The assimilation was initialized with a scale factor of zero and a corresponding uncertainty of one.

plifies the amount of signal recovered from the satellite observations. Both imposed and rescaled fields differ significantly, and the latter is much less intense in most parts.

Detailed analysis

Additionally, the energy spectrum of the imposed and the rescaled OIMF is shown in Figure 5.3, allowing the comparison of both fields on different spatial scales. In general, the energy spectrum of the rescaled field differs significantly from the imposed one (compared to the energy spectrum in the ideal scenario of the OSSE in Figure 4.9), showing again that the imposed signal could not or only partly recovered. However, an adaption of the energy spectrum of the rescaled OIMF to the imposed one can be found at lower SH degrees (up to SH degree of 15). In accordance with the findings based on the OSSE (see Section 4.2.4), this indicates a better signal recovery on larger spatial scales. Signals of spatial scales greater than degree and order of SH 15 have lower energy in the imposed

Table 5.1: Area-weighted spatial averages of the final scale factor and its associated uncertainty

Area	**scale factor k_f**	**uncertainty (STD of k_f)**
Atlantic	0.15	0.92
Pacific	0.48	0.86
Indian Ocean	0.56	0.78
Southern Ocean	0.38	0.80
Full oceanic area	0.38	0.86

signal and are, consequently, harder to identify.

Two possible principal explanations come into question for the poorer signal recovery and the larger uncertainty compared to the OSSE. On the one hand, a lower signal-to-noise ratio compared to the OSSE could decrease the sensitivity of KREMS. On the other hand, an incorrect imposed temporal behavior of the presumed estimates could result in larger incompatibilities with the ground truth of the OIMF in observations. Both would result in higher uncertainty of the determined scale factor and, therefore, indistinguishable when considering the scale factor uncertainty exclusively. Even though interpreting the scale factor is more difficult without knowing the optimal factor, a more detailed consideration reveals further indications of the higher uncertainty cause. The scale factor convergence introduced and shown in Section 4.2.2 using the OSSE provides a valuable opportunity for such an analysis. Therefore, the complete assimilation is repeated, but the initial scale factor values are slightly changed following a Gaussian normal distribution $\mathcal{N}(2, 1)$. The corresponding scale factor convergence as the absolute difference of the final scale factors

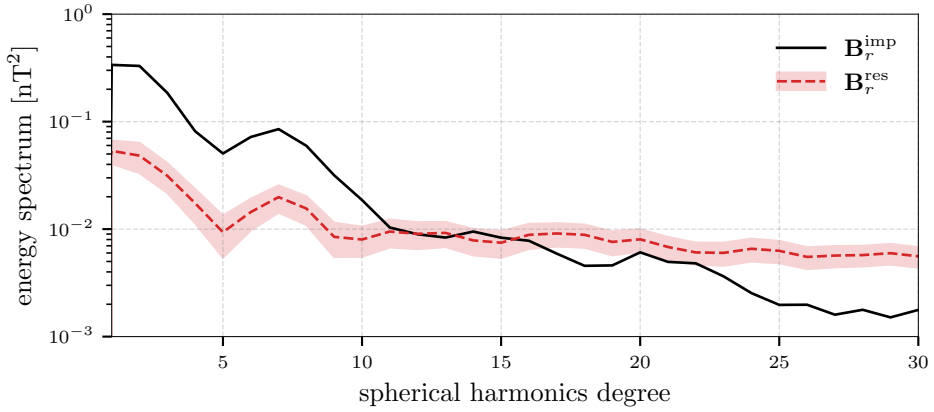

Figure 5.3: The energy spectrum of the imposed and the rescaled OIMF from the assimilation of Swarm observations using presumed estimates from ECCO2. The mean imposed OIMF energy spectrum is drawn in black; the mean rescaled OIMF and its associated uncertainty are shown in red.

from both assimilation ($|k_f^2 - k_f^0|$) is shown in Figure 5.4 (top panel).

The scale factor convergence reveals a distinct area where the assimilations lead to similar results despite different initial conditions. A good convergence (low difference between the final scale factors) means a significant change in at least one of the scale factors due to assimilation. That demonstrates the method's sensitivity and indicates that an incorrect temporal behavior of the presumed estimates causes the still remained high uncertainty. On the downside, a poor convergence (high difference between the final scale factors) implies unchanged initial scale factors. That, in turn, exposes an insensitivity and indicates a too-low signal-noise ratio to recover the imposed signal. This distinction is also pointed out by the scale factor evolution.

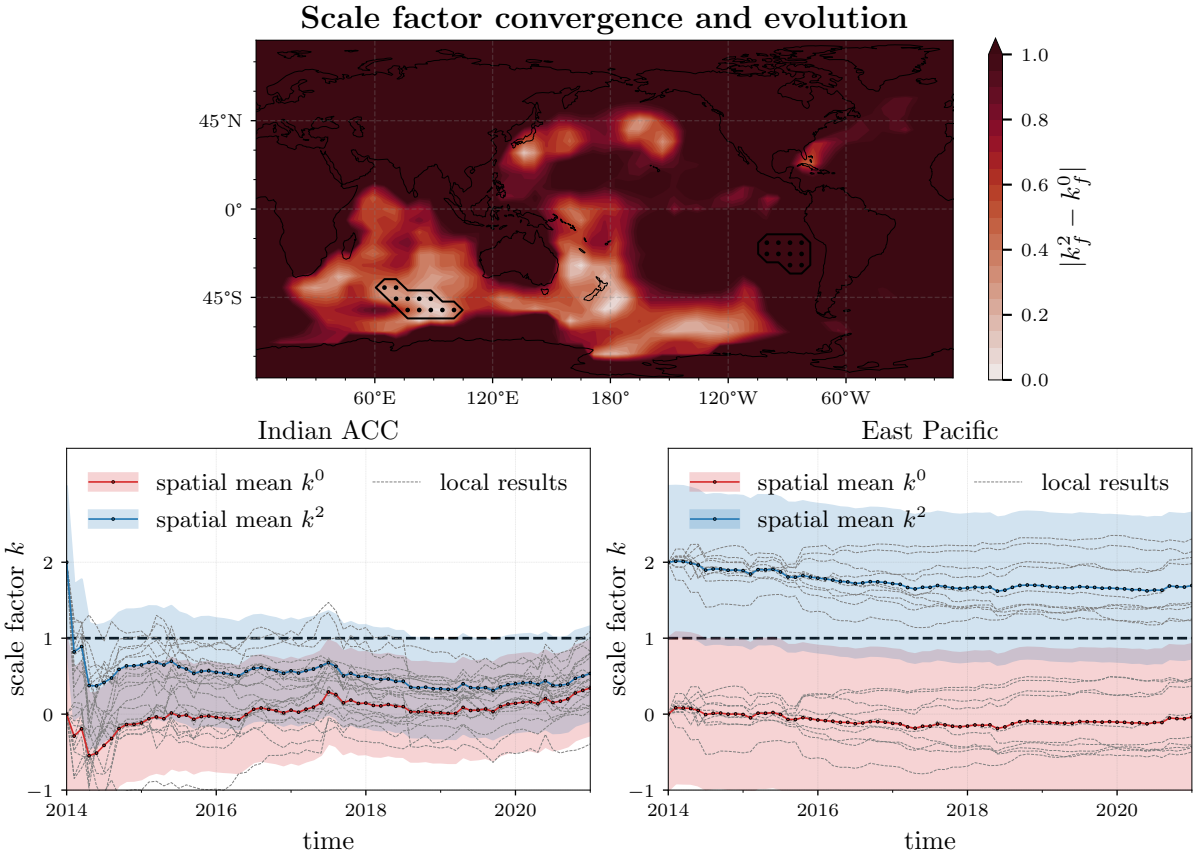

Figure 5.4: The plot shows the scale factor convergence (top) as the difference between two final scale factors from differently initialized assimilations. Light colors indicate good convergence (small scale factor-differences), and dark colors poor convergence (large scale factor-differences) The bottom plots show the evolution of both scale factors over the entire assimilation period in two different areas. The areas (Indian ACC and East Pacific) and their containing grid points are equal to the previously studied areas (see Figure 4.4) and marked again in the top panel. The grey lines denote the pointwise local factors, and the red lines highlight the spatial area-weighted averaged mean and uncertainty (posterior standard deviation).

Figure 5.4 (bottom panel) shows the area-weighted spatial average of scale factor evolution and the corresponding local results in the same two areas already investigated in the OSSE in the previous chapter (Figure 4.5): The Indian ACC area (high imposed variability and good convergence), and the East Pacific area (low imposed variability and poor convergence). In the East Pacific, it is clearly visible that both scale factors remain unchanged, and the imposed OIMF cannot be detected there. However, in the Indian ACC, both initial scale factors converge together and demonstrate the conclusiveness of the scale factor. This scale factor convergence analysis shows that compared to the OSSE, the poorer signal recovery is not only explained by an increased signal-to-noise ratio but also by a larger incompatibility between the imposed and the true OIMF. Although the analysis of the proposed method in Section 4.4 indicated a certain robustness of the scale factor determination concerning the imposed OIMF, the results of the OSSE were purely based on the ECCO2 model, which means that the imposed and the in the artificial data included signal are still based on the same model. However, in particular, the oceanic transport predictions and the resulting OIMF anomalies may vary more widely. Therefore, in the application to real Swarm observations, incompatibilities of the temporal behavior between the imposed and the true signal play a decisive role in the scale factor determination and explain the larger scale factor uncertainty in areas of good convergence.

Influence of assimilation parameters

Finally, the presumed estimates from ECCO2 are used to test the influence of some assimilation settings and parameters. Here, the previously shown result serves as a reference. The different assimilation results are compared by the spatial average of the scale factor over the area exhibiting a good convergence (scale factor difference is less than one, meaning at least 50% reduction). An overview of the result is given in Figure 5.5. First, the influence of the included observatory data is examined. Since the observatory data is just used as secular variation data to constrain the core field better, the effect is little on the OIMF identification and, therefore, not visible in the shown area-weighted average of the final scale factor. Secondly, the assimilation is performed using different correlation lengths of the exponential decaying covariance matrix incorporated in the Kalman filter. A clear improvement is visible when using the exponential decaying covariance matrix. Lastly, the parameter for spatial resolution of the magnetic source accounting for the ionosphere is varied in the assimilation. The results show a deterioration through an increased spatial resolution of the ionosphere.

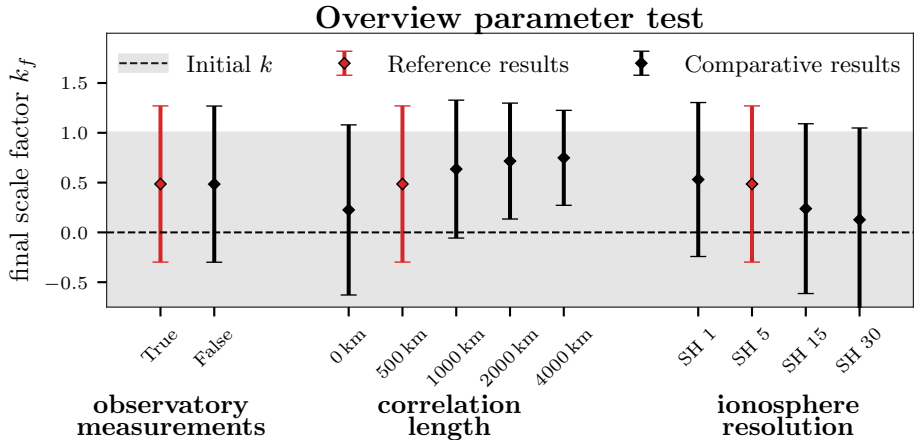

Figure 5.5: An overview of the assimilation result using different settings based on the presumed estimates from ECCO2. The results are compared by the area-weighted average of the scale factor and its uncertainty. The considered area is defined via a good scale factor convergence (see Figure 5.4, top panel).

5.2.2 Presumed estimate from GLOCER

The assimilation results in the previous section based on the presumed OIMF estimates from the ECCO2 model showed the functionality and general applicability of KREMS on Swarm observations. However, the results also suggest a significantly reduced sensitivity of KREMS compared to the OSSE in Chapter 4. Even in areas where a conclusive scale factor determination was possible, considerably larger uncertainties occurred. In this context, the question was raised to what extent potential incompatibilities of the imposed and the real signal in the Swarm satellite data affect the assimilation and scale factor determination. This question is strengthened by the fact that the results so far were only based on the presumed OIMF estimates from the ECCO2 model. In order to examine this in more detail, further imposed magnetic fields are tested and compared to extend the variety of the presumed OIMF estimates. Therefore, the global ocean ensemble reanalysis (GLOCER) dataset introduced in Section 3.1 was considered. In the following, both the ensemble mean, and the three individual members (ORAS5, GloSea5, and GLORYS) were taken and used to derive various presumed OIMF estimates instead of the ECCO2 model. All data sets provide 2557 time steps of daily means (from 2014.0 until 2021.0) of 3D ocean velocities, temperature, and salinity fields. Hence, the calculation of the OIMF can be kept as before. These further assimilations are used to investigate the dependence of the results on the presumed estimates of the OIMF.

At first, the results of the assimilation based on the imposed field retrieved from the ensemble mean of the GLOCER dataset are considered. According to the findings before, the final results are evaluated only up to more reliable spatial scales of SH degree 15.

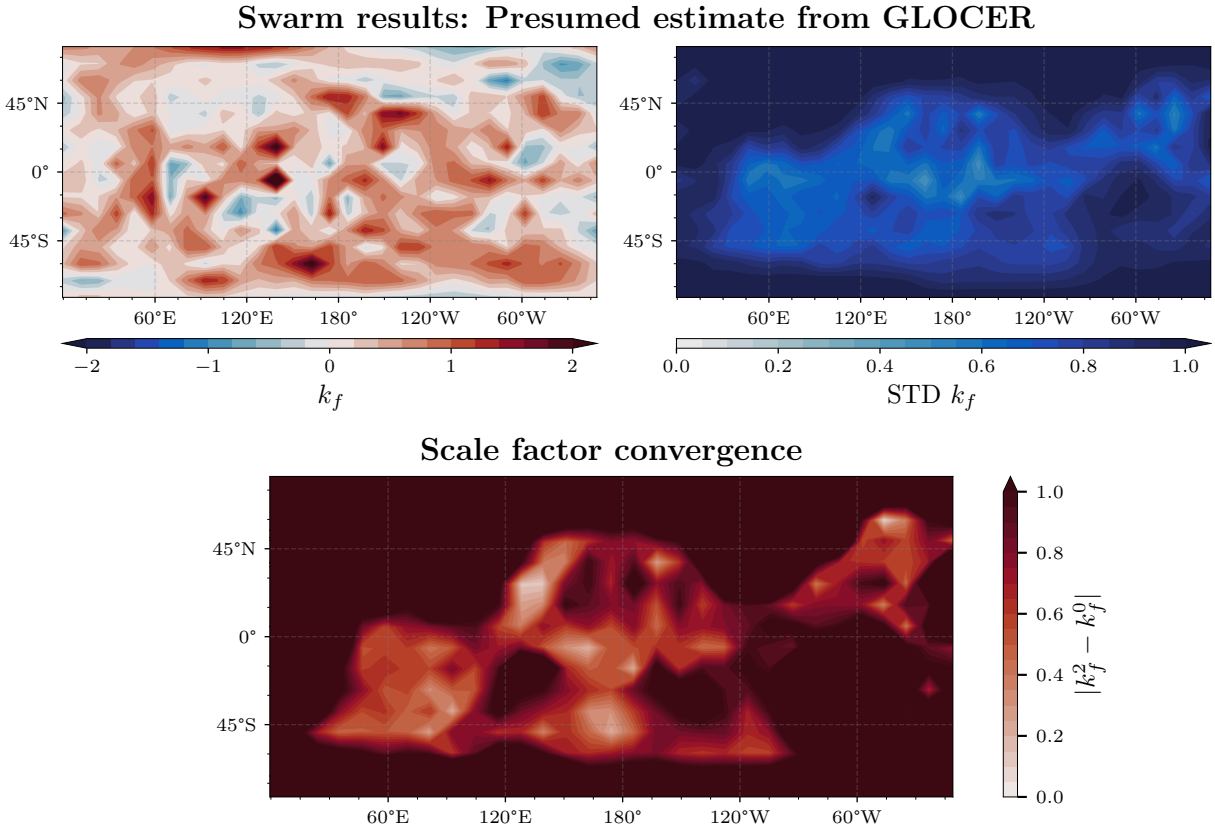

Figure 5.6: The assimilation results based on Swarm observations and using an imposed OIMF estimated from the ensemble mean of the GLOCER dataset up to SH degree of 15. The upper plots show both the final scale factor k_f (left) and the associated uncertainty (posterior standard deviation) of the final scale factor k_f (right). The bottom plot shows the scale factor convergence as the difference between two final scale factors of assimilations with different initial values.

Figure 5.6 presents the final scale factor and its associated uncertainty (top panel) and, additionally, the scale factor convergence (bottom panel, calculated using a second assimilation with different initial values as described before). Generally, the scale factor determination results are also less conclusive than in the OSSE, and an overall larger scale factor uncertainty arises. In this case, the uncertainty can again, at best, only be reduced to 0.42. Nevertheless, the pattern of the scale factor and the associated uncertainty evidently differs from the results based on the ECCO2 model. Since the imposed OIMF was changed, also the imposed variability was altered in this assimilation. The scale factor determination, and especially the pattern of the associated uncertainty, is obviously affected by that. However, this already illustrates the strong dependence on the imposed signal. Likewise, the scale factor convergence pattern changed to the results based on the presumed estimate from ECCO2. However, general regions of good

convergence remain similar, like areas of the Indian Ocean, the Southern Ocean around New Zealand, and also the areas of the Kursoshio or the Gulf stream, which correspond to the areas of higher variability of oceanic EM signals. Interestingly, the scale factor differs also in areas of comparable lower uncertainty and good convergence, which indicates a considerable influence of the OIMF detectability on the imposed temporal behavior.

The dependence on the imposed temporal behavior can even be more affirmed by looking at the different assimilation results of the individual members of the GLOCER data set. Both imposed variability of the EM signal as well as the scale factor results vary widely between the individual ocean reanalysis product (ORAS5, GloSea5, GLORYS).

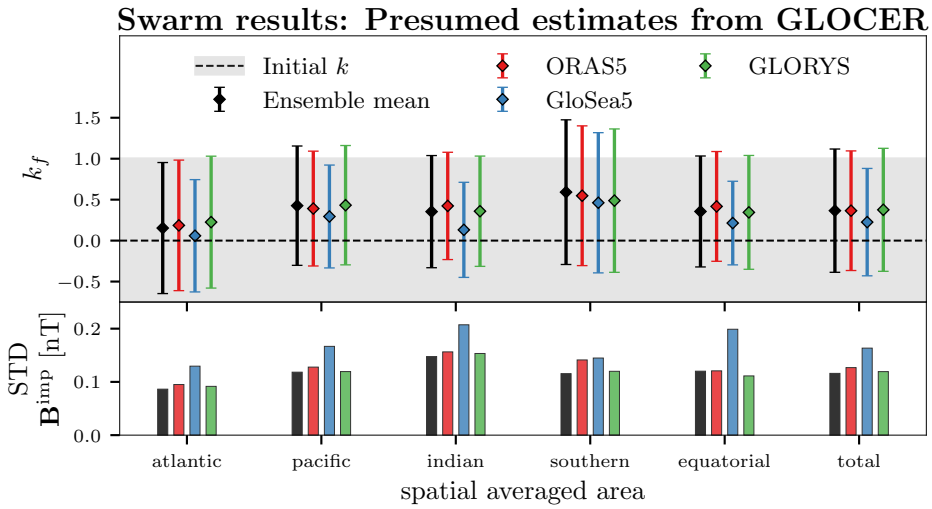

Figure 5.7: An overview of the assimilation outcomes based on Swarm observations and using different imposed OIMFs from the individual ensemble members (ORAS5, GloSea5, GLORYS) of the GLOCER dataset. The results are compared by the area-weighted average of the scale factor and its associated uncertainty (top panel) in different ocean basins. In the bottom plot, additionally, the averaged imposed variability of each ocean product in each area is shown to evaluate the results better.

Figure 5.7 gives an overview of the results by showing the spatial area-weighted mean of the final scale factor and its associated uncertainty in different regions (according to Figure 4.4) and comparing the results of the individual ocean reanalysis products. In addition, the average imposed variability for each presumed estimate in each area is highlighted in the figure for a better evaluation. Even though only the spatial area-weighted mean over large ocean basins is shown in this figure, significant differences in the results can be seen. These averaged scale factors already indicate different detectability of the imposed OIMFs from the individual ocean products in different areas. Unfortunately, the scale factor uncertainty remains very large for all products in most areas. Even the initial scale factor of zero is within the range of the spatially averaged uncertainty in all considered areas. General differences between the areas are as expected from the previous results,

e.g., lower detectability in the Atlantic Ocean and higher detectability in the Southern Ocean but with larger uncertainty due to the higher latitudes.

When comparing the individual results, the assimilation outcome based on the GloSea5 product consistently shows a lower averaged uncertainty, which is well in accordance with its higher imposed variability. However, in all areas, also the average scale factor using the imposed OIMF from GloSea5 is lower than the ORAS5 and the GLORYS product results. The higher imposed OIMF variability allows, on the one hand, a more precise signal identification (lower scale factor uncertainty) but, on the other hand, results, in this case, in a lower signal accuracy (lower scale factor). The low accuracy of the recovered imposed signal is assumably explained by either an incorrect temporal behavior or an overestimation of the imposed OIMF. High variability in the imposed OIMF caused by an incorrect temporal behavior results also more likely in a low scale factor. However, an overestimation of the imposed OIMF would also exhibit a higher variability and result in a lower scale factor to scale down the overestimated imposed signal. In contrast, the results based on the GLORYS product show comparable high averaged scale factors but also with high associated uncertainty. A lower imposed variability explains the lower scale factor uncertainty.

In this case, the higher scale factor could indicate either a better temporal accordance of the imposed OIMF with the true one or a partly underestimation of the imposed signal. Interestingly, also compared with the ORAS5 product results (with similar imposed variability), the average scale factor based on the GLORYS product exhibits a larger scale factor in some areas,e.g., the Atlantic and Pacific Oceans. The individual results for each assimilation using the different ocean products as imposed OIMF are shown in the Appendix A.10 for a more detailed comparison. Generally, the variety in the different assimilation outcomes confirms a stronger dependence of the results on the imposed temporal behavior. Consequently, this points out again the importance of imposing an exact temporal behavior to identify small variations of the circulation-induced magnetic field anomalies. However, the temporal behavior of the considered presumed estimates of the OIMF differs significantly, indicating that the deterioration of the scale factor determination compared to the OSSE is explained to a large extent by insufficient presumed estimates of the OIMF.

5.3 Detectability of observation-based estimates

5.3.1 Presumed estimate from altimetry data

The considered presumed OIMF estimates could not, or only to some extent, be identified in Swarm observations with KREMS. Nevertheless, the following presents an advanced approach toward an ocean model independent identification of the OIMF. Especially emphasized by the results of the global ocean ensemble reanalysis in the previous section, the OIMF detectability heavily relies on the presumed estimate from an ocean model and, therefore, can not be seen as a model-independent identification. However, the objective of the following is a purely observation-based identification of the circulation-induced EM signals. As suggested earlier in this thesis and proposed by Saynisch et al. (2018), the combination with altimetry measurements is considered to achieve this goal. Therefore, the presumed estimates taken from ocean model data are replaced with OIMF predictions from independent altimetry observations. The geostrophic approach to obtain OIMF estimates from altimetry observations was already validated in Section 3.3. Moreover, the principle use of the geostrophic OIMF as presumed estimates in KREMS was also shown in the OSSE (Section 4.4.5).

Despite the raised caveats during this validation, the application of this approach to real Swarm satellite observations will be investigated in the following. Therefore, altimetry data from the Data unification and Altimeter Combination System (DUACS) is used. DUACS is a multimission production system of altimeter data and provides combined high-quality altimeter data from several missions (see Section 3.1). The sea surface height data from ocean model data was replaced by the eastward and northward geostrophic velocities taken from DUACS. Here, 366 timesteps from 2014 until 2021 of weekly velocity data are considered. Apart from that, the required ocean conductivity can be taken directly from the World Ocean Atlas 2018 (WOA18) instead of derived from an ocean model. The WOA18 provides a dataset of an observation-based statistical mean of ocean conductivity. Even though the conductivity is assumed constant over time in this way, the WOA18 allows a sufficient conductivity description for the derivation of the OIMF estimates. In order to obtain the geostrophic OIMF from the DUACS data, the geostrophic velocities are assumed to be constant until ocean depth from the ETOPO1 dataset and subsequently weighted by the depth-averaged WOA18 ocean conductivity. Based on these conductivity-weighted velocities from the DUACS data, the geostrophic OIMF can be derived using X3DG and used as presumed estimate for KREMS.

Figure 5.8 (top row) presents the mean and the standard deviation of the estimates from DUACS used as imposed OIMF. The radial magnetic field amplitude is more extensive than the magnetic field derived from ocean model data (compare to Figure 4.1). This

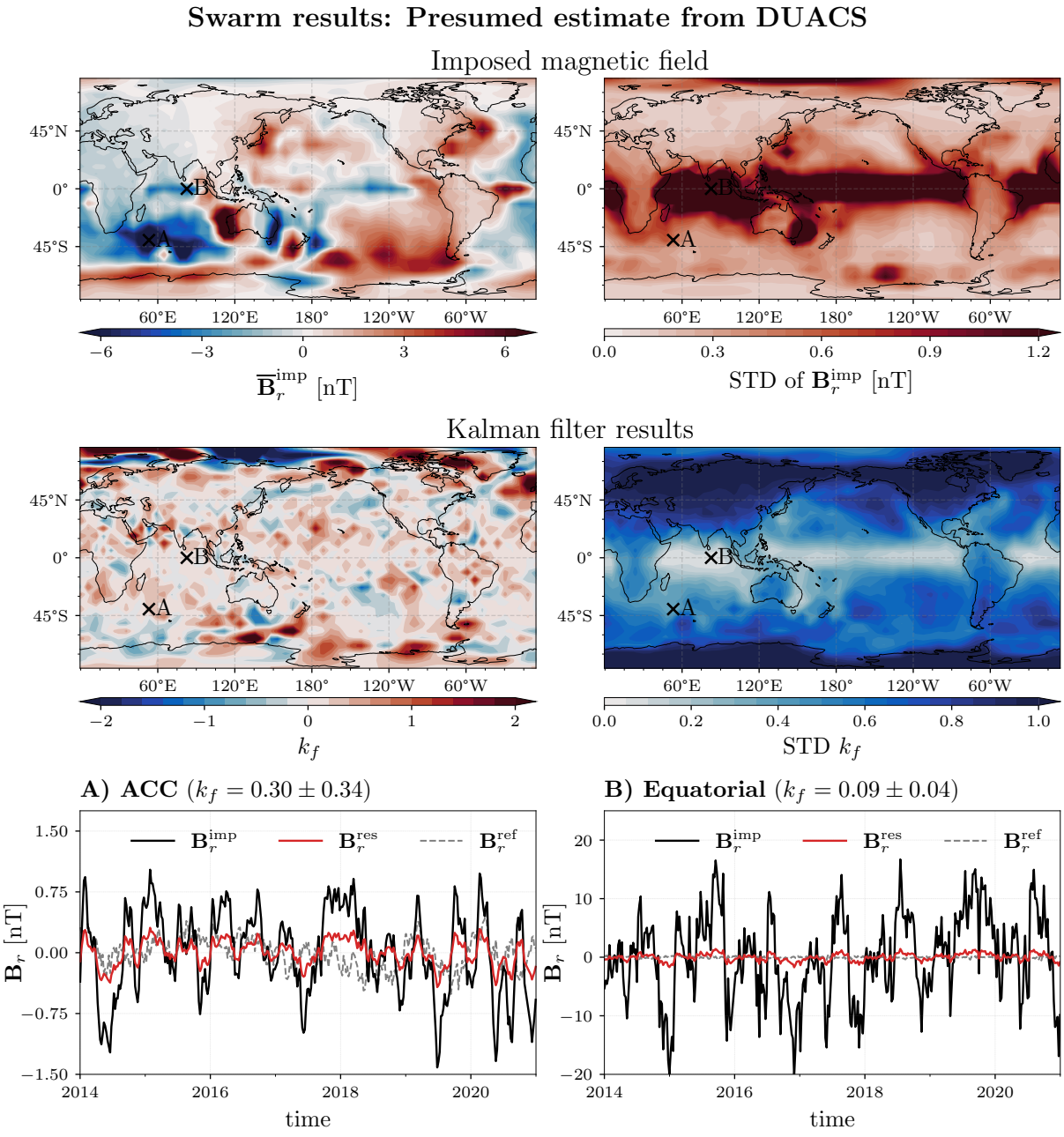

Figure 5.8: A summary of the assimilation results using presumed estimates from altimetry based on the DUACS product. The top row shows the imposed magnetic field's mean (left) and corresponding standard deviation (right). In the middle, the final resulting scale factor (left) and its associated uncertainty (right) are shown. At the bottom, the time series of imposed (black) and rescaled(red) magnetic fields are illustrated at two different locations. Additionally, in grey, the time series from the GLOCER ensemble mean is shown as a reference.

enhancement is caused by the overly strong assumption of constant geostrophic velocities until ocean depth. Furthermore, around the equator, the standard deviation of the geostrophic OIMF is evidently intensified. Since the Coriolis force vanishes at the equator, the invalidity of the geostrophic approximation in this region leads to unrealistically high magnetic fields.

Eventually, the Kalman filter assimilation is then initialized with scale factors following the normal distribution using the exponential decaying spatial correlation with a correlation length of 500 km. The assimilation results of the Swarm observations are demonstrated as usual in terms of the final scale factor and its standard deviations as associated uncertainty in Figure 5.8 (middle row). On the one hand, the high variability in the equatorial band yields a very low uncertainty of the scale factor (0.22 on average in the equatorial area). On the other hand, the final scale factors in this area remain close to zero (0.04 on average in the equatorial area). Concluding from this, the unrealistic extensive geostrophic signal at the equator cannot be found in the Swarm observations. Remarkably, the scale factor's low uncertainty clearly supports this conclusion. However, as already discussed in the OSSE (Section 4.4.5), it must be considered that a scale factor close to zero, despite a low uncertainty, is still difficult to interpret. It is indistinguishable whether a low correlation between the imposed signal with the ground truth or the exaggerated amplitude of the imposed EM signal causes the results.

In other oceanic areas, the uncertainty is significantly higher, and the pattern of the scale factors could be more conclusive and less noisy. Moreover, two exemplary locations in the Indian ocean are marked: A) at the ACC and B) in the equatorial region. Gridpoint A) at the ACC show a partial detectability with a final scale factor of 0.3. According to the previous findings, this indicates a partial correlation between the imposed geostrophic signal and the true OIMF at this location.

Figure 5.8 (bottom row) shows the time series of the imposed and the final rescaled magnetic field at this location. In addition, the OIMF resulting from an ocean model is depicted as a reference. This illustration reveals the overestimation due to the geostrophic assumption again. However, the rescaled geostrophic OIMF is much closer to the OIMF retrieved from an ocean model, demonstrating the plausibility of the scale factor. Similarly, the time series at location B) in the equatorial region confirms a reasonable rescaling. The overestimated imposed signal is rescaled close to zero in agreement with the OIMF estimate from an ocean model.

5.3.2 Presumed estimate from multiobservational data

An issue of the presumed estimates from altimetry data, like the DUACS data, is the inconclusive assumption about the depth-integration of the geostrophic surface velocities to

obtain the transports. Even though the method is only sensitive to the OIMF anomalies and the crucial aspect is their temporal behavior and not their amplitude, the assumption of constant geostrophic velocity is deficient. This assumption of depth-constant conductivity weighted velocities not only leads to overestimating but also neglects relative changes with depth. Moreover, avoiding an overestimation could be beneficial by preventing the scale factor from being too close to zero.

A potential improvement of geostrophic OIMF estimates, which still purely rely on observations, was already discussed in Section 2.3.4 and is explored in the following. In order to accomplish this, the altimetry data is combined with in-situ temperature and salinity profiles to obtain 3D geostrophic velocities (see Section 2.3.4). The ARMOR3D dataset introduced in Section 3.1 represents a possible multiobservational ocean data product combining temperature and salinity measurements and altimetry data. In Section 3.3.2, it was already demonstrated that this combination improved the OIMF estimate by reducing the RMSD to the model-based OIMF. Here, the presumed OIMF estimate, based on the multiobservational ARMOR3D dataset, is considered and the corresponding assimilation results are discussed. The OIMF can be estimated similarly to the purely altimetry-based DUACS estimates from the previous section and considered in the same time period and temporal resolution. However, since the ARMOR3D dataset is also based on in-situ measurements, the conductivity can be calculated from the corresponding temperature and salinity fields instead of using the data from WOA18. In doing so, the presumed OIMF estimate consistently relies on the ARMOR3D dataset.

Figure 5.9 illustrates the assimilation results of real Swarm satellite observations using the presumed OIMF estimate based on the ARMOR3D dataset. The final scale factor (top left) and its associated uncertainty (top right) are presented. The final scale factor still exhibits an inconclusive, noisy pattern and indicates no significant improvement in EM signal identification. Overall, the corresponding uncertainty of the scale factor is higher than the uncertainty from the DUACS product estimates. The global average is 0.67 compared to 0.48 for the estimates from DUACS. This is explainable by the lower imposed variability due to lower overestimation in the presumed OIMF estimates caused by a more realistic determination of the EM signal magnitude. The uncertainty is clearly diminished in the equatorial region, where the presented method is particularly sensitive, but the altimetry-based estimates are inaccurate due to the invalidity of the geostrophic approximation. In this equatorial area, the scale factor uncertainty is 0.44 compared to 0.22 for the estimates from DUACS. However, the average scale factor in the equatorial area is 0.02, even smaller than the average from DUACS of 0.04. Unfortunately, the more realistic OIMF estimation from ARMOR3D did not help to avoid a scale factor close to zero.

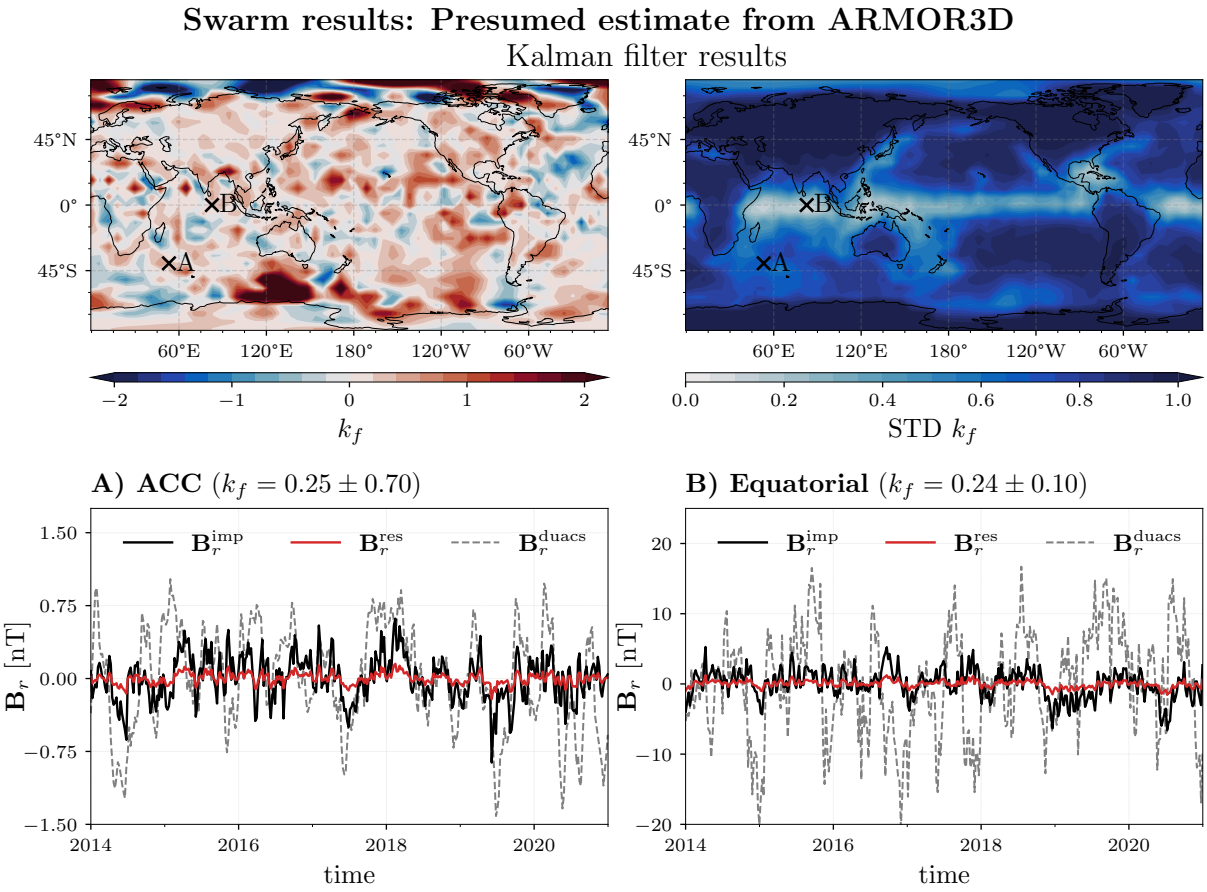

Figure 5.9: The assimilation results based on the presumed estimates from the multiobservational ocean product ARMOR3D. The top row shows the final scale factor (left) and its associated uncertainty (right). At the bottom, the time series of imposed (black) and rescaled (red) magnetic fields are illustrated at two different locations. Additionally, in grey, the time series from the OIMF estimate based on the DUACS dataset is shown as a comparison.

As in Section 5.3.1, the time series of the imposed and the rescaled OIMF at the same two exemplary locations, A) at the ACC and B) in the equatorial region, is shown. The time series are compared to the OIMF estimates from the DUACS dataset considered in the previous section. On the one hand, this comparison shows the improved presumed OIMF estimate by the ARMOR3D dataset, especially in the equatorial region (a less extensive geostrophic signal), but on the other hand, the presumed OIMF estimate is still scaled down by KREMS. The downscaling, in combination with the high uncertainty in the ACC, indicates a poor or only partial identification of the ocean-circulation-induced EM signal.

In conclusion, compared to the model-based result in Section 5.2, KREMS using observation-based estimates provide results of similar quality. Consequently, KREMS can be, in principle, used for purely observation-based detection. In particular, the equato-

rial area revealed interesting results when using satellite-altimetry-based presumed OIMF estimates. KREMS determined a scale factor close to zero in combination with remarkably low uncertainty. This clearly shows that the EM signal derived from the DUACS or ARMOR3D was not found in Swarm satellite observations. Whether this is due to low temporal correlation or overestimated amplitude is difficult to distinguish. Preparatory studies showed a low correlation but also amplitude comparison revealed an overestimation. However, such inaccuracies are reasonable in the equatorial region due to the invalidity of geostrophic approximation. The presented results at least demonstrate the potential of KREMS to correct such inaccuracies and indicate the benefit beyond the pure detectability of EM signals.

6 Conclusion

6.1 Summary

This thesis deals with the observation of electromagnetic (EM) signals caused by general ocean circulation. These so-called ocean-induced magnetic fields (OIMF) provide a beneficial source of information due to their sensitivity to ocean conductivity (i.e., temperature and salinity), ocean flow velocity, and the Earth's mantle conductivity. Moreover, the remotely measurable radial component of OIMF allows for a global observation through space-borne satellite magnetometers. Remote sensing techniques for the ocean often only allow surface observations (e.g., satellite altimetry). In contrast, oceanic EM signals depend on the depth-integrated ocean velocities and provide indirect information about the whole water column. Therefore, observing oceanic EM signals provides the opportunity to access large-scale oceanic water mass transports indirectly by space-borne satellite measurements. However, the OIMF is only a tiny contribution (around $\pm 4\,\mathrm{nT}$) to the total geomagnetic field (ranging from 25 to $65\,\mu\mathrm{T}$). Since geomagnetic observations exclusively measure the total magnetic field, the detection of oceanic EM signals requires a separation from other magnetic field contributions. The precision of magnetometer satellite missions, such as CHAMP and Swarm, theoretically enabled the detection of oceanic EM signals for the first time. While tidal-induced EM signals were successfully extracted from geomagnetic satellite observations, a suitable approach to extract ocean-circulation-induced EM signals is missing so far.

In this thesis, a novel method was developed to address the challenge of identifying

ocean-circulation-induced EM signals in Swarm satellite observations for the first time. A Kalman-filter-based rescaling of EM signals (KREMS) using the geomagnetic field model Kalmag was proposed to achieve the essential separation from other geomagnetic field contributions. The crucial aspect of this separation is an adequate prior characterization of the oceanic EM signals based on their temporal variations. Therefore, in KREMS, the entire temporal behavior of the oceanic EM signals is characterized by a presumed estimate to account for the complex temporal pattern of the irregular ocean current. The Kalman filter is then used to locally rescale the amplitude of these given presumed estimates by a temporal constant factor by the assimilation of geomagnetic observations. In the context of this thesis, KREMS is used with different presumed estimates of the OIMF to evaluate their detectability via the resulting scale factor from assimilation. For this purpose, the assimilation was initiated with a completely downscaled amplitude of the presumed OIMF estimate, and the detectability was measured after full assimilation. If the amplitude remained downscaled, the signal was unidentifiable; otherwise, the final scale factor states that the signal was identified in observations.

Presumed OIMF estimates

In the first place, the required presumed OIMF estimates for KREMS are derived from ocean model data. However, in addition, observation-based OIMF estimates that allow for purely observational signal identification were also considered in this thesis.

Generally, these presumed OIMF estimates were calculated using the X3DG electromagnetic induction solver X3DG. It has been demonstrated that most of the OIMF variability is driven by the ocean flow velocities. Additonally, the OIMF was also estimated in a first approximation based on the law of Biot-Savart, which would facilitate future inversions of the magnetic field. A comparison of this simplified approach with the OIMF calculations from X3DG showed an averaged global difference of 0.3 nT and an average correlation of 0.4. However, these simplified presumed OIMF estimates proved to be insufficient for adequate signal identification using KREMS since in decisive areas (e.g., Southern Indian and Pacific Oceans), larger deviations (up to 3 nT) and a inconsistent temporal behavior occurred. It can be concluded that an accurate electromagnetic framework is required when determining the presumed OIMF estimates for KREMS.

Furthermore, the observation-based presumed estimates were calculated from satellite altimetry data. According to the geostrophic balance, ocean surface velocities can be estimated from sea surface height data and used to roughly approximate the OIMF. These observation-based and model-based OIMF estimates are temporally correlated of up to 0.8 (average global correlation of 0.3). An extension by in-situ measurements allows further improvement of the observation-based OIMF estimates.

Validation and evaluation of KREMS

The validation of KREMS as a novel detection method was performed using an observing system simulation experiment (OSSE) based on synthetic Swarm-like observations and model-based OIMF estimates derived from the Estimating Circulation and Climate 2 (ECCO2). In this case, knowing the true oceanic signal contained in the synthetic observations allowed a precise evaluation of KREMS and served as proof of concept.

Using an OSSE showed that an amplitude rescaling with low associated uncertainty is possible regardless of the complex temporal behavior and the low intensity of the presumed EM signal. After the assimilation of 7 years of synthetic observations, the scale factor could be determined with a globally averaged deviation from the true value of 0.27, and the initially assumed uncertainty was vastly reduced on average, around 70% over the oceanic areas. Thus, the OSSE demonstrated that KREMS could be used to identify an oceanic EM signal in geomagnetic observations. Moreover, the locally varying scale factor allows for spatial analysis of the OIMF detectability. Local differences in the scale factor indicated a potentially better detectability in the Indian Ocean basin and parts of the Southern Ocean, as well as in individual areas influenced by large ocean currents like Kuroshio or Gulf Stream. Additionally, it was shown that an assumed a priori spatial correlation between the scale factors further improves the assimilation results. Furthermore, the evaluation of KREMS was extended to more realistic, non-ideal scenarios of the OSSE, where the presumed OIMF estimate deviates from the true signal contained in the synthetic observations. These non-ideal scenarios proved the robustness of KREMS in determining a reasonable scale factor despite different deviations and inaccuracies between the presumed OIMF estimate and the true signal. The deviations of the scale factor compared to a rescaling obtained by a least-square-fit showed the optimality of KREMS. In this sense, a given presumed oceanic EM signal is adapted by KREMS to the real signal contained in the observations as best as possible.

The extensive examination of KREMS based on the OSSE was also used to answer the research questions raised in Section 1.3:

- *What are the advantages and capabilities of KREMS?*

The chosen Kalman filter approach using Bayesian inversion proves to be particularly advantageous since it provides uncertainties associated to the results. The natural consideration of uncertainties allows including measurements or known model inaccuracies as well as incorporating dependencies on background assumptions. Therefore, the Kalman filter allows the consideration of different prior assumptions at the beginning of the assimilation (e.g., incorporating spatial correlations of the scale factors). In addition, the resulting scale factor uncertainty proved valuable for the interpretation of rescaling by

indicating how trustworthy a result is.

Another major advantage is that KREMS allows for a locally different rescaling of the amplitude of the given EM signal. The signal strength of oceanic EM signals and the accuracy of predicting and modeling the OIMF or other background sources are known to be locally different and, consequently, the signal-to-noise ratio. KREMS can account for these regional differences and answer the question at which location a globally given EM signal is best detectable.

Although in this thesis, KREMS is used to detect ocean-circulation-induced EM signals, the method is generally not limited to a specific type of EM signal. In an additional OSSE scenario, it was already exemplarily shown that KREMS can also be used to identify tidal-induced EM signals. In principle, KREMS could also be used to rescale non-oceanic EM signals. This generality could be further expanded in future studies.

- *What are the most relevant influences on the results of KREMS?*

The results of KREMS most strongly depend on the variability of the presumed EM signal. The OSSE clearly demonstrated that highly varying signals are easier to identify and can be detected more accurately due to a better signal-to-noise ratio. Particularly, no clear evidence could be found that a specific frequency band or a type of variation is easier to identify than others.

Besides the signal variability, the results depend on the geographic latitude position. KREMS allows better identification of EM signals at lower latitudes. In the OSSE, an EM signal near the equator of similar variability can be rescaled with uncertainty up to five times smaller than at a geographic position at 60° latitude.

Moreover, the detection of oceanic EM signals will always depend on the understanding and modeling of other magnetic field contributions. The findings of this thesis indicate that despite the nighttime data selection, the separation from the ionospheric magnetic field significantly influences the identification of OIMF.

- *What are the limitations of KREMS?*

KREMS identifies an EM signal by its temporal variations and, therefore, is only sensitive to the OIMF anomalies. Consequently, KREMS does not allow for the identification of the static part of an EM signal and is incapable of detecting the mean of OIMF, which would be indistinguishable from the magnetic field contributions of the lithosphere

A major limitation of KREMS is the fixed temporal behavior of the presumed estimate, which is, on the one hand, crucial for signal separation but, on the other hand, severely limits the searched signal. Accordingly, the temporally constant rescaling only allows for an amplitude correction but not for a correction of an inaccurate predefined

temporal behaviour. Therefore, the success of KREMS as a detection method relies on an accurate temporal behavior of the presumed OIMF estimate. However, this thesis showed that the considered spatial resolution, the used electromagnetic framework (e.g., assumption of the Earth's conductivity), or observation-based derivation of the OIMF estimates influence OIMF temporal behavior and consequently affect the result of the OSSE. Therefore, KREMS would benefit from improved predictions of the ocean-circulation-induced magnetic field.

A simple first approach to tackle this limitation by determining various scale factors for different temporal components of the ocean-circulation-induced EM signal proved troublesome. The temporal decomposition of the oceanic EM signal always entails a lower temporal variability, which invariably results in more difficult signal identification. In the current setup, the gain in signal detectability by a temporal decomposition of the oceanic EM signal can not compensate for the loss in sensitivity.

Application of KREMS

Finally, KREMS was applied to real Swarm satellite observations over the same 7-year period as the OSSE. The assimilation was performed using various model-based presumed OIMF estimates derived from either the ECCO2 model or the Global Ocean Ensemble Reanalysis (GLOCER) dataset. In addition, two different observation-based OIMF estimates from the satellite-altimetry-based dataset DUCAS and the multiobservational dataset ARMOR3D are considered.

The Swarm assimilation results proved to be more ambiguous and significantly deviated from the results obtained in the OSSE. The uncertainty of the rescaling was only be reduced by 14% on average for presumed estimates derived from ECCO2 and 15% for estimates derived from the ensemble mean of the GLOCER dataset. Similar to the OSSE, the best detectability was still observed in the Indian Ocean and parts of the Southern Ocean (with an uncertainty reduction of up to 20%). The determined scale factors did not reveal a consistent spatial pattern. The local results differ significantly from each other for different presumed OIMF estimates. Moreover, the KREMS results indicate an increased signal identification for lower spatial scale, higher correlation length, and lower spatial resolution of the ionosphere. Generally, the assimilation results proved to be similar when using observation-based OIMF estimates. However, the ocean-circulation-induced EM signals derived from satellite altimetry exhibit an exaggerated amplitude near the equator due to the invalidity of the geostrophic balance in this region. This equatorial signal was convincingly downscaled by KREMS. The uncertainty was reduced by 78% near the equator, and a scale factor of 0.04 was determined.

The application of KREMS also aimed to answer the remaining research questions

raised in Section 1.3:

- Can KREMS be used to identify ocean-circulation-induced EM signals in Swarm satellite observations?

Due to the high remaining uncertainty of the assimilation results, ocean-circulation-induced EM signals could not be conclusively identified in Swarm satellite observations. However, in some areas, parts of the signal could be recovered by assimilating the Swarm observations, which could be interpreted as partial detection of the EM signal. The reliability of the rescaling could be emphasized by showing that different initial assimilation conditions lead to the same result in areas of high signal variability. Therefore, two reasons come into consideration for the ambiguous results: Either the signal-to-noise ratio was too low or substantial discrepancies between the presumed and the true circulation-induced EM signal occurred. The high uncertainty of the rescaling implies an increased signal-to-noise ratio compared to the OSSE. The strong dependence of the result on different presumed OIMF estimates indicates larger incompatibilities between the presumed and true circulation-induced EM signal. The predetermined temporal behavior is subject to too many uncovered or incorrect fluctuations. The complex temporal OIMF variations are needed to identify the signal; conversely, it diminishes the accuracy of the presumed estimates.

- Is a purely observation-based detection of ocean-circulation-induced magnetic fields possible?

Similar results obtained using presumed OIMF estimates derived from satellite altimetry suggest a purely observation-based detection is possible using KREMS. The results show no evidence that the predetermined temporal behavior of observation-based OIMF estimates is insufficient for a general detection with KREMS. In particular, the downscaling with low uncertainty of the exaggerated signal in the equatorial region implies a reasonable rescaling by KREMS.

6.2 Outlook

Since it was claimed as a secondary research objective of the ongoing Swarm mission and especially in the light of future magnetic field missions like NanoMagSat, there is still a growing desire to identify ocean-circulation-induced EM signals in satellite observations. KREMS and the corresponding magnetic field observation system simulator developed in this thesis could play a decisive role in future studies and have the potential to contribute to emerging research questions.

This thesis showed that KREMS provides a tool to analyze the detectability of EM signals in Swarm satellite observations. KREMS can be adapted to different satellite constellations and additional geomagnetic observations. Concerning possible future satellite magnetic field missions, KREMS can be used to identify optimal conditions for oceanic EM signal detection.

Since KREMS is an extension of the geomagnetic field model Kalmag, the separation of oceanic EM signals would benefit from any improvement in the characterization of other geomagnetic contributions in Kalmag. In particular, KREMS could be used to investigate the impact of further advancements in modeling the ionosphere during solar-quite nighttime on the detectability of oceanic EM signals.

In future studies, the results of KREMS could be more specified by a more confined prior due to the Bayesian approach of the method. This thesis already gave an example by incorporating simple spatial correlations, but it could be expanded to a more detailed spatial pattern of the large-scale ocean flow. KREMS also allows for applied-oriented studies with more precisely defined temporal patterns of the EM signal, like seasonality due to temperature changes or trends caused by climate change. In particular, since KREMS is not limited to ocean-circulation-induced EM signals, the approach is suitable for combined analysis with tidal-induced EM signals.

The rescaling of EM signals is not limited to a measure of detectability. In this thesis, KREMS already exemplified the potential to correct observation-based OIMF estimates from satellite altimetry. In the future, KREMS could be used to independently evaluate oceanic water mass transport predictions derived from ocean models or other observations.

Based on the findings of this thesis, the following developments of KREMS are proposed to address the aforementioned limitations.
1) The sensitivity of KREMS can be increased by a better characterization of the magnetic field contribution of the ionosphere. An improved separation from the ionospheric magnetic field would increase the signal-to-noise ratio.
2) Incompatibilities between the predefined temporal behavior and the ground truth con-

tained in the observations should be tackled by identifying a more robust temporal prediction of the EM signal or weakening the temporal constraints in KREMS.
3) The limitations in correcting the EM signal by rescaling the constant in time should be addressed by a specific temporal decomposition or by considering an approach for time-dependent rescaling.
Finally, a major suggestion of this thesis is to directly rescale the sources of the magnetic field instead of the resulting field itself. Rescaling the electric current density would switch the focus from measuring the detectability towards the utilization as an ocean observation system since this electric current density is coupled directly to the desired ocean conductivity and velocities. Moreover, a linear calibration of the electric current density in this thesis already showed a better temporal magnetic field prediction, which would benefit signal separation. However, the magnetic field calculations must be inverted to rescale the electric current density. Since the simplified approach using Biot-Savart has proven to be insufficient in this thesis, this inversion has been accomplished based on an electromagnetic solver and used to obtain tidal transports (Saynisch-Wagner et al., 2023). In the future, it is recommended to incorporate this inversion to develop KREMS towards an ocean observation system.

Successfully detecting ocean-circulation-induced magnetic fields would provide a major step toward establishing novel observation techniques to explore the dynamics in the interior ocean. This thesis has provided the first approach to identifying these magnetic fields in geomagnetic satellite observations.

A
Appendix

A.1 Derivation of the law of Biot-Savart

The law of Biot-Savart describes the magnetic field $\mathbf{B}$ generated by a constant electric current $\mathbf{J}$. It can be derived from Maxwell's equations. According to Maxwells's equation (Equation (2.3b)), the magnetic field $\mathbf{B}$ is divergence-free, allowing the representation using a vector potential $\mathbf{A}$:

$$\mathbf{B} = \nabla \times \mathbf{A}, \tag{A.1}$$

where one chooses the Coulomb gauge so that the vector potential also fulfills:

$$\nabla \cdot \mathbf{A} = 0. \tag{A.2}$$

In order to derive the law of Biot-Savart, the case of magnetostatics is considered. In this case, as explained in Section 2.1.1, Maxwell's equation (2.3d) is simplified to:

$$\nabla \times \mathbf{B} = \mu_0 \mathbf{J}. \tag{A.3}$$

The magnetic field $\mathbf{B}$ in this equation can then be expressed by the introduced vector potential $\mathbf{A}$. Using the Grassmann identity and Equation (A.2), it follows:

$$\nabla \times \mathbf{B} = \nabla \times (\nabla \times \mathbf{A}) = \nabla(\nabla \cdot \mathbf{A}) - (\nabla \cdot \nabla)\mathbf{A} = -(\nabla \cdot \nabla)\mathbf{A}, \tag{A.4}$$

with the definition $(\nabla \cdot \nabla) = \nabla^2$ this leads to a Poisson equation for the vector potential depending on the electric current :

$$\nabla^2 \mathbf{A} \; = \; -\mu_0 \mathbf{J}. \tag{A.5}$$

The fundamental solution of Poisson's equation using Greens's function can be written as:

$$\mathbf{A}(\mathbf{r}) = \frac{\mu_0}{4\pi} \int_V \frac{\mathbf{J}(\mathbf{r}\,')}{|\mathbf{r} - \mathbf{r}\,'|}\, dV' \tag{A.6}$$

Subsequently, the definition of the vector potential (A.1) is applied again to the fundamental solution of Poisson's equation to obtain the magnetic field $\mathbf{B}$. Thereby, the integrand of Equation (A.6) is transformed using the following relation:

$$\nabla \times \frac{\mathbf{J}(\mathbf{r}\,')}{|\mathbf{r} - \mathbf{r}\,'|} \; = \mathbf{J}(\mathbf{r}\,') \; \times \; \frac{\mathbf{r} - \mathbf{r}\,'}{|\mathbf{r} - \mathbf{r}\,'|^3} \tag{A.7}$$

Finally, the combination of this relation with Equation (A.6) yields the law of Biot-Savart:

$$\mathbf{B}(\mathbf{r}) = \frac{\mu_0}{4\pi} \int_V \mathbf{J}(\mathbf{r}\,') \; \times \; \frac{\mathbf{r} - \mathbf{r}\,'}{|\mathbf{r} - \mathbf{r}\,'|^3}\, dV' \tag{A.8}$$

A.2 Biot-Savart distance formula

In order to estimate to what extent the spatial expansion of the magnetic field influences the neighboring scale factors, a simplified case is considered. Here the distance dependence of the strength of the magnetic field, which is caused by a current of a single grid cell, is examined. For simplification, a cuboid grid cell with the dimensions s_x, s_y and s_z at the origin of a Cartesian coordinate system is considered (the curvature of the Earth is neglected in the area around the grid cell). In this grid cell, a constant current in the x-direction is assumed. Finally, the resulting magnetic field can be evaluated at distance d above to this grid cell and satellite heigh h using the law of Biot-Savart:

$$\mathbf{B}(\mathbf{r}) = \frac{\mu_0}{4\pi} \int_V \mathbf{J}(\mathbf{r}\,') \; \times \; \frac{\mathbf{r} - \mathbf{r}\,'}{|\mathbf{r} - \mathbf{r}\,'|^3}\, dV', \tag{A.9}$$

In the simplified case, the electric current density in the considered grid cell is given by $\mathbf{J} = (J, 0, 0)$ and is assumed to be zero everywhere else. And the magnetic field $\mathbf{B}$ is evaluated at the position $\mathbf{r}_d = (0, d, h)$. The $\mathbf{r}\,'$ respresents the position vector in the grid celld and V' the corresponding volume. The consideration of electric current density and

location vector results in the following cross product:

$$\mathbf{J}(\mathbf{r}\,') \times (\mathbf{r} - \mathbf{r}\,') \;=\; \begin{pmatrix} J \\ 0 \\ 0 \end{pmatrix} \times \begin{pmatrix} -x \\ d-y \\ h-z \end{pmatrix} \;=\; \begin{pmatrix} 0 \\ -J(h-z) \\ J(d-y) \end{pmatrix} \tag{A.10}$$

Thus in this case the z-component of the magnetic field $\mathbf{B}_z$ (corresponding to the decisive radial magnetic field) is given by Biot-Savart (combine Equation (A.9) and Equation (A.10)):

$$\mathbf{B}_z(\mathbf{r}_d) \;=\; \frac{\mu_0}{4\pi} \int_{-\frac{s_z}{2}}^{\frac{s_z}{2}} \int_{-\frac{s_y}{2}}^{\frac{s_y}{2}} \int_{-\frac{s_x}{2}}^{\frac{s_x}{2}} \frac{J(d-y)}{\sqrt{x^2 + (d-y)^2 + (h-z)^2}^{\,3}}\, dx\, dy\, dz. \tag{A.11}$$

The considered grid size s_z is much smaller than the satellite height (satellite height of 460 km compared to ocean depth ≈ 5 km), which means $z \ll h$ in the integration volume so that one can approximatley assume $z \approx 0$. This allows the z-integration and lead to:

$$\mathbf{B}_z(\mathbf{r}_d) \;=\; \frac{\mu_0}{4\pi} \int_{-\frac{s_y}{2}}^{\frac{s_y}{2}} \int_{-\frac{s_x}{2}}^{\frac{s_x}{2}} \frac{j(d-y)}{\sqrt{x^2 + (d-y)^2 + h^2}^{\,3}}\, dx\, dy, \tag{A.12}$$

where the depth-integrated electric current density j is used, which is in the case of the considered simple cuboid grid cell given by: $j = J \cdot s_z$.
The y-integration can be solved analytical using the following integral relation:

$$\int \frac{(d-y)}{\sqrt{(d-y)^2 + c}^{\,3}}\, dy \;=\; \frac{1}{\sqrt{(d-y)^2 + c}} + const. \tag{A.13}$$

If this relation (A.13) is now applied to Equation (A.12) follows:

$$\mathbf{B}_z(\mathbf{r}_d) \;=\; \frac{\mu_0 j}{4\pi} \int_{-\frac{s_x}{2}}^{\frac{s_x}{2}} \frac{1}{\sqrt{x^2 + (d - \frac{s_x}{2})^2 + h^2}} - \frac{1}{\sqrt{x^2 + (d + \frac{s_x}{2})^2 + h^2}}\, dx. \tag{A.14}$$

Similarly, the x-integration can be solved analytical using the following integral relation:

$$\int \frac{1}{\sqrt{x^2 + c}}\, dx \;=\; \tanh^{-1}\left(\frac{x}{\sqrt{x^2 + c}}\right) + const, \tag{A.15}$$

which in combination with th relation of $\tanh^{-1}(x) = -\tanh^{-1}(-x)$ leads to:

$$\int_{-s}^{s} \frac{1}{\sqrt{x^2 + c}}\, dx \;=\; 2 \cdot \tanh^{-1}\left(\frac{s}{\sqrt{s^2 + c}}\right) \tag{A.16}$$

Now, using Equation (A.16) resolves the integral in Equation (A.14) and allows the simplification to:

$$\mathbf{B}_z(\mathbf{r}_d) = \frac{\mu_0 j}{4\pi}\left(2{\cdot}\tanh^{-1}\left(\frac{\frac{s_x}{2}}{\sqrt{\frac{{s_x}^2}{4}+(d-\frac{s_y}{2})^2+h^2}}\right) - 2{\cdot}\tanh^{-1}\left(\frac{\frac{s_x}{2}}{\sqrt{\frac{{s_x}^2}{4}+(d+\frac{s_y}{2})^2+h^2}}\right)\right), \tag{A.17}$$

which can be transformed further and with the assumption of a grid cell with the same length and width $s \approx s_x \approx s_y$ simplified to:

$$\mathbf{B}_z(\mathbf{r}_d) = \frac{\mu_0 j}{2\pi}\left(\tanh^{-1}\left(\frac{s}{\sqrt{s^2+(2d-s)^2+4h^2}}\right) - \tanh^{-1}\left(\frac{s}{\sqrt{s^2+(2d+s)^2+4h^2}}\right)\right). \tag{A.18}$$

This distance formula can be used with typical values (e.g., $s = 100\,\text{km}$ and $h = 460\,\text{km}$) to estimate the strength of the magentic field at distance d. In this thesis, this was used to motivate a typical correlation length.

A.3 ARP Parameters used in the Kalmag model

Table A.1: ARP paramters for the magnetic sources considered in the Kalmag model

Magnetic source	Spectrum	Radius	Timescale
Core	Flat	3456	935 a
Lithospheric	C-based	6287	∞
Residual ionospheric/induced	Flat	6324	0.71 d
Close magnetospheric	C-based	12524	1.54 d
Remote magnetospheric	C-based	235570	10.31 a
Fluctuating magnetospheric	C-based	13028	0.36 - 0.55 days
Field-aligned currents	C-based	7917	0

A.4 Geostrophic balance

Derivation of the geostrophic equations

The Equations (2.21) describing the geostrophic balance can be derived from the equations of motion under certain assumptions. Starting from Newton's second law $\mathbf{a} = \frac{\mathbf{F}}{m}$, the equations of motion can be formulated to describe ocean dynamics. These equations of conservation of linear momentum can be written in a three-component version for the coordinates x (eastward),y (northward), and z (upward) and corresponding velocities $\mathbf{v}_x$,

$\mathbf{v}_y$ and $\mathbf{v}_z$ as follows (see Pond and Pickard, 1983):

$$\frac{\mathrm{d}\mathbf{v}_x}{\mathrm{d}t} = -\frac{1}{\rho}\frac{\partial p}{\partial x} + 2\Omega\sin(\phi)\mathbf{v}_y - 2\Omega\cos(\phi)\mathbf{v}_z + \mathbf{F}_x^{\text{other}} \tag{A.19a}$$

$$\frac{\mathrm{d}\mathbf{v}_y}{\mathrm{d}t} = -\frac{1}{\rho}\frac{\partial p}{\partial y} - 2\Omega\sin(\phi)\mathbf{v}_x + \mathbf{F}_y^{\text{other}} \tag{A.19b}$$

$$\frac{\mathrm{d}\mathbf{v}_z}{\mathrm{d}t} = -\frac{1}{\rho}\frac{\partial p}{\partial z} + 2\Omega\cos(\phi)\mathbf{v}_x - g + \mathbf{F}_z^{\text{other}} \tag{A.19c}$$

The terms on the right-hand side of these equations of motion explicitly consider pressure, Coriolis, and gravity as acting forces. All other physical forces per unit mass (e.g., frictional or tidal forces) are summarized as $\mathbf{F}^{\text{other}}$. In Equations (A.19), ρ and p describe the density and the pressure, Ω the magnitude of the angular velocity of rotation of the Earth, ϕ the geographic latitude, and g the Earth's gravitational acceleration. The velocity components $\mathbf{v}$ then describe the motion of the ocean. The geostrophic approximation considers the large-scale mean circulation in the interior of the oceans. In this case, a steady state of the ocean is assumed, where oceanic velocities do not change with time, meaning no acceleration:

$$\frac{\mathrm{d}\mathbf{v}_x}{\mathrm{d}t} = \frac{\mathrm{d}\mathbf{v}_y}{\mathrm{d}t} = \frac{\mathrm{d}\mathbf{v}_z}{\mathrm{d}t} = 0, \tag{A.20}$$

and all other forces assumed to be zero:

$$\mathbf{F}^{\text{other}} = 0. \tag{A.21}$$

Under these assumptions, the equations of motion (A.19) simplify to (Pond and Pickard, 1983):

$$0 = -\frac{1}{\rho}\frac{\partial p}{\partial x} + 2\Omega\sin(\phi)\mathbf{v}_y - 2\Omega\cos(\phi)\mathbf{v}_z \tag{A.22a}$$

$$0 = -\frac{1}{\rho}\frac{\partial p}{\partial y} - 2\Omega\sin(\phi)\mathbf{v}_x \tag{A.22b}$$

$$0 = -\frac{1}{\rho}\frac{\partial p}{\partial z} + 2\Omega\cos(\phi)\mathbf{v}_x - g \tag{A.22c}$$

Additionally, vertical velocities are assumed to be so small compared to horizontal ones that the term $2\Omega\cos(\phi)\mathbf{v}_z$ in Equation (A.22a) can be neglected. By using the Coriolis parameter $f = 2\Omega\sin(\phi)$, Equation (A.22a) and (A.22b) yield the geostrophic equations for horizontal velocities:

$$f\mathbf{v}_y^{\text{geo}} = \frac{1}{\rho}\frac{\partial p}{\partial x} \qquad f\mathbf{v}_x^{\text{geo}} = -\frac{1}{\rho}\frac{\partial p}{\partial y} \tag{A.23}$$

Derivation of the hydrostatic equation

The hydrostatic equations can be derived using the same assumptions as described before in Section A.4 and considering Equation (A.22c). However, the term $2\Omega\cos(\phi)\mathbf{v}_x$ is small compared with g (typically four orders smaller, see Pond and Pickard, 1983) and can be neglected. From this follows the hydrostatic equation:

$$\frac{\partial p}{\partial z} = -\rho g \tag{A.24}$$

Derivation of geostrophic surface velocities and thermal wind equation

Instead of using the geostrophic balance (A.23) to calculate the absolute geostrophic velocities from pressure gradients, one can derive the geostrophic surface velocities from the slope of the sea surface height η. For this purpose, the hydrostatic equation (A.24) is considered and integrated over z from depth d until sea surface height η to obtain an expression for the pressure p (see Stewart, 2008):

$$p = \int_{-d}^{\eta} g\rho\, dz = \int_{-d}^{0} g\rho\, dz + \int_{0}^{\eta} g\rho\, dz, \tag{A.25}$$

where the integral has been split into two parts accounting for the pressure due to the height of water between depth d and the geoid $z = 0$ and the pressure to the height of water above the geoid (Stewart, 2008). The expression (A.25) can be used to replace the pressure in equation (A.23):

$$\mathbf{v}_y^{\text{geo}} = \frac{1}{f\rho}\frac{\partial}{\partial x}\int_{-d}^{0} g\rho\, dz + \frac{g}{f}\frac{\partial \eta}{\partial x} \qquad \mathbf{v}_x^{\text{geo}} = -\frac{1}{f\rho}\frac{\partial}{\partial y}\int_{-d}^{0} g\rho\, dz - \frac{g}{f}\frac{\partial \eta}{\partial y}. \tag{A.26}$$

The first term on the right-hand side of these equations describes the pressure gradient due to horizontal density differences, i.e., the baroclinic component, and the second term describes the pressure gradient due to sea surface slope, i.e., the barotropic component (Stewart, 2008). When assuming density ρ is constant, the first term in Equation (A.26), i.e., the baroclinic part, is zero. It follows an equation for the geostrophic surface currents:

$$\mathbf{v}_x^{\text{geo,s}} = -\frac{g}{f}\frac{\partial \eta}{\partial y} \qquad \mathbf{v}_y^{\text{geo,s}} = \frac{g}{f}\frac{\partial \eta}{\partial x}. \tag{A.27}$$

Otherwise, the first term in Equation (A.26) is used to calculate geostrophic velocities at depth z) with respect to a given reference level z_0, where the velocity is known . This

leads to the so called thermal wind equation:

$$\mathbf{v}_x^{\text{geo}}(z) = -\frac{g}{f\rho}\int_{z_0}^{z}\frac{\partial\rho}{\partial y}\,dz + \mathbf{v}_x^{\text{geo}} \qquad \mathbf{v}_y^{\text{geo}}(z) = \frac{g}{f\rho}\int_{z_0}^{z}\frac{\partial\rho}{\partial x}\,dz + \mathbf{v}_y^{\text{geo}}. \tag{A.28}$$

A.5 Additional plots quasi-stationary approximation

In Section 3.2.3, the deviations of the radial magnetic field in a single frequency band due to the quasi-stationary approximation are calculated. In Figure A.1, the deviations for two different excitation frequencies (weekly and monthly) are shown. Compared toFigure 3.3, it can be seen that the differences are already much smaller than for a daily excitation frequency.

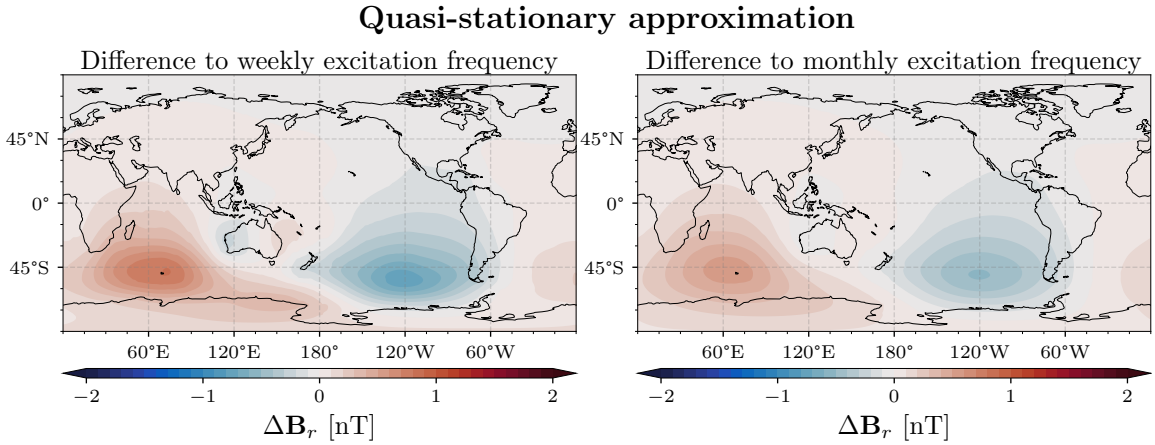

Figure A.1: Deviations between the radial magnetic field calculated with a different excitatory frequencies and the quasi-stationary approximation. The left side shows the differences for a weekly excitatory frequency and the right side for a monthly excitatory frequency.

A.6 Calibration of geostrophic electric current density

In the model-based validation of the geostrophic approach, the electric current density is derived from sea surface height taken from the GLOCER dataset. In order to avoid an exaggerated amplified magnetic signal around the equator, the geostrophic electric current density is calibrated. The geostrophic electric current density is calibrated using a depth-integrated electric current density directly derived from oceanic velocities of the ensemble mean of the GLOCER dataset. The data from the year 2013 (which is not concluded in the model-based validation of Section 3.3.1) is used for this calibration. Both zonal

and meridional depth-integrated electric current density is linearly calibrated according to Equation (3.1), where a is a calibration scale factor and b is a calibration constant. Both parameters are obtained independently for zonal and meridional depth.-integrated electric current density by a least-square-fit. Figure A.2 shows the resulting calibration paramters. It can be clearly seen that the scale factor a is the most important calibration parameter. Around the equator, the calibration results in a significant downscaling of the geostrophic electric current density.

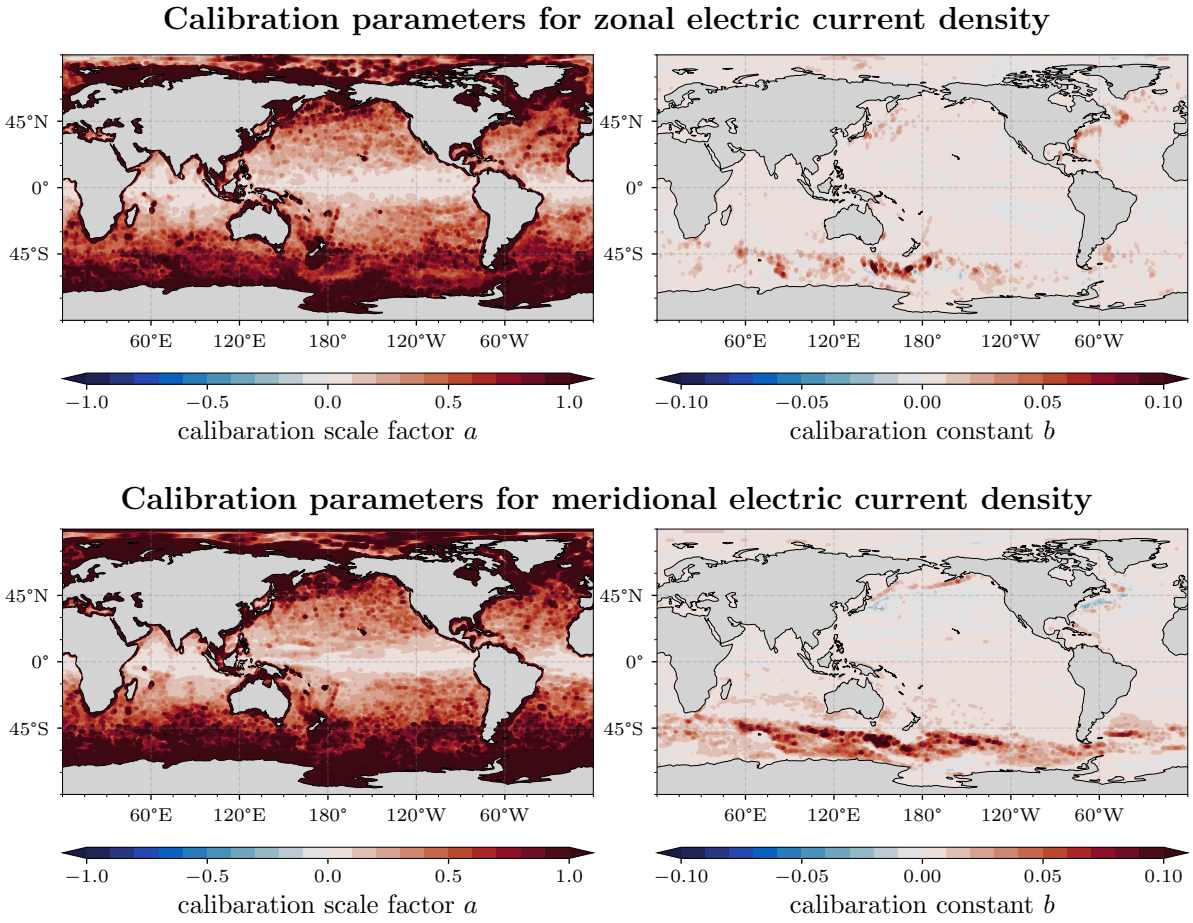

Figure A.2: Parameters for calibrating the geostrophic electric current density according to Equation (3.1). The left side shows the calibration scale factor a, and the right side the calibration constant b. The calibration parameters for the zonal electric current density are shown in the top row and the bottom for the meridional.

A.7 Correlation between observation-based and model-based OIMF estimates

In order to validate the geostrophic approach using real satellite altimetry-based data, the observation-based OIMF estimates are compared to the OIMF derived from the ocean reanalysis dataset GLOCER, which was also used in the validation study in Section 3.3. The temporal behavior of both the OIMF estimates based on the DUACS and ARMOR3D datasets are both compared using the correlation of the weekly time series from 2014 until 2021. The correlation is shown in Figure A.3.

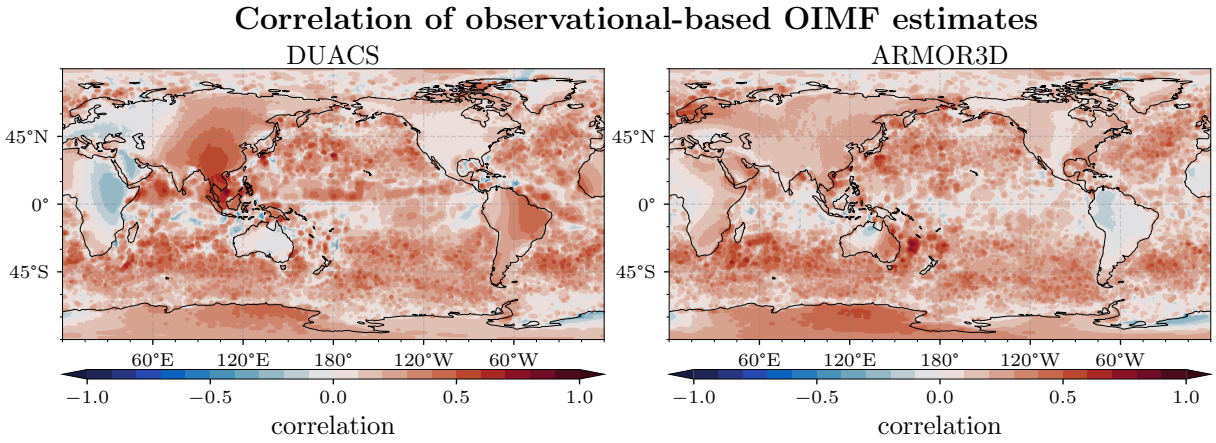

Figure A.3: Correlation between the time series of the observation-based OIMF from DUACS (left) or ARMOR (right) and the model-based OIMF derived from the ensemble mean of the ocean reanalysis dataset GLOCER.

A.8 Spatial constraints through an imposed covariance structure

Covariance matrix

As stated in Section 4.3, spatial constraints of the scale factors can be considered by a simplified parametrization of their covariance structure. Here, the chosen exponentially-decaying covariance matrix (see Equation (4.5)) is shown for different correlation lengths of $l = 500\,\text{km}$ and $l = 1000\,\text{km}$. Moreover, the covariance is compared to the OIMF covariance obtained from the OIMF estimates from the ECCO2 model. All covariance matrices are shown in Figure A.4.

Both positive and negative correlations occur in the full covariance matrix from the OIMF from ECCO2 (see left panel of Figure A.4). Also, significant correlations over

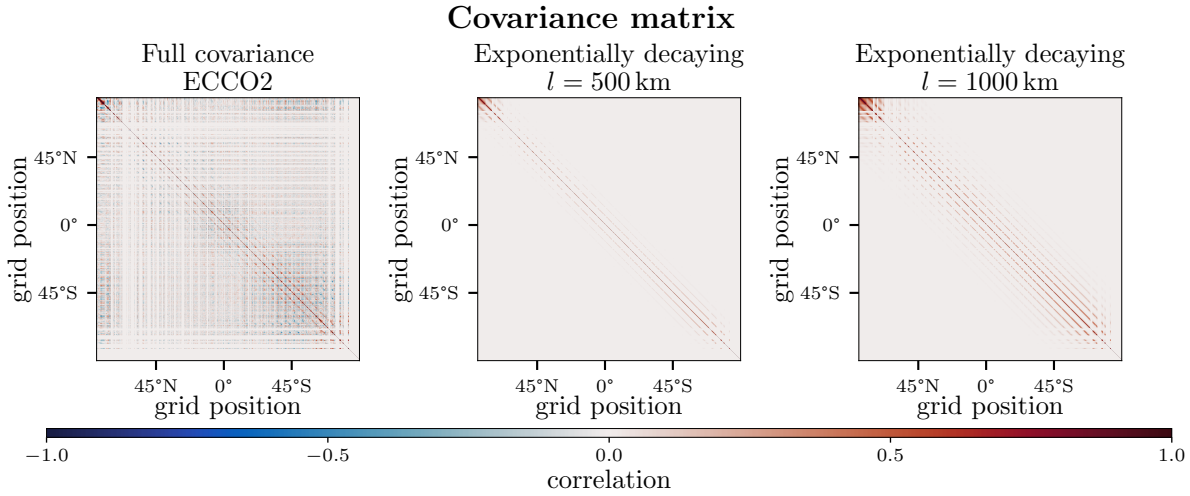

Figure A.4: An illustration of the covariance matrix associated with the OIMF (left plot) or the associated scale factor (middle and right plot). The grid positions of the Gauss-Legendre grid corresponding to SH 30 are sorted in a vector from north to south. The correlation between each other positions is then highlighted as a matrix. The left plot shows the covariance obtained from the OIMF estimates from ECCO2, and the right plot shows the exponential-decaying parametrization of the covariance for $l = 500\,\mathrm{km}$ and $l = 1000\,\mathrm{km}$ correlation length.

larger distances between different grid points can be seen. Contrarily, only positive correlations occur in the exponentially-decaying covariance matrix (see middle and right panel of Figure A.4), and significant correlations only arise for small distances. This is reflected in the secondary diagonal structure of the covariance matrix. A larger correlation length strengthens this structure (compare the middle to the right panel of Figure A.4). For all covariance matrices, the correlation between any grid point on land is set to zero, resulting in gaps in the structure of the covariance matrix. Notably, the secondary diagonal structure can also be identified in the full covariance matrix from the OIMF ECCO2 estimates. This comparison justifies the simplified exponentially-decaying covariance structure but also indicates that the correlation length must be chosen carefully.

OSSE results using different correlation length

The exponentially decaying covariance parameterizations based on different correlation lengths are used for further assimilations in an ideal OSSE. The results are presented similarly to Figure 4.11 in the case of $l = 500\,\text{km}$ using the imposed OIMF based on the ECCO2 up to a spatial resolution of SH degree of 30. Figure A.5 shows the final scale factor and its corresponding uncertainty using an exponentially decaying covariance with a correlation length of $l = 1000\,\text{km}$ and $l = 2000\,\text{km}$.

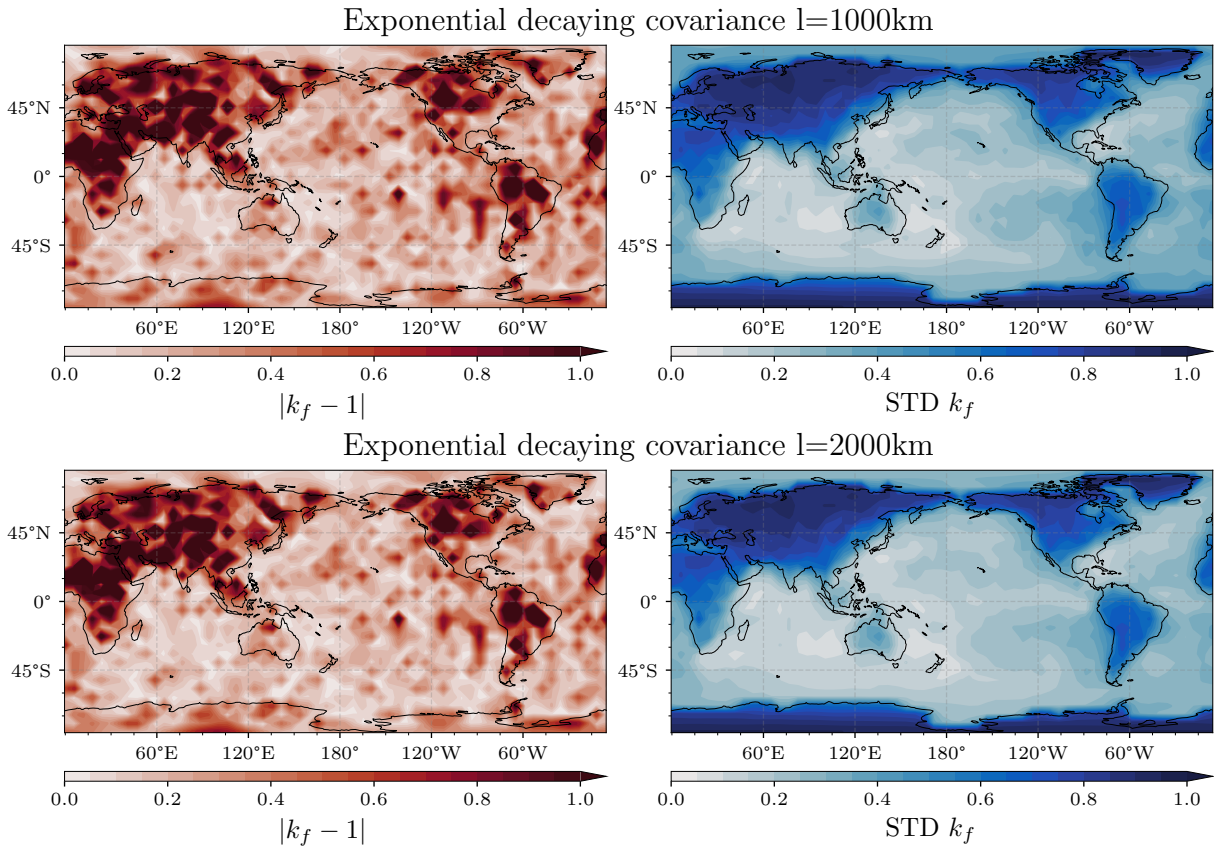

Figure A.5: The assimilation results of an ideal OSSE incorporating spatial constraints by an exponentially decaying covariance matrix with a correlation length of $l = 100\,\text{km}$ (top row) and $l = 500\,\text{km}$ (bottom row). The left side always shows the final scale factor deviation, and the right side the corresponding uncertainty of the scale factor.

A.9 NRMSD in ideal scenario

Here, it is shown that the NRMSD($\widetilde{\mathbf{B}}_r^{\text{res}}$) between rescaled and true magnetic field in the ideal scenario of the OSSE equals the scale factor deviation $|k_f - 1|$. The rescaled magnetic field anomalies are generally expressed by $\widetilde{\mathbf{B}}_r^{\text{res}} = k_f(x,y) \cdot \widetilde{\mathbf{B}}_r^{\text{imp}}$, which can be used in the NRMSD definition:

$$\text{NRMSD}(\widetilde{\mathbf{B}}_r^{\text{res}}) = \sqrt{\frac{\sum_{t_i=0}^{N} \left(k_f(x,y) \cdot \widetilde{\mathbf{B}}_r^{\text{imp}} - \widetilde{\mathbf{B}}_r^{\text{true}}(t_i,x,y)\right)^2}{\sum_{t_i=0}^{N} \widetilde{\mathbf{B}}_r^{\text{true}}(t_i,x,y)^2}} \,, \tag{A.29}$$

In the ideal scenario, $\widetilde{\mathbf{B}}_r^{\text{imp}} = \widetilde{\mathbf{B}}_r^{\text{true}}$ also applies, from which follows (since k_f is independent in time):

$$\text{NRMSD}(\widetilde{\mathbf{B}}_r^{\text{res}}) = \sqrt{\frac{(k_f(x,y)-1) \cdot \sum_{t_i=0}^{N} \left(\widetilde{\mathbf{B}}_r^{\text{true}}(t_i,x,y)\right)^2}{\sum_{t_i=0}^{N} \widetilde{\mathbf{B}}_r^{\text{true}}(t_i,x,y)^2}} = |k_f - 1| \,. \tag{A.30}$$

A.10 Detectability of presumed estimates from individual members of the GLOCER dataset

In the context of section 5.2.2, the method's application on real Swarm satellite observation based on presumed estimates from the GLOCER dataset was considered. A Kalman-filter assimilation was performed for each ensemble member (ORAS5, GloSea5, GLORYS) of the GLOCER dataset. In section 5.2.2, the results of the ensemble mean were presented (see figure 5.6) and discussed, and for the individual ensemble members, only an overview was given (see figure 5.7). Here, in figure A.6, the assimilation results based on an imposed OIMF from ORAS5, GloSea5, and GLORYS are presented separately. The final scale factor and its associated uncertainty are shown with a spatial resolution of SH degree of 15.

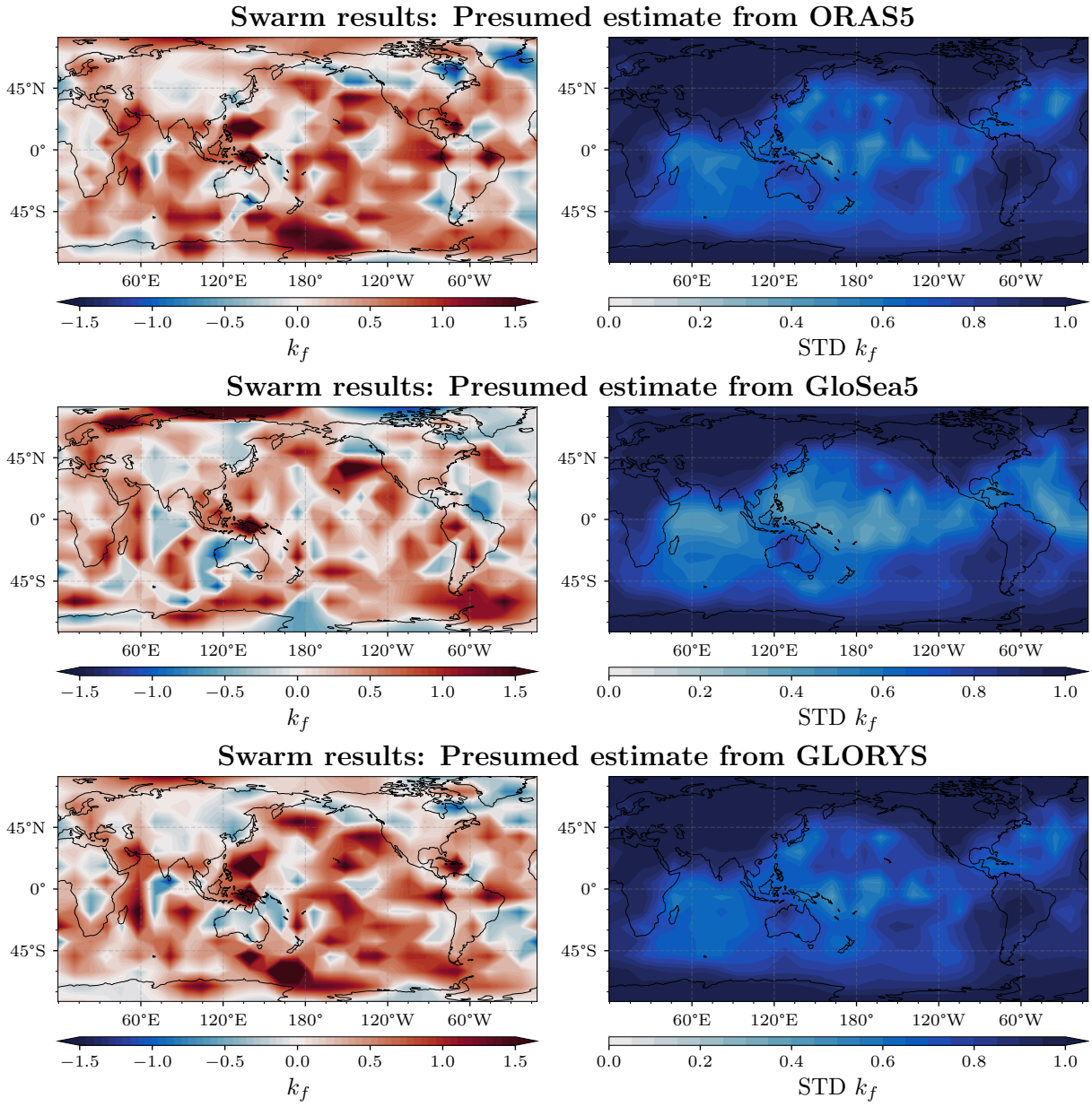

Figure A.6: The assimilation results based on Swarm observations and using various imposed OIMF estimated from the ORAS5, GloSea5, and GLORYS ocean reanalysis products of the GLOCER dataset. The left plot always shows the final scale factor (k_f) and the right one the associated uncertainty (posterior standard deviation) of the final scale factor (STD of k_f). The assimilation was initialized with a scale factor of zero and a corresponding uncertainty of one and performed with a spatial resolution of SH degree of 15.

List of Figures

List of Tables

Nomenclature

Abbreviations and acronyms

ACC	Antarctic Circumpolar Current
ADT	Absolute dynamic topography
Argo	Worldwide fleet of drifting ocean profiling floats
ARMOR3D	Multi Observation Global Ocean Product
ARP	Auto regressive processes
CHAMP	CHAllenging Minisatellite Payload
CMEMS	Copernicus Marine Environment Monitoring Service
DUACS	Data Unification and Altimeter Combination System
ECCO2	Estimating the Circulation and Climate of the Ocean, Phase II project (ocean model)
EM	electromagnetic
ECMWF	European Centre for Medium-Range Weather Forecasts
ETOPO	The ETOPO1 Global Relief Mode
ESA	European Space Agency
FFT	Fast Fourier Transformation
GLOCER	GLobal OCean Ensemble Reanalysis
GLORYS	Global Ocean Reanalysis and Simulation (ocean dataset, member of GLOCER)
GloSea5	Global Seasonal forecast system 5 (ocean dataset, member of GLOCER)
IGRF-13	International Geomagnetic Reference Field
JPL	Jet Propulsion Laboratory
Kalmag	Geomagnetic field model
KREMS	Kalman-filter-based Rescaling of ElectroMagnetic Signals
M2	Principal lunar semi-diurnal ocean tide constituent
MDT	Mean dynamic topography
NEMO	Nucleus for European Modelling of the Ocean (underlying common ocean model of GLOCER)
NEMOVAR	Ocean data assimilation system
NRMSD	Normalized Root-mean-square deviation
OGCM	Ocean General Circulation Model
ORAS5	Ocean Reanalysis System 5 (ocean dataset, member of GLOCER)

OIMF	Ocean-induced magnetic field
OSSE	Observing system simulation experiment
RMSD	Root-mean-square deviation
SEEK	Singular evolutive extended Kalman filter (ocean assimilation system)
SH	Sphercial harmonic functions
SLA	Sea level anomaly
Swarm	ESA geomagnetic field satellite mission
TEOS-10	Thermodynamic Equation of Seawater 2010
TPXO8	Global ocean tidal model
WOA18	World Ocean Atlas 2018
X3DG	Electromagnetic induction solver

List of Symbols

∇	Nabla operator
$\nabla \mathbf{f}$	Gradient of vector field $\mathbf{f}$
$\nabla \cdot \mathbf{f}$	Divergence of vector field $\mathbf{f}$
$\nabla \times \mathbf{f}$	Rotation of vector field $\mathbf{f}$
∇^2	Laplace operator, $\nabla^2 = (\nabla \cdot \nabla)$
∂	Partial derivative
Δ	Difference
$\overline{\mathbf{f}}$	Temporal mean of vector field $\mathbf{f}$
$\widetilde{\mathbf{f}}$	Anomalies of vector field $\mathbf{f}$
$\hat{\mathbf{f}}$	Amplitude of complex vector field $\mathbf{f}$
$\mathbf{M}^T$	Transpose of matrix $\mathbf{M}$
$\mathbf{M}^{-1}$	Inverse of matrix $\mathbf{M}$
$P(A)$	Probability of A
$P(A \mid B)$	Conditional probability of A given B
$\mathcal{N}(\mu, s)$	Normal distribution with mean μ and standard deviation s

Vectorial quantities:

$\mathbf{A}$	Magnetic field vector potential
$\mathbf{B}$	Magnetic field
$\mathbf{B}_r$	Radial component of the magnetic field
$\mathbf{B}^{\text{earth}}$	Earth magnetic main field
$\mathbf{B}^{\text{poloidal}}$, $\mathbf{B}^{\text{toroidal}}$	Poloidal and toroidal part of the magnetic field
$\mathbf{B}^{\text{true}}$, $\mathbf{B}^{\text{imp}}$, $\mathbf{B}^{\text{res}}$	True, imposed and rescaled oceanic magnetic field
$\mathbf{C}_{ij}$	Spatial covariance matrix scale factors
$\mathbf{E}$	Electric field
$\mathbf{F}$	Force
$\mathbf{F}^{\text{lorentz}}$	Lorentz force
$\mathbf{H}$	Observation operator
$\mathbf{I}$	Identity matrix
$\mathbf{J}$	Electric current density
$\mathbf{J}^{\text{ext}}$	External electric current density
$\mathbf{j}$	Depth-integrated electric current density
$\mathbf{j}^{\text{ext}}$	External depth-integrated electric current density
$\mathbf{j}^{\text{model}}$, $\mathbf{j}^{\text{geo}}$	Model-based and geostrophic depth-integrated electric current density
$\mathbf{K}_t$	Kalman gain matrix at time t
$\mathbf{P}_t^{\text{f}}, \mathbf{P}_t^{\text{a}}$	Covariance of the forcast or analyzed state of a system at time t
$\mathbf{R}_t$	Covariance of the observation noise at time t
$\mathbf{r}$	Radial vector in spherical coordinates

$\mathbf{v}$	Velocity vector
$\mathbf{v}_x$, $\mathbf{v}_y$, $\mathbf{v}_z$	Zonal (eastward), meridional (northward), vertical (upward) velocities
$\mathbf{v}_x^{\mathrm{geo}}$, $\mathbf{v}_y^{\mathrm{geo}}$	Zonal and meridional geostrophic velocities
$\mathbf{v}_x^{\mathrm{geo,s}}$, $\mathbf{v}_y^{\mathrm{geo,s}}$	Zonal and meridional geostrophic surface velocities
$\mathbf{x}_t^{\mathrm{f}}, \mathbf{x}_t^{\mathrm{a}}$	Mean of the forcast or analyzed state of a system at time t
$\mathbf{y}_t$	Observation vector at time t
$\mathbf{z}_s$	Vector of spherical harmonicsdescribing magnetic sourc s
$\boldsymbol{\xi}$	Gaussian white noise

Scalar quantities:

a_0	Reference radius for the magnetic source potential
a, b, c	Fit parameters
d	Depth
d_{ij}	Distance between two grid points i and j
f	Coriolis parameter
F_s	ARP Parameters for magnetic source s
g	Gravitational acceleration
$g_{\ell,m}$	Spherical harmonics coefficients of degree ℓ and order m
$g^c_{\ell,m}, g^s_{\ell,m}$	Cosine and sine sphercial harmonics coefficients of degree ℓ and order m
h	Height
i	Imaginary unit
k	Scale factor
k_0, k_f	Initial and final scale factor
k^{opt}	Optimal scale factor
l	Correlation length of the scale factors
$\ell, \ell_{\max}$	Degree (and maximum degree) of spherical harmonics
$m, m_{\max}$	Order (and maximum order) of spherical harmonics
p	Pressure
q	Unit charge
r	Radius
S	Salinity
T	Temperature
t	Time
V	Potential of magnetic source
$\mathrm{V}^{\mathrm{int}}$, $\mathrm{V}^{\mathrm{ext}}$	Internal and external magnetic source potential of Kalmag
V	Volume
$Y_{\ell,m}$	Spherical harmonics function of degree ℓ and order m
x, y, z	Zonal (eastward), meridional (northward) and vertical (upward) cartesian coordinates
ϵ_0	Vacuum Permittivity
η	Sea surface height

μ_0	Vaccuum magnetic permeability
ϱ	Electric charge density
ρ	Seawater density
σ	Electrical conductivity
φ	Geographical latitude
ϕ	Scalar potential of the ocean-induced magnetic source
Φ	Scalar potential poloidal magnetic field
Ψ	Scalar potential toroidal magnetic field
Ω	Magnitude of the angular velocity of the Earth's rotation
ω	Angular frequency
ω_i	Gaussian quadrature weights at i^{th} Gauss node

Bibliography

Alken, P., Thébault, E., Beggan, C. D., Amit, H., Aubert, J., Baerenzung, J., Bondar, T. N., Brown, W. J., Califf, S., Chambodut, A., Chulliat, A., Cox, G. A., Finlay, C. C., Fournier, A., Gillet, N., Grayver, A., Hammer, M. D., Holschneider, M., Huder, L., Hulot, G., Jager, T., Kloss, C., Korte, M., Kuang, W., Kuvshinov, A., Langlais, B., Léger, J.-M., Lesur, V., Livermore, P. W., Lowes, F. J., Macmillan, S., Magnes, W., Mandea, M., Marsal, S., Matzka, J., Metman, M. C., Minami, T., Morschhauser, A., Mound, J. E., Nair, M., Nakano, S., Olsen, N., Pavón-Carrasco, F. J., Petrov, V. G., Ropp, G., Rother, M., Sabaka, T. J., Sanchez, S., Saturnino, D., Schnepf, N. R., Shen, X., Stolle, C., Tangborn, A., Tøffner-Clausen, L., Toh, H., Torta, J. M., Varner, J., Vervelidou, F., Vigneron, P., Wardinski, I., Wicht, J., Woods, A., Yang, Y., Zeren, Z., and Zhou, B.: International Geomagnetic Reference Field: the thirteenth generation, Earth, Planets and Space, 73, 49, https://doi.org/10.1186/s40623-020-01288-x, 2021.

Amante, C. and Eakins, B.: ETOPO1 1 Arc-Minute Global Relief Model: procedures, data sources and analysis, NOAA Technical Memorandum NESDIS NGDC-24, National Geophysical Data Center, Boulder,Colorado, https://doi.org/10.7289/V5C8276M, 2009.

Anderson, D. L. T., Sheinbaum, J., and Haines, K.: Data assimilation in ocean models, Reports on Progress in Physics, 59, 1209, https://doi.org/10.1088/0034-4885/59/10/001, 1996.

ARMOR3D: Multi Observation Global Ocean ARMOR3D L4 analysis, Dataset, Copernicus Marine Environment Monitoring Service, URL https://doi.org/10.48670/moi-00052, 2022.

Aubert, J., Finlay, C. C., and Fournier, A.: Bottom-up control of geomagnetic secular variation by the Earth's inner core, Nature, 502, 219–223, https://doi.org/10.1038/nature12574, 2013.

Backus, G.: Poloidal and toroidal fields in geomagnetic field modeling, Reviews of Geophysics, 24, 75–109, https://doi.org/10.1029/RG024i001p00075, 1986.

Baerenzung, J., Holschneider, M., Wicht, J., Lesur, V., and Sanchez, S.: The Kalmag model as a candidate for IGRF-13, Earth, Planets and Space, 72, 163, https://doi.org/10.1186/s40623-020-01295-y, 2020.

Baerenzung, J., Holschneider, M., Saynisch-Wagner, J., and Thomas, M.: Kalmag: a high spatio-temporal model of the geomagnetic field, Earth, Planets and Space, 74, 139, https://doi.org/10.1186/s40623-022-01692-5, 2022.

Bao, S., Wang, H., Ren, Z., Yan, H., and Chen, J.: Spatial and temporal scales of sea surface salinity in the tropical Indian Ocean from SMOS, Aquarius and SMAP, Journal of Oceanography, 76, 389–400, https://doi.org/10.1007/s10872-020-00552-8, 2020.

Barnoud, A., Pfeffer, J., Cazenave, A., Fraudeau, R., Rousseau, V., and Ablain, M.: Revisiting the global mean ocean mass budget over 2005–2020, Ocean Science, 19, 321–334, https://doi.org/10.5194/os-19-321-2023, 2023.

Bayes, T.: LII. An essay towards solving a problem in the doctrine of chances. By the late Rev. Mr. Bayes, F. R. S. communicated by Mr. Price, in a letter to John Canton, A. M. F. R. S, Philosophical Transactions of the Royal Society of London, 53, 370–418, https://doi.org/10.1098/rstl.1763.0053, 1763.

Blockley, E. W., Martin, M. J., McLaren, A. J., Ryan, A. G., Waters, J., Lea, D. J., Mirouze, I., Peterson, K. A., Sellar, A., and Storkey, D.: Recent development of the Met Office operational ocean forecasting system: an overview and assessment of the new Global FOAM forecasts, Geoscientific Model Development, 7, 2613–2638, https://doi.org/10.5194/gmd-7-2613-2014, 2014.

Brankart, J.-M., Cosme, E., Testut, C.-E., Brasseur, P., and Verron, J.: Efficient Adaptive Error Parameterizations for Square Root or Ensemble Kalman Filters: Application to the Control of Ocean Mesoscale Signals, Monthly Weather Review, 138, 932–950, https://doi.org/10.1175/2009MWR3085.1, 2010.

Bretherton, F., Davis, R., and Fandry, C.: A technique for objective analysis and design of oceanographic experiments applied to MODE-73, Deep Sea Research and Oceanographic Abstracts, 23, 559–582, https://doi.org/https://doi.org/10.1016/0011-7471(76)90001-2, 1976.

Chave, A. D. and Luther, D. S.: Low-frequency, motionally induced electromagnetic fields in the ocean: 1. Theory, Journal of Geophysical Research: Oceans, 95, 7185–7200, https://doi.org/https://doi.org/10.1029/JC095iC05p07185, 1990.

Chen, J.: Satellite gravimetry and mass transport in the earth system, Geodesy and Geodynamics, 10, 402–415, https://doi.org/10.1016/j.geog.2018.07.001, 2019.

Cherry, D. W. and Stovold, A. T.: Earth Currents in Short Submarine Cables, Nature, 157, 766–766, https://doi.org/10.1038/157766a0, 1946.

de Verdière, A. C. and Michel Ollitrault, M.: A Direct Determination of the World Ocean Barotropic Circulation, Journal of Physical Oceanography, 46, 255 – 273, https://doi.org/10.1175/JPO-D-15-0046.1, 2016.

Desportes, C., Garric, G., Régnier, C., Drévillon, M., Parent, L., Garric, G., Drillet, Y., Masina, S., Storto, A., Mirouze, I., Cipollone, A., Zuo, H., Balmaseda, M., Peterson, D., Wood, R., Jackson, L., Mulet, S., Greiner, E., and Gounou, A.: Global Ocean Reanalysis Multi-model Ensemble Products, Quality information document, Copernicus Marine Environment Monitoring Service, URL https://catalogue.marine.copernicus.eu/documents/QUID/CMEMS-GLO-QUID-001-031.pdf, 2022.

Doglioni, F., Ricker, R., Rabe, B., Barth, A., Troupin, C., and Kanzow, T.: Sea surface height anomaly and geostrophic current velocity from altimetry measurements over the Arctic Ocean (2011–2020), Earth System Science Data, 15, 225–263, https://doi.org/10.5194/essd-15-225-2023, 2023.

Dostal, J., Martinec, Z., and Thomas, M.: The modelling of the toroidal magnetic field induced by tidal ocean circulation, Geophysical Journal International, 189, 782–798, https://doi.org/10.1111/j.1365-246X.2012.05407.x, 2012.

DUACS: Global Ocean Gridded L 4 Sea Surface Heights And Derived Variables Reprocessed 1993 Ongoing, Dataset, Copernicus Marine Environment Monitoring Service, URL https://doi.org/10.48670/moi-00148, 2022.

ECCO2: Estimating the Circulation and Climate of the Ocean II, Dataset, NASA Jet Propulsion Laboratory, URL https://ecco.jpl.nasa.gov/drive/files/ECCO2/cube92_latlon_quart_90S90N, 2022.

Egbert, G. D. and Erofeeva, S. Y.: Efficient Inverse Modeling of Barotropic Ocean Tides, Journal of Atmospheric and Oceanic Technology, 19, 183 – 204, https://doi.org/10.1175/1520-0426(2002)019<0183:EIMOBO>2.0.CO;2, 2002.

Eldardiry, H., Hossain, F., Srinivasan, M., and Tsontos, V.: Success Stories of Satellite Radar Altimeter Applications, Bulletin of the American Meteorological Society, 103, E33 – E53, https://doi.org/https://doi.org/10.1175/BAMS-D-21-0065.1, 2022.

Everett, M. E., Constable, S., and Constable, C. G.: Effects of near-surface conductance on global satellite induction responses, Geophysical Journal International, 153, 277–286, https://doi.org/10.1046/j.1365-246X.2003.01906.x, 2003.

Ferry, N., Parent, L., Garric, G., Barnier, B., and Jourdain, N.: Mercator global eddy permitting ocean reanalysis GLORYS1V1: Description and results, Mercator Ocean Quarterly Newsletter, 36, 15–27, 2010.

Finlay, C. C., Kloss, C., Olsen, N., Hammer, M. D., Tøffner-Clausen, L., Grayver, A., and Kuvshinov, A.: The CHAOS-7 geomagnetic field model and observed changes in the South Atlantic Anomaly, Earth, Planets and Space, 72, 156, https://doi.org/10.1186/s40623-020-01252-9, 2020.

Flosadóttir, A. H., Larsen, J. C., and Smith, J. T.: Motional induction in North Atlantic circulation models, Journal of Geophysical Research: Oceans, 102, 10 353–10 372, https://doi.org/10.1029/96JC03603, 1997.

Friis-Christensen, E., Lühr, H., and Hulot, G.: Swarm: A constellation to study the Earth's magnetic field, Earth, Planets and Space, 58, 351–358, https://doi.org/10.1186/BF03351933, 2006.

Fu, L.-L., Christensen, E. J., Yamarone Jr., C. A., Lefebvre, M., Ménard, Y., Dorrer, M., and Escudier, P.: TOPEX/POSEIDON mission overview, Journal of Geophysical Research: Oceans, 99, 24 369–24 381, https://doi.org/https://doi.org/10.1029/94JC01761, 1994.

Gill, A. E.: Atmosphere-Ocean Dynamics, vol. 30, Academic Press, Inc., San Diego, California 92101, 1982.

Gillet, N., Jault, D., Finlay, C. C., and Olsen, N.: Stochastic modeling of the Earth's magnetic field: Inversion for covariances over the observatory era, Geochemistry, Geophysics, Geosystems, 14, 766–786, https://doi.org/10.1002/ggge.20041, 2013.

GLOCER: Global Ocean Ensemble Physics Reanalysis, Dataset, Copernicus Marine Environment Monitoring Service, URL https://doi.org/10.48670/moi-00024, 2022.

Grantham, W., Bracalente, E., Jones, W., and Johnson, J.: The SeaSat-A satellite scatterometer, IEEE Journal of Oceanic Engineering, 2, 200–206, https://doi.org/10.1109/JOE.1977.1145338, 1977.

Gray, A. R. and Riser, S. C.: A method for multiscale optimal analysis with application to Argo data, Journal of Geophysical Research: Oceans, 120, 4340–4356, https://doi.org/https://doi.org/10.1002/2014JC010208, 2015.

Grayver, A., Schnepf, N. R., Kuvshinov, A., Sabaka, T. J., Manoj, C., and Olsen, N.: Satellite tidal magnetic signals constrain oceanic lithosphere-asthenosphere boundary, Science Advances, 2, e1600 798, https://doi.org/10.1126/sciadv.1600798, 2016.

Grayver, A., Munch, F., Kuvshinov, A., Khan, A., Sabaka, T., and Tøffner-Clausen, L.: Joint inversion of satellite-detected tidal and magnetospheric signals constrains electrical conductivity and water content of the upper mantle and transition zone: INVERSION OF SATELLITE MAGNETIC DATA, Geophysical Research Letters, 44, https://doi.org/10.1002/2017GL073446, 2017.

Greiner, E., Verbrugge, N., Mulet, S., and Guinehut, S.: Multi Observation Global Ocean 3D Temperature Salinity Heights Geostrophic Currents and MLD Product, Quality information document, Copernicus Marine Environment Monitoring Service, URL https://catalogue.marine.copernicus.eu/documents/QUID/CMEMS-MOB-QUID-015-012.pdf, 2021.

Guinehut, S., Dhomps, A.-L., Larnicol, G., and Le Traon, P.-Y.: High resolution 3-D temperature and salinity fields derived from in situ and satellite observations, Ocean Science, 8, 845–857, https://doi.org/10.5194/os-8-845-2012, 2012.

Gurvan, M., Bourdallé-Badie, R., Chanut, J., Clementi, E., Coward, A., Ethé, C., Iovino, D., Lea, D., Lévy, C., Lovato, T., Martin, N., Masson, S., Mocavero, S., Rousset, C., Storkey, D., Müeller, S., Nurser, G., Bell, M., Guillaume Samson, G., Pierre Mathiot, P., Mele, F., and Moulin, A.: NEMO ocean engine, https://doi.org/10.5281/zenodo.6334656, 2022.

Heaviside, O.: XXXIX. On the electromagnetic effects due to the motion of electrification through a dielectric, The London, Edinburgh, and Dublin Philosophical Magazine and Journal of Science, 27, 324–339, https://doi.org/10.1080/14786448908628362, 1889.

Holschneider, M., Lesur, V., Mauerberger, S., and Baerenzung, J.: Correlation-based modeling and separation of geomagnetic field components, Journal of Geophysical Research: Solid Earth, 121, 3142–3160, https://doi.org/https://doi.org/10.1002/2015JB012629, 2016.

Holton, J. R. and Hakim, G. J.: Chapter 2 - Basic Conservation Laws, in: An Introduction to Dynamic Meteorology (Fifth Edition), edited by Holton, J. R. and Hakim, G. J., pp. 31–66, Academic Press, Boston, fifth edition edn., https://doi.org/https://doi.org/10.1016/B978-0-12-384866-6.00002-7, 2013.

Hornschild, A., Baerenzung, J., Saynisch-Wagner, J., Irrgang, C., and Thomas, M.: On the detectability of the magnetic fields induced by ocean circulation in geomagnetic satellite observations, Earth, Planets and Space, 74, 182, https://doi.org/10.1186/s40623-022-01741-z, 2022.

Hulot, G., Sabaka, T., N. Olsen, N., and Fournier, F.: 5.02 - The Present and Future Geomagnetic Field, in: Treatise on Geophysics (Second Edition), edited by Schubert, G., pp. 33–78, Elsevier, Oxford, second edition edn., https://doi.org/10.1016/B978-0-444-53802-4.00096-8, 2015.

Irrgang, C., Saynisch, J., and Thomas, M.: Impact of variable seawater conductivity on motional induction simulated with an ocean general circulation model, Ocean Science, 12, 129–136, https://doi.org/10.5194/os-12-129-2016, 2016.

Irrgang, C., Saynisch, J., and Thomas, M.: Utilizing oceanic electromagnetic induction to constrain an ocean general circulation model: A data assimilation twin experiment, Journal of Advances in Modeling Earth Systems, 9, 1703–1720, https://doi.org/10.1002/2017MS000951, 2017.

Irrgang, C., Saynisch, J., and Thomas, M.: Estimating global ocean heat content from tidal magnetic satellite observations, Scientific Reports, 9, 7893, https://doi.org/10.1038/s41598-019-44397-8, 2019.

Ivchenko, V. O., Sidorenko, D., Danilov, S., Losch, M., and Schröter, J.: Can sea surface height be used to estimate oceanic transport variability?, Geophysical Research Letters, 38, https://doi.org/https://doi.org/10.1029/2011GL047387, 2011.

Johnson, G. C., Lumpkin, R., Boyer, T., Bringas, F., Cetinić, I., Chambers, D. P., Cheng, L., Dong, S., Feely, R. A., Fox-Kemper, B., Frajka-Williams, E., Franz, B. A., Yao Fu, Y., Gao, M., Garg, J., Gilson, J., G., G., Hamlington, B. D., Hewitt, H. T., Hobbs, W. R., Hu, Z., Huang, B., Jevrejeva, S., Johns, W. E., Katsunari, S., Kennedy, J. J., Kersalé, M., Killick, R. E., Leuliette, E., Locarnini, R., Lozier, M. S., M., L. J., Merrifield, M. A., Mishonov, A., Mitchum, G. T., Moat, B. I., Nerem, R. S., Notz, D., Perez, R. C., Purkey, S. G., Rayner, D., Reagan, J., Schmid, C., Siegel, D. A., Smeed, D. A., Stackhouse, P. W., Sweet, W., Thompson, P. R., Volkov, D. L., Wanninkhof, R., Weller, R. A., Wen, C., Westberry, T. K., Widlansky, M. J., Willis, J. K., Yu, L., and Zhang, H.-M.: Global Oceans, Bulletin of the American Meteorological Society, 103, 143 – 192, https://doi.org/10.1175/BAMS-D-22-0072.1, 2022.

K., L., Yoshinari, H., Maximenko, N. A., and Hacker, P. W.: YoMaHa'07: Velocity data assessed from trajectories of Argo floats at parking level and at the sea surface, Technical Note 4(2), National Geophysical Data Center, IPRC, URL http://apdrc.soest.hawaii.edu/projects/yomaha/yomaha07/YoMaHa070612.pdf, 2007.

Kalman, R. E.: A New Approach to Linear Filtering and Prediction Problems, Journal of Basic Engineering, 82, 35–45, https://doi.org/10.1115/1.3662552, 1960.

Kelbert, A., Kuvshinov, A., Velímský, J., Koyama, T., Ribaudo, J., Sun, J., Martinec, Z., and Weiss, C. J.: Global 3-D electromagnetic forward modelling: a benchmark study, Geophysical Journal International, 197, 785–814, https://doi.org/10.1093/gji/ggu028, 2014.

Kuvshinov, A.: 3-D Global Induction in the Oceans and Solid Earth: Recent Progress in Modeling Magnetic and Electric Fields from Sources of Magnetospheric, Ionospheric and Oceanic Origin, Surv Geophys, 29, 139–186, https://doi.org/10.1007/s10712-008-9045-z, 2008.

Kuvshinov, A. and Olsen, N.: 3-D Modelling of the Magnetic Fields Due to Ocean Tidal Flow, pp. 359–365, Springer Berlin Heidelberg, Berlin, Heidelberg, https://doi.org/10.1007/3-540-26800-6_57, 2005.

Kuvshinov, A. and Semenov, A.: Global 3-D imaging of mantle electrical conductivity based on inversion of observatory C-responses—I. An approach and its verification, Geophysical Journal International, 189, 1335–1352, https://doi.org/10.1111/j.1365-246X.2011.05349.x, 2012.

Landerer, F. W., Flechtner, F. M., Save, H., Webb, F. H., Bandikova, T., Bertiger, W. I., Bettadpur, S. V., Byun, S. H., Dahle, C., Dobslaw, H., Fahnestock, E., Harvey, N., Kang, Z., Kruizinga, G. L. H., Loomis, B. D., McCullough, C., Murböck, M., Nagel, P., Paik, M., Pie, N., Poole, S., Strekalov, D., Tamisiea, M. E., Wang, F., Watkins, M. M., Wen, H.-Y., Wiese, D. N., and Yuan, D.-N.: Extending the Global Mass Change Data Record: GRACE Follow-On Instrument and Science Data Performance, Geophysical Research Letters, 47, e2020GL088 306, https://doi.org/https://doi.org/10.1029/2020GL088306, 2020.

Larsen, J. C.: Electric and Magnetic Fields Induced by Deep Sea Tides, Geophysical Journal of the Royal Astronomical Society, 16, 47–70, https://doi.org/10.1111/j.1365-246X.1968.tb07135.x, 1968.

Laske, G. and Masters, G.: A global digital map of sediment thickness, EOS Trans. AGU, 78, F483, URL https://igppweb.ucsd.edu/~gabi/sediment.html, 1997.

Le Traon, P. Y.: From satellite altimetry to Argo and operational oceanography: three revolutions in oceanography, Ocean Science, 9, 901–915, https://doi.org/10.5194/os-9-901-2013, 2013.

Lin, M. and Yang, C.: Ocean Observation Technologies: A Review, Chinese Journal of Mechanical Engineering, 33, 32, https://doi.org/10.1186/s10033-020-00449-z, 2020.

Longuet-Higgins, M., Stern, M., and Stommel, H.: The electrical field induced by ocean currents and waves, with applications to the method of towed electrodes, Physical Oceanography and Meteorology, 13, 1–37, https://doi.org/10.1575/1912/1064, 1954.

Lorentz, H. A.: Versuch einer Theorie der electrischen und optischen Erscheinungen in bewegten Körpern, Cambridge Library Collection - Physical Sciences, Cambridge University Press, https://doi.org/10.1017/CBO9781139381406, 1895.

MacLachlan, C., Arribas, A., Peterson, K. A., Maidens, A., Fereday, D., Scaife, A. A., Gordon, M., Vellinga, M., Williams, A., Comer, R. E., Camp, J., Xavier, P., and Madec, G.: Global Seasonal forecast system version 5 (GloSea5): a high-resolution seasonal forecast system, Quarterly Journal of the Royal Meteorological Society, 141, 1072–1084, https://doi.org/https://doi.org/10.1002/qj.2396, 2015.

Manoj, C., Kuvshinov, A., Maus, S., and Lühr, H.: Ocean circulation generated magnetic signals, Earth, Planets and Space, 58, 429–437, https://doi.org/10.1186/BF03351939, 2006.

Masters, D., Nerem, R. S., Choe, C., Leuliette, E., Beckley, B., White, N., and Ablain, M.: Comparison of Global Mean Sea Level Time Series from TOPEX/Poseidon, Jason-1, and Jason-2, Marine Geodesy, 35, 20–41, https://doi.org/10.1080/01490419.2012.717862, 2012.

Matzka, J., Stolle, C., Yamazaki, Y., Bronkalla, O., and Morschhauser, A.: The Geomagnetic Kp Index and Derived Indices of Geomagnetic Activity, Space Weather, 19, e2020SW002 641, https://doi.org/https://doi.org/10.1029/2020SW002641, 2021.

Maus, S. and Kuvshinov, A.: Ocean tidal signals in observatory and satellite magnetic measurements, Geophysical Research Letters, 31, 1–4, https://doi.org/10.1029/2004GL020090, 2004.

Maxwell, J. C.: VIII. A dynamical theory of the electromagnetic field, Philosophical Transactions of the Royal Society of London, 155, 459–512, https://doi.org/10.1098/rstl.1865.0008, 1865.

Mazloff, M. R., Cornuelle, B. D., Gille, S. T., and Verdy, A.: Correlation Lengths for Estimating the Large-Scale Carbon and Heat Content of the Southern Ocean, Journal of Geophysical Research: Oceans, 123, 883–901, https://doi.org/https://doi.org/10.1002/2017JC013408, 2018.

McDougall, T. J. and Barker, P.: Getting started with TEOS-10 and the Gibbs Seawater (GSW) Oceanographic Toolbox, 2011.

Menemenlis, D., Fukumori, I., and Lee, T.: Using Green's Functions to Calibrate an Ocean General Circulation Model, Monthly Weather Review, 133, 1224–1240, https://doi.org/10.1175/MWR2912.1, 2005.

Menemenlis, D., Campin, J.-M., Heimbach, P., Hill, C., Lee, T., Nguyen, A., Schodlok, M., and Zhang, H.: ECCO2: High Resolution Global Ocean and Sea Ice Data Synthesis, in: AGU Fall Meeting Abstracts, pp. OS31C–1292, URL https://ui.adsabs.harvard.edu/abs/2008AGUFMOS31C1292M, 2008.

Minami, T., Schnepf, N. R., and Toh, H.: Tsunami-generated magnetic fields have primary and secondary arrivals like seismic waves, Scientific Reports, 11, 2287, https://doi.org/10.1038/s41598-021-81820-5, 2021.

Mogensen, K. and Balmaseda, W.: The NEMOVAR ocean data assimilation system as implemented in the ECMWF ocean analysis for System 4, https://doi.org/10.21957/x5y9yrtm, 2012.

Moore, A. M.and Martin, M. J., Akella, S., Arango, H. G., Balmaseda, M., Bertino, L., Ciavatta, S., Cornuelle, B., Cummings, J., Frolov, S., Lermusiaux, P., Oddo, P., Oke, P. R., Storto, A., Teruzzi, A., Vidard, A., and Weaver, A. T.: Synthesis of Ocean Observations Using Data Assimilation for Operational, Real-Time and Reanalysis Systems: A More Complete Picture of the State of the Ocean, Frontiers in Marine Science, 6, https://doi.org/10.3389/fmars.2019.00090, 2019.

Mulet, S., Rio, M.-H., Etienne, H., Artana, C., Cancet, M., Dibarboure, G., Feng, H., Husson, R., Picot, N., Provost, C., and Strub, P. T.: The new CNES-CLS18 global mean dynamic topography, Ocean Science, 17, 789–808, https://doi.org/10.5194/os-17-789-2021, 2021.

Nature: Water Movements and Earth Currents : Electrical and Magnetic Effects*, Nature, 161, 192–193, https://doi.org/10.1038/161192a0, 1948.

Ollitrault, M. and de Verdière, A. C.: The Ocean General Circulation near 1000-m Depth, Journal of Physical Oceanography, 44, 384 – 409, https://doi.org/10.1175/JPO-D-13-030.1, 2014.

Park, S.-Y., Dash, U. K., and Yu, J.: Length Scale Analyses of Background Error Covariances for EnKF and EnSRF Data Assimilation, Atmosphere, 13, 160, https://doi.org/10.3390/atmos13020160, 2022.

Petereit, J., Saynisch, J., Irrgang, C., Weber, T., and Thomas, M.: Electromagnetic characteristics of ENSO, Ocean Science, 14, 515–524, https://doi.org/10.5194/os-14-515-2018, 2018.

Petereit, J., Saynisch-Wagner, J., Irrgang, C., and Thomas, M.: Analysis of Ocean Tide-Induced Magnetic Fields Derived From Oceanic In Situ Observations: Climate Trends and the Remarkable Sensitivity of Shelf Regions, Journal of Geophysical Research: Oceans, 124, 8257–8270, https://doi.org/https://doi.org/10.1029/2018JC014768, 2019.

Pham, D., Verron, J., and Christine Roubaud, M. C.: A singular evolutive extended Kalman filter for data assimilation in oceanography, Journal of Marine Systems, 16, 323–340, https://doi.org/10.1016/S0924-7963(97)00109-7, 1998.

Pond, S. and Pickard, G. L.: Introductory Dynamical Oceanography, Elsevier Butterworth-Heinemann, The Boulevard, Kidlington, Oxford, second edn., https://doi.org/https://doi.org/10.1016/C2009-0-24288-7, 1983.

Pujol, M.-I., Faugère, Y., Taburet, G., Dupuy, S., Pelloquin, C., Ablain, M., and Picot, N.: DUACS DT2014: the new multi-mission altimeter data set reprocessed over 20 years, Ocean Science, 12, 1067–1090, https://doi.org/10.5194/os-12-1067-2016, 2016.

Pujol, M.-I., Taburet, G., and SL-TAC team: Sea Level TAC - DUACS products, Quality information document, Copernicus Marine Environment Monitoring Service, URL https://catalogue.marine.copernicus.eu/documents/QUID/CMEMS-SL-QUID-008-032-068.pdf, 2023.

Püthe, C., Kuvshinov, A., Khan, A., and Olsen, N.: A new model of Earth's radial conductivity structure derived from over 10 yr of satellite and observatory magnetic data, Geophysical Journal International, 203, 1864–1872, https://doi.org/10.1093/gji/ggv407, 2015.

Reigber, C., Lühr, H., and Schwintzer, P.: CHAMP mission status, Advances in Space Research, 30, 129–134, https://doi.org/10.1016/S0273-1177(02)00276-4, 2002.

Rio, M. H., Guinehut, S., and Larnicol, G.: New CNES-CLS09 global mean dynamic topography computed from the combination of GRACE data, altimetry, and in situ measurements, Journal of Geophysical Research: Oceans, 116, https://doi.org/https://doi.org/10.1029/2010JC006505, 2011.

Ronald Anderson, R.: The Referees' Assessment of Faraday's Electromagnetic Induction Paper of 1831, Notes and Records of the Royal Society of London, 47, 243–256, URL http://www.jstor.org/stable/531789, 1993.

Sabaka, T. J., Tyler, R. H., and Olsen, N.: Extracting ocean-generated tidal magnetic signals from Swarm data through satellite gradiometry, Geophysical Research Letters, 43, 3237–3245, https://doi.org/10.1002/2016GL068180, 2016.

Sabaka, T. J., Tøffner-Clausen, L., Olsen, N., and Finlay, C. C.: A comprehensive model of Earth's magnetic field determined from 4 years of Swarm satellite observations, Earth, Planets and Space, 70, 130, https://doi.org/10.1186/s40623-018-0896-3, 2018.

Sabaka, T. J., Tøffner-Clausen, L., Olsen, N., and Finlay, C. C.: CM6: a comprehensive geomagnetic field model derived from both CHAMP and Swarm satellite observations, Earth, Planets and Space, 72, 80, https://doi.org/10.1186/s40623-020-01210-5, 2020.

Šachl, L., Martinec, Z., Velímský, J., Irrgang, C., Petereit, J., Saynisch, J., Einšpigel, D., and Schnepf, N. R.: Modelling of electromagnetic signatures of global ocean circulation: physical approximations and numerical issues, Earth, Planets and Space, 71, 58, https://doi.org/10.1186/s40623-019-1033-7, 2019.

Sanford, T. B.: Motionally Induced Electric and Magnetic Fields in the Sea, Journal of Geophysical Research, 76, 3476–3492, https://doi.org/10.1029/JC076i015p03476, 1971.

Saynisch, J., Petereit, J., Irrgang, C., Kuvshinov, A., and Thomas, M.: Impact of climate variability on the tidal oceanic magnetic signal—A model-based sensitivity study, Journal of Geophysical Research: Oceans, 121, 5931–5941, https://doi.org/10.1002/2016JC012027, 2016.

Saynisch, J., Irrgang, C., and Thomas, M.: On the Use of Satellite Altimetry to Detect Ocean Circulation's Magnetic Signals, Journal of Geophysical Research: Oceans, 123, 2305–2314, https://doi.org/https://doi.org/10.1002/2017JC013742, 2018.

Saynisch-Wagner, J., Baerenzung, J., Hornschild, A., Irrgang, C., and Thomas, M.: Tide-induced magnetic signals and their errors derived from CHAMP and Swarm satellite magnetometer observations, Earth, Planets and Space, 73, 234, https://doi.org/10.1186/s40623-021-01557-3, 2021.

Saynisch-Wagner, J., Baerenzung, J., Hornschild, A., and Thomas, M.: Tidal transports from satellite observations of Earth's magnetic field, submitted to Science Advances, 2023.

Schmitt, R. W.: The Ocean's Role in Climate, Oceanography, 31, 32 – 40, https://doi.org/10.5670/oceanog.2018.225, 2018.

Schnepf, N. R., Manoj, C., Kuvshinov, A., Toh, H., and Maus, S.: Tidal signals in ocean-bottom magnetic measurements of the Northwestern Pacific: observation versus prediction, Geophysical Journal International, 198, 1096–1110, https://doi.org/10.1093/gji/ggu190, 2014.

Schnepf, N. R., Kuvshinov, A., and Sabaka, T.: Can we probe the conductivity of the lithosphere and upper mantle using satellite tidal magnetic signals?, Geophysical Research Letters, 42, 3233–3239, https://doi.org/https://doi.org/10.1002/2015GL063540, 2015.

Schnepf, N. R., Manoj, C., An, C., Sugioka, H., and Toh, H.: Time-Frequency Characteristics of Tsunami Magnetic Signals from Four Pacific Ocean Events, Pure and Applied Geophysics, 173, 3935–3953, https://doi.org/10.1007/s00024-016-1345-5, 2016.

Stammer, D. and Cazenave, A.: Satellite Altimetry over Oceans and Land Surfaces, CRC Press, Taylor & Francis Group, 6000 Broken Sound Parkway NW, Suite 300, 2018.

Stanley, H. R.: The Geos 3 Project, Journal of Geophysical Research: Solid Earth, 84, 3779–3783, https://doi.org/10.1029/JB084iB08p03779, 1979.

Stephenson, D. and Bryan, K.: Large-scale electric and magnetic fields generated by the oceans, Journal of Geophysical Research: Oceans, 97, 15 467–15 480, https://doi.org/10.1029/92JC01400, 1992.

Stewart, R. H.: Introduction to Physical Oceanography, Department of Oceanography, Texas A&M University, URL https://www.colorado.edu/oclab/sites/default/files/attached-files/stewart_textbook.pdf, 2008.

Suzuki, A.: Geomagnetic Sq field at successive Universal Times, Journal of Atmospheric and Terrestrial Physics, 40, 449–463, https://doi.org/10.1016/0021-9169(78)90177-0, 1978.

Takeda, M.: Features of global geomagnetic Sq field from 1980 to 1990, Journal of Geophysical Research: Space Physics, 107, SIA 4–1–SIA 4–8, https://doi.org/10.1029/2001JA009210, 2002.

Tapley, B. D., Bettadpur, S., Watkins, M., and Reigber, C.: The gravity recovery and climate experiment: Mission overview and early results, Geophysical Research Letters, 31, https://doi.org/https://doi.org/10.1029/2004GL019920, 2004.

Tapley, B. D., Watkins, M. M., Flechtner, F., Reigber, C., Bettadpur, S., Rodell, M., Sasgen, I., Famiglietti, J. S., Landerer, F. W., Chambers, D. P., Reager, J. T., Gardner, A. S., Save, H., Ivins, E. R., Swenson, S. C., Boening, C., Dahle, C., Wiese, D. N., Dobslaw, H., Tamisiea, M. E., and Velicogna, I.: Contributions of GRACE to understanding climate change, Nature Climate Change, 9, 358–369, https://doi.org/10.1038/s41558-019-0456-2, 2019.

Toh, H., Satake, K., Hamano, Y., Fujii, Y., and Goto, T.: Tsunami signals from the 2006 and 2007 Kuril earthquakes detected at a seafloor geomagnetic observatory, Journal of Geophysical Research: Solid Earth, 116, 1–10, https://doi.org/10.1029/2010JB007873, 2011.

Trossman, D. S. and Tyler, R. H.: Predictability of Ocean Heat Content From Electrical Conductance, Journal of Geophysical Research: Oceans, 124, 667–679, https://doi.org/10.1029/2018JC014740, 2019.

Tyler, R. H., Mysak, L. A., and Oberhuber, J. M.: Electromagnetic fields generated by a three dimensional global ocean circulation, Journal of Geophysical Research: Oceans, 102, 5531–5551, https://doi.org/10.1029/96JC03545, 1997.

Tyler, R. H., Oberhuber, J., and Sanford, T.: The potential for using ocean generated electromagnetic fields to remotely sense ocean variability, Physics and Chemistry of the Earth, Part A: Solid Earth and Geodesy, 24, 429–432, https://doi.org/10.1016/S1464-1895(99)00054-X, 1999.

Tyler, R. H., Maus, S., and Luhr, H.: Satellite observations of magnetic fields due to ocean tidal flow, Science, 299, 239–241, https://doi.org/10.1126/science.1078074, 2003.

Tyler, R. H., Boyer, T. P., Minami, T., Zweng, M. M., and Reagan, J. R.: Electrical conductivity of the global ocean, Earth, Planets and Space, 69, 156, https://doi.org/10.1186/s40623-017-0739-7, 2017.

Velímský, J.: Determination of three-dimensional distribution of electrical conductivity in the Earth's mantle from Swarm satellite data: Time-domain approach, Earth, Planets and Space, 65, 5, https://doi.org/10.5047/eps.2013.08.001, 2013.

Velímský, J., Grayver, A., Kuvshinov, A., and Šachl, L.: On the modelling of M2 tidal magnetic signatures: effects of physical approximations and numerical resolution, Earth, Planets and Space, 70, 192, https://doi.org/10.1186/s40623-018-0967-5, 2018.

Velímský, J., Schnepf, N. R., Nair, M. C., and Thomas, N. P.: Can seafloor voltage cables be used to study large-scale circulation? An investigation in the Pacific Ocean, Ocean Science, 17, 383–392, https://doi.org/10.5194/os-17-383-2021, 2021.

Velímský, J. and Martinec, Z.: Time-domain, spherical harmonic-finite element approach to transient three-dimensional geomagnetic induction in a spherical heterogeneous Earth, Geophysical Journal International, 161, 81–101, https://doi.org/10.1111/j.1365-246X.2005.02546.x, 2005.

Velímský, J., Šachl, L., and Martinec, Z.: The global toroidal magnetic field generated in the Earth's oceans, Earth and Planetary Science Letters, 509, 47–54, https://doi.org/10.1016/j.epsl.2018.12.026, 2019.

Vigo, M. I., García-García, D., Sempere, M. D., and Chao, B. F.: 3D Geostrophy and Volume Transport in the Southern Ocean, Remote Sensing, 10, https://doi.org/10.3390/rs10050715, 2018.

Vivier, F., Maier-Reimer, E., and Tyler, R. H.: Simulations of magnetic fields generated by the Antarctic Circumpolar Current at satellite altitude: Can geomagnetic measurements be used to monitor the flow?, Geophysical Research Letters, 31, https://doi.org/10.1029/2004GL019804, 2004.

Wieczorek, M. and Meschede, M.: SHTools: Tools for Working with Spherical Harmonics, Geochemistry, Geophysics, Geosystems, 19, 2574–2592, https://doi.org/10.1029/2018GC007529, 2018.

WOA18: World Ocean Atlas 2018, Dataset, NOAA National Centers for Environmental Information, URL https://www.ncei.noaa.gov/products/world-ocean-atlas, 2019.

Wong, A. P. S., Wijffels, S. E., Riser, S. C., Pouliquen, S., Hosoda, S., Roemmich, D., Gilson, J., Johnson, G. C., Martini, K., Murphy, D. J., Scanderbeg, M., Bhaskar, T. V. S. U., Buck, J. J. H., Merceur, F., Carval, T., Maze, G., Cabanes, C., André, X., Poffa, N., Yashayaev, I., Barker, P. M., Guinehut, S., Belbéoch, M., Ignaszewski, M., Baringer, M. O., Schmid, C., Lyman, J. M., McTaggart, K. E., Purkey, S. G., Zilberman, N., Alkire, M. B., Swift, D., Owens, W. B., Jayne, S. R., Hersh, C., Robbins, P., West-Mack, D., Bahr, F., Yoshida, S., Sutton, P. J. H., Cancouët, R., Coatanoan, C., Dobbler, D., Juan, A. G., Gourrion, J., Kolodziejczyk, N., Bernard, V., Bourlès, B., Claustre, H., D'Ortenzio, F., Le Reste, S., Le Traon, P.-Y., Rannou, J.-P., Saout-Grit, C., Speich, S., Thierry, V., Verbrugge, N., Angel-Benavides, I. M., Klein, B., Notarstefano, G., Poulain, P.-M., Vélez-Belchí, P., Suga, T., Ando, K., Iwasaska, N., Kobayashi, T., Masuda, S., Oka, E., Sato, K., Nakamura, T., Sato, K., Takatsuki, Y., Yoshida, T., Cowley, R., Lovell, J. L., Oke, P. R., van Wijk, E. M., Carse, F., Donnelly, M., Gould, W. J., Gowers, K., King, B. A., Loch, S. G., Mowat, M., Turton, J., Rama Rao, E. P., Ravichandran, M., Freeland, H. J., Gaboury, I., Gilbert, D., Greenan, B. J. W., Ouellet, M., Ross, T., Tran, A., Dong, M., Liu, Z., Xu, J., Kang, K., Jo, H., Kim, S.-D., and Park, H.-M.: Argo Data 1999–2019: Two Million Temperature-Salinity Profiles and Subsurface Velocity Observations From a Global Array of Profiling Floats, Frontiers in Marine Science, 7, https://doi.org/10.3389/fmars.2020.00700, 2020.

Yi, S. and Choe, G. S.: The toroidal field surfaces in the standard poloidal-toroidal representation of magnetic field, Scientific Reports, 12, 2944, https://doi.org/10.1038/s41598-022-07040-7, 2022.

Young, F., Gerrard, H., and evons, W.: XIII. On electrical disturbances due to tides and waves, The London, Edinburgh, and Dublin Philosophical Magazine and Journal of Science, 40, 149–159, https://doi.org/10.1080/14786440708636105, 1920.

Zanna, L., Khatiwala, S., Gregory, J. M., Ison, J., and Heimbach, P.: Global reconstruction of historical ocean heat storage and transport, Proceedings of the National Academy of Sciences, 116, 1126–1131, https://doi.org/10.1073/pnas.1808838115, 2019.

Zuo, H., Balmaseda, M. A., de Boisseson, E., Hirahara, S., Chrust, M., and de Rosnay, P.: A generic ensemble generation scheme for data assimilation and ocean analysis, https://doi.org/10.21957/cub7mq0i4, 2017.

Zuo, H., Balmaseda, M. A., Tietsche, S., Mogensen, K., and Mayer, M.: The ECMWF operational ensemble reanalysis–analysis system for ocean and sea ice: a description of the system and assessment, Ocean Science, 15, 779–808, https://doi.org/10.5194/os-15-779-2019, 2019.

Danksagung

An dieser Stelle möchte ich meinen Dank aussprechen. Der gilt zuerst meinen Eltern Friderun und Pedro, die mich immer unterstützt haben und mir, wenn nötig mit Rat und Tat zur Seite standen.

Ich möchte mich bei Prof. Maik Thomas und Dr. Jan Saynisch-Wagner bedanken, die mir die Möglichkeit gaben als Teilchenphysiker einen gewagten Sprung in die neuen Gewässer der Ozeane zu wagen, indem sie mir diese Dissertation und das zugehörige Projekt ermöglicht haben und mir das Vertrauen dazu geschenkt haben.

Jan möchte ich nochmal ganz ausdrücklich für die beständige Betreuung meiner Dissertation danken, für all die Ratschläge und Hinweise, welche ich manchmal erst viel später verstanden habe, und natürlich für deine Geduld, die einem als Betreuer wohl häufiger abverlangt wird.

Die letzte Zeit war nicht nur aufgrund der Dissertation außergwöhnlich, sondern wird in den Erinnerungen auch immer von der Covid19-Pandemie geprägt sein. Viele Tage war mein Büro leer und der Arbeitsplatz verlassen...
Diese spezielle Zeit benötigte besondere Leute - daher möchte ich mich bei Linus Shihora und Roman Sulzbach nicht nur als Arbeitskollegen und Bürokollegen bedanken, sondern auch dafür, dass ihr diese besonderen Leute gewesen seid.
Die Zeit mit euch werde ich auch trotz der Covid19-Einschränkungen immer in bester Erinnerung behalten.

Bei Christopher Irrgang und Julien Baerenzung möchte ich mich vor allem auch nochmal für die zahlreichen Anregungen, Erklärungen, Hilfen und die wissenschaftliche Zusammenarbeit bedanken.

Außerdem möchte ich allen aus der Sektion 1.3 für das gute Arbeitsklima danken. Dir, Reyko Schachtschneider, sei an dieser Stelle auch nochmal explizit gedankt für deine Korrekturen zu dieser Arbeit.

Zu guter Letzt danke ich natürlich dir, Anna Oprei, für Korrekturen, Unterstützung, und so vieles mehr...

Eidesstattliche Erklärung

Hiermit versichere ich an Eides statt, die vorliegende Dissertation selbstständig und ohne unerlaubte Hilfe angefertigt zu haben.

Bei der Verfassung der Dissertation wurden keine anderen als die im Text aufgeführten Hilfsmittel verwendet.

Ein Promotionsverfahren zu einem früheren Zeitpunkt an einer anderen Hochschule oder bei einem anderen Fachbereich wurde nicht beantragt.

Ort, Datum

Aaron Hornschild